TOWARDS QUANTUM TELECOMMUNICATION AND A THORIUM NUCLEAR CLOCK

A Thesis
Presented to
The Academic Faculty

by

Alexander G. Radnaev

In Partial Fulfillment
of the Requirements for the Degree
Doctor of Philosophy in the
School of Physics

Georgia Institute of Technology
December 2012

TOWARDS QUANTUM TELECOMMUNICATION AND A THORIUM NUCLEAR CLOCK

Approved by:

Professor T. A. Brian Kennedy,
Committee Chair
School of Physics
Georgia Institute of Technology

Professor Alex Kuzmich, Advisor
School of Physics
Georgia Institute of Technology

Professor Kenneth R. Brown
School of Chemistry and Biochemistry
Georgia Institute of Technology

Professor Phillip N. First
School of Physics
Georgia Institute of Technology

Dr. Steven Jefferts
Time and Frequency Division
National Institute of Standards and Technology

Date Approved: 15 August 2012

To my parents and brother.

ACKNOWLEDGEMENTS

in the neighboring labs, Chris Hamley, Eva Bookjans, Peyman Ahmadi, Chung-Yu Shin, Michael DePalatis, Thai Hoang, Corey Gerving, Gustavo Telles, and Tetsuya Ishikawa, from whom I borrowed optics, electronics, and bits of advice. I particularly owe thanks to Chris for our numerous and fruitful technical discussions. Tetsuya deserves special acknowledgment for his kindness and continuing friendship.

A special, heartfelt thank you goes to my troop of industrious undergraduate research assistants whom I taught and worked with and whose energy and passion greatly benefited the lab: Aurelien Billot, Jacob Blumoff, Leroy Jia, Mariano Leonhardt, Amin Agha, John Parker, Michael Valdes, Alex Lind, and Diya Radhakrishna. I would like to specially recognize Jacob Blumoff for his highly productive assistance with the telecom experiments. Another special recognition is deserved by the wonderful trio of Michael Valdes, Alex Lind, and Diya Radhakrishna, who performed a tremendous amount of work for the thorium project and made the lab a more engaging place.

In addition to the people who aided me in my graduate studies, of equal importance are the mentors who inspired me as an undergraduate and research assistant prior to joining the Kuzmich Lab.

As an undergraduate at the Moscow Engineering Physics Institute, I discovered my passion for atomic physics in the course of my research under Vladimir Velichanskys group at the Lebedev Physical Institute. I would like to heartily thank Sergei Zibrov, Vitaly Vasil'ev, and especially Vladimir Velichansky for providing the solid foundation in physics that proved invaluable in my graduate career at Georgia Tech.

Prior to joining the Kuzmich Lab, I had the fortune to work under Steven Jefferts at the National Institute of Standards and Technology. I would like to thank Tom Heavner, Stefania Romisch, and Steve for demonstrating their exemplary methods of doing physics, as well as introducing me to the precision measurement of time intervals. I am very thankful to Steve and Stefi for their warm friendship, support,

and an unforgettable summer spent in Boulder, Colorado.

Lastly, I wish to express the highest degree of gratitude to my parents, Ludmila and Georgiy, and my brother, Lev, for their infinite love and support, and for fostering my curiosity for science.

TABLE OF CONTENTS

LIST OF TABLES

LIST OF FIGURES

SUMMARY

With recent advances in atomic, molecular, and optical physics, it is now possible to perform a broad spectrum of quantum-level manipulations on the external and internal degrees of freedom for single atoms, single photons, and collective systems, achieving accuracies at the 10^{-17} level [3]. This thesis presents the results of the work performed by the author on Rubidium atoms in magneto-optical traps and triply charged Thorium ions in electrodynamic traps towards future advances in long-distance quantum telecommunication, next generation clocks, and fundamental tests of current physical theories.

In Chapters II, III, and IV, experimental realizations of two core building blocks of a quantum repeater [4] are described: a multiplexed quantum memory and a telecom interface for long-lived quantum memories. A color change of single-photon level light fields by several hundred nanometers in an optically thick cold gas is demonstrated, while preserving quantum entanglement with a remotely stored matter excitation. These are essential elements for long-distance quantum telecommunication, fundamental tests of quantum mechanics, and applications in secure communication and computation [5, 6].

In Chapter V, the first trapping and laser cooling of Thorium-229 ions are described. Thorium-229 nuclear electric quadrupole moment is revealed by hyperfine spectroscopy of triply charged Thorium-229 ions, described in Chapter VI. A system to search for the isomer nuclear transition in Thorium-229 is developed and tested with the excitation of a forbidden electronic transition at 717 nm, presented in Chapter VI. Direct excitation of the nuclear transition with laser light would allow for an

extremely accurate clock [7] and a sensitive test bed for variations of fundamental physical constants [8], including the fine structure constant.

Chapter VII concludes with a summary of the results and an outlook for future research.

CHAPTER I

INTRODUCTION

This chapter describes the motivation for the experimental work of this thesis.

1.1 Long distance quantum telecommunication

Quantum information promises to provide great advances in computing [6] and information security [5]. While quantum key distribution is already commercially available on a scale of 100 miles, scaling up to continental scales is challenging due to the exponential absorption in the atmosphere or the optical fibers. A deteriorated quantum signal cannot be amplified without destroying the quantum information it carries [9], and therefore the classical solution of using amplifiers is not applicable.

There are two approaches to solving this problem. The first one is conceptually straightforward: remove the media and transmit signals through outer space [10]. The second approach relies on a so-called quantum repeater architecture [4] with a particular realization proposed in a seminal paper by Duan *et al.*. The idea is to use atomic ensembles as the memory elements of the quantum repeater [1], as illustrated in Fig.1. The protocols proposed to distribute entanglement over large distances require quantum memory storage lifetimes that are large compared to the classical communication time between nodes.

Fundamental advances in the interface of single photon fields and alkali atom memories have been made [2, 11–19] following the work of Duan *et al.*. However, the most promising quantum memories operate with light wavelengths outside the transparency windows of modern telecom fibers (Fig.3). Moreover, due to the intrinsic probabilistic nature of the protocol, the entanglement distribution rates are impractically low.
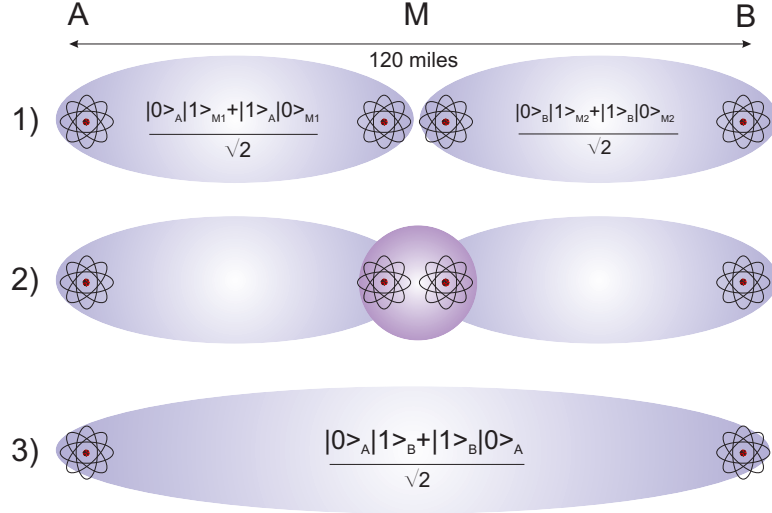
Figure 1: A quantum repeater architecture. If a signal can propagate for only 60 miles, qubits A and B separated by twice that distance can be entangled by using an intermediate node of quantum memories in the intermediate site. In step one qubit A can be entangled with the intermediate qubit 1, and B with qubit 2. In step two, qubits A and B become entangled by performing a projecting measurement on the intermediate qubits 1 and 2.

In this work, solutions to these key challenges are demonstrated: the multiplexed quantum memory array for boosting the communication rate, and the entanglement of long-lived quantum memory with telecommunication wavelength light fields to minimize exponential transmission losses through existing fiber-based networks. These advances bring us closer to entanglement distribution on a continental scale and can be useful for both fundamental and applied problems: quantum key distribution for more secure communication and tests of quantum mechanics by providing an answer to the Einstein-Podolsky-Rosen paradox [20] without locality and detection loopholes [21].

1.1.1 Multiplexed quantum memory

Multiplexing is a method of combining information signals over a shared medium. In classical fiber-based telecommunication networks, signals can be transmitted via
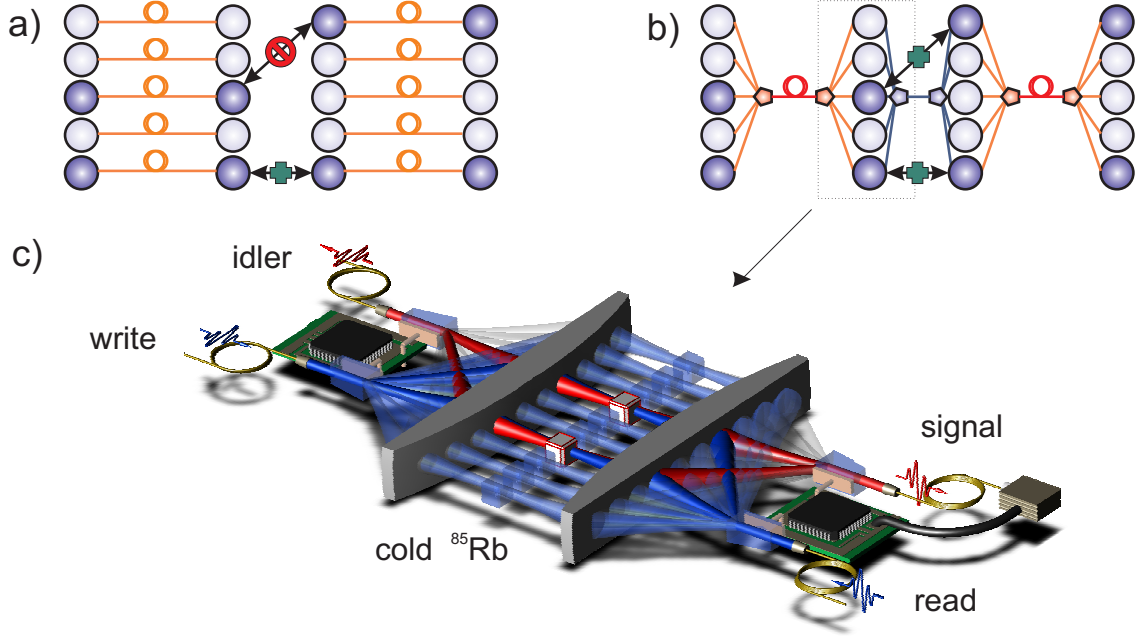
Figure 2: a) Parallel and b) multiplexed quantum repeater architectures. In a multiplexed system, probabilistically-generated atomic excitations in channels can be interconnected in real time, greatly increasing the probability of entanglement generation. c) A realization of a multiplexed quantum memory node based on a laser cooled atomic gas addressed by acousto-optical deflectors.

the same fiber using separation by frequency (Dense Wavelength Division Multiplexing), time (Time Division Multiplexing), polarization, angular momentum, etc. Combining these techniques with the ability to reconnect arbitrary elements of a quantum memory array based on detection feedback can dramatically increase the entanglement distribution rate and lower the requirements for memory lifetime [22]. Time division multiplexing ideally utilizes the time delay due to feedback signal propagation, and combined with the dynamic reconfiguration of the connections between quantum memories increases the number of repeater states where entanglement distribution is possible (Fig.2). In Chapter II, an experimental realization of a multiplexed quantum memory of 12 elements capable of boosting the communication rates by several orders of magnitude is demonstrated.

3

1.1.2 Telecom conversion for quantum memories
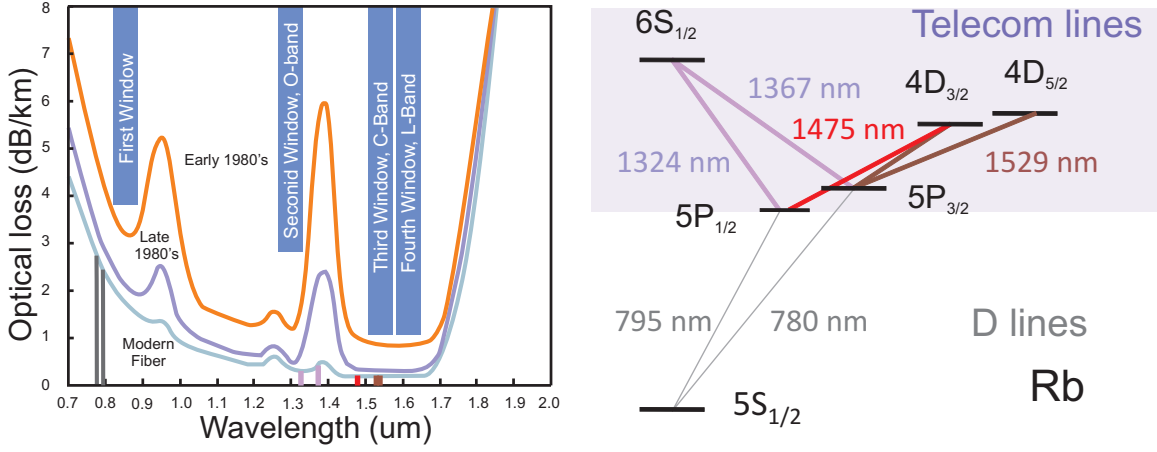
Figure 3: a) Optical fiber losses in the infrared domain overlapped with memory and telecom Rubidium lines, corresponding to the transitions of a Rubidium atom (b). Rubidium quantum memory D-lines are coupled with various telecom wavelength transitions through the $5P$ states.

A long-distance quantum information network requires transmission between quantum memory elements at telecom wavelengths where absorption is minimized (Fig.3a). Unfortunately, typical atomic ground-state electronic transitions suitable for quantum information applications lie outside the telecom window [2, 16, 17, 19, 23–25], limiting the transmission to a distance to a few kilometers. In this work, long-lived quantum memory entangled with telecom light is demonstrated by a wavelength conversion of the near-infrared light emitted on the ground-state transition to telecom wavelengths, engaging telecom transitions in rubidium (Fig.3). The conversion is achieved with a non-degenerate non-collinear four-wave mixing process in an optically thick gas of cold rubidium utilizing the atomic telecom transitions. Importantly, the conversion scheme employs a highly efficient parametric conversion process which is essentially noiseless. By measuring quantum correlations of light fields prior and post to telecom down-conversion, transmission, and up-conversion, a basic memory element for scalable quantum networking is demonstrated.

1.2 Laser Nuclear Spectroscopy of Thorium-229

Achieving long atomic coherence lifetimes is of major importance for long-distance quantum telecommunication, precision measurements, and simulation of model quantum systems. This requires elimination of the dephasing that arises from inhomogeneous external fields and trapping potentials. In atomic fountain experiments, such as those used in establishing time standards, second-scale coherence times have been observed [26]. Quantum information applications require controllable interactions and correspondingly well-defined positions. Common strategies to achieve this involve the use of optical lattices or micro-trap arrays [14, 27–31] with differential a.c. Stark shift compensation [32, 33].
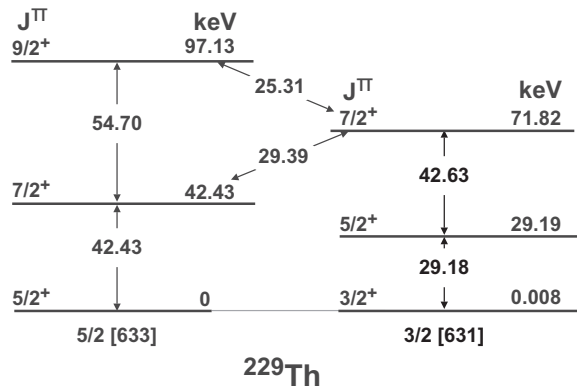
Figure 4: A diagram of the nuclear energy levels of Thorium-229. Quantum numbers are in the Nilsson classification.

An alternative approach is encoding quantum information in a system that is by default weakly coupled to the environment but can exhibit strong interaction on demand. Atomic nuclei can satisfy these criteria, which is utilized in Nuclear Magnetic Resonance (NMR) type experiments where nuclear spin projections serve as a qubit basis. While this approach promises long-lived quantum memories [34, 35], an efficient interaction with such systems is challenging and often requires cryogenic temperatures. Instead of external degrees of freedom, one may utilize internal nuclear states, however the internal nuclear states are unachievable by currently available
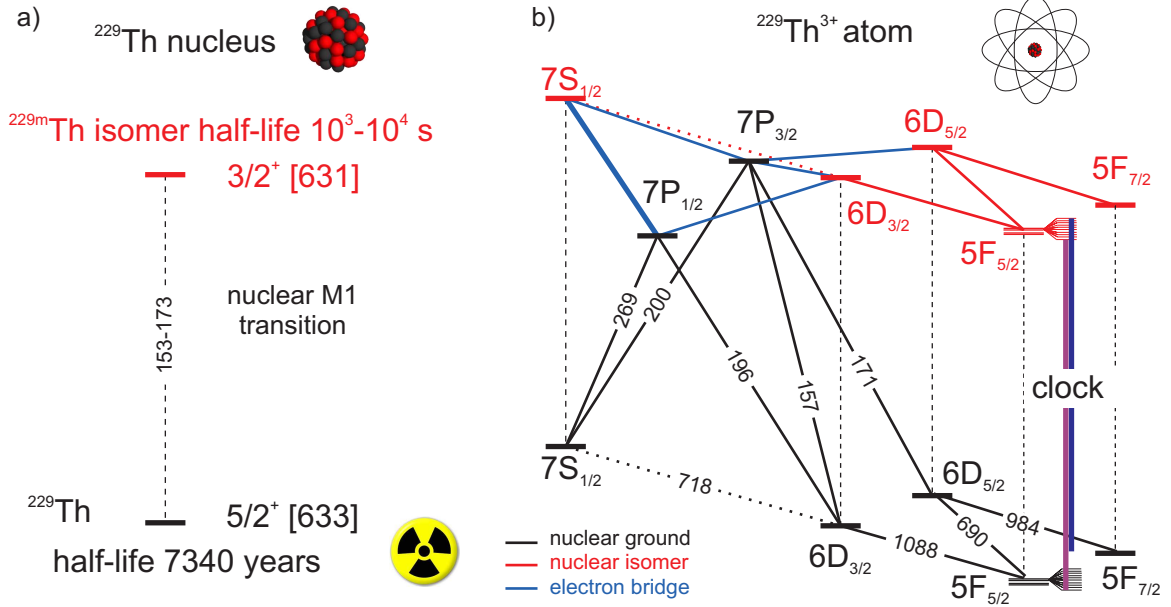
Figure 5: A diagram of electronic energy levels and electric dipole transitions, including both nuclear ground and excited isomeric manifolds. Direct nuclear magnetic dipole (M1) decay channels and electron bridge pathways suitable for the isomer search are shown. Optical transition wavelengths are in nm and the integers near atomic levels indicate principal quantum numbers.

sources of coherent light, since atomic nuclei usually possess excitation energies in the keV to MeV range.

A notable exception is the ^{229}Th nucleus, where the energy splitting of the ground state doublet is less than 10 eV [36–39], as shown in Fig.4. Due to the superb isolation of the nucleus from external fields, and the intrinsic narrowness of the nuclear transition, ^{229}Th may form the basis of a next-generation optical clock [7, 40] and a long-lived qubit. The ground $5F_{5/2}$ electronic levels of the ground and isomer manifolds (Fig. 5) can form a clock with a predicted inaccuracy of 10^{-19} [7], corresponding to hour-scale quantum memory. A convenient set of electronic transitions in the triply charged form of the Th atom may be utilized for the optical preparation and read-out of the nuclear ground and isomer manifolds. If the isolation from the environment is sufficiently high, Thorium-229 opens prospects for a solid-state quantum memory or clock [41–43].

Importantly, the ground-isomer nuclear transition may be used to search for the temporal variation of fundamental constants by monitoring the ratio of the frequencies of the nuclear transition and that of an atomic (electronic) clock transition, e.g., in Al^+ or Sr [3, 44]. Flambaum et al. have predicted that such a frequency ratio is likely to be supremely sensitive to the relative variation of the strong interaction parameter and the fine structure constant, with enhancement factor K possibly reaching as high as 10^6 [8, 45, 46]. Although the complexity of this nuclear system makes a theoretical evaluation of K difficult [47, 48], optical and microwave spectroscopy of the ground and isomer level manifolds should provide a reliable empirical determination of the enhancement factor with little or no dependence on the nuclear model assumed [49].

Since the discovery of the low-lying isomer state in Thorium-229 in 1976, this isomer transition has not been directly observed due to the large frequency uncertainty of ~ 1 PHz [36–39]. The isotope's radioactivity, zero natural abundance, complex energy levels structure, and low optical scattering rates complicate the search for this unique nuclear transition.

This work is a step towards directly exciting the optical domain nuclear transition in Thorium-229 with laser light. Chains of laser-cooled $^{229}Th^{3+}$ ions were obtained in a linear Paul trap, and excitation to a high-lying electronic state for the search of the isomer transition via an electron bridge was accomplished. Once the isomer energy value is measured, either in the system presented here or using one of the other approaches [41, 50], a single trapped, cold $^{229}Th^{3+}$ ion is expected to be an ideal system for taking advantage of this remarkable nucleus.

1.2.1 Trapping, laser cooling, and spectroscopy of $^{229}Th^{3+}$

Since the first demonstration of laser cooling in 1978 [51], dozens of neutral and charged species have been laser cooled, notably starting with alkali elements Li, Na, K, Rb, Cs, Fr; noble gases in metastable states Ne*, Ar*, Xe*, Kr*; alkali-like ions

Be$^+$, Mg$^+$, Ca$^+$, Ba$^+$; and more complex structured atoms like Hg$^+$, Yb$^+$, In$^+$, Sr, Yb, Er, Cr, Dy. Typically, strong closed transitions which provide scattering rates on the order of 10 MHz are utilized to overcome heating mechanisms and cool the atoms down to the Doppler ~ 1 mK or sub-Doppler $\sim 1\,\mu$K limits. However, the energy level structure of Th, Th$^+$, and Th^{2+} contains many metastable states requiring an impractical number of repumping lasers. While there are suitable cooling transitions in Th^{3+}, the scattering rate is limited to 150 kHz due to the microsecond lifetimes of the excited states. Nevertheless, laser cooling of ^{232}Th^{3+} has been demonstrated by Campbell et al. [52], which was also the first demonstration of the laser cooling of a multiply charged ion.

In spite of the advancements prior to this work, obtaining laser cooled ^{229}Th^{3+} is challenging for the following reasons. The natural abundance of the 229 isotope is zero, hence only microscopic amounts of ^{229}Th^{3+} are available. In contrast to the zero nuclear spin of the 232 isotope, the nuclear ground state of ^{229}Th^{3+} has spin 5/2, which combined with the large electron angular momentum of up to 7/2 results in a complex hyperfine structure. Neither the hyperfine structure, nor the electronic transition frequencies, were known well enough for laser cooling. Piece by piece these problems were solved; the methods used are described in this work. The procedure for locating the unknown hyperfine structure and isotope shift will be useful for identifying for the first time the unknown hyperfine structure and the isomer shift of the ^{229m}Th^{3+} isomer state once the isomer state is populated.

In Chapter V, the apparatus and experimental procedures for creating, trapping and laser cooling ^{229}Th^{3+} are described. In Chapter VI, Section 1, the procedure for finding ground state electronic transitions with unknown hyperfine structures is presented. In Section 2 of the same chapter, a protocol for searching for forbidden transitions in Th^{3+} is demonstrated by locating the 717 nm electronic electric quadrupole transition. In the last sections of Chapter VI, the lifetime measurement

of the $7S_{1/2}$ metastable state and spectroscopy of the 269 nm line are presented for the nuclear isomer search via an electron bridge.

CHAPTER II

MULTIPLEXED QUANTUM MEMORY

This chapter is based on Ref. [53].

A quantum memory array is demonstrated for the first time. It is realized in a gas of cold Rubidium atoms by spatially dividing the gas into 12 independently addressable memory elements. Having established conditions so the elements operate independently to a sufficient degree, it is shown that arbitrary element pairs can be coherently addressed, generating matter-light entanglement. This multiplexed quantum memory can increase the rate of entanglement distribution by several orders of magnitude and lower the requirements on memory lifetime.

2.1 *Experimental setup*

The quantum memory array, illustrated in Fig. 6, is produced by dividing a cold cloud of ^{85}Rb atoms (prepared in a MOT of diameter 2.6 mm and with a temperature of $\simeq 100$ μK) into separate elements. These are addressed by a frequency-controlled deflection of laser beams using four AODs with 50 MHz central frequencies and RF bandwidths (full width at half maximum) $\Delta f = 30$ MHz, so that element $j = 1, .., 12$ is addressed with a RF field of frequency $f_j = (36 + 1.8j)$ MHz. These AODs also serve as dynamic phase-controlled beamsplitters, enabling the generation and verification of matter-light entanglement for an arbitrary pair of memory elements. The waist of the write/read modes is 115(3) μm, while that of the signal and idler fields is 30(6) μm); beam waist is defined as the half-width at $1/e^2$ of maximum intensity.

The protocol begins with atoms being prepared in level $|b\rangle$ and released from the trap with the magnetic field, trapping, and repumping light are switched off. In order to create a spin-wave excitation in one of the elements, a sequence of 250 ns long write
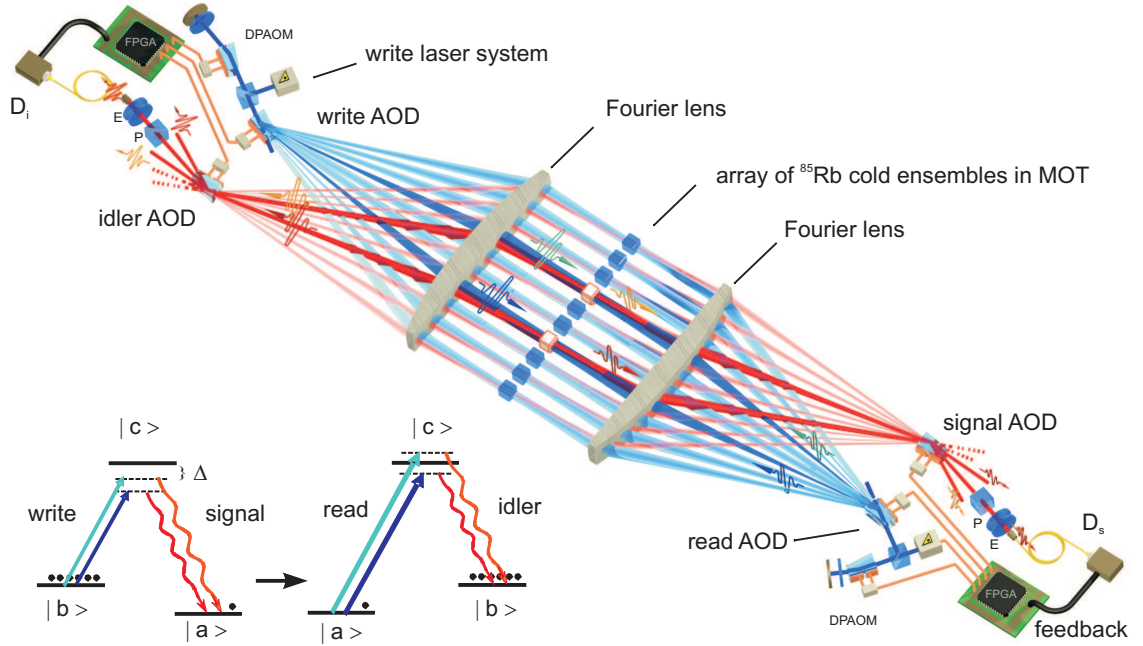
Figure 6: A cold sample of ^{85}Rb atoms is produced in a magneto-optical trap (MOT). The atoms are addressed with laser beams whose positions are controlled by acousto-optic deflectors (AODs), followed by a 10 cm focal length Fourier lens, used to map angular deflection into spatial translation. One pair of AODs mode-matches the write and read beams, determining the array element locations, while another pair collects the scattered signal and idler fields which are directed into single photon detectors (D_s and D_i, respectively) through etalon (E) and polarization filters (P). The signal(write) mode of each element is coupled into the idler(read) fiber mode with about 75% efficiency. The position of the four intersecting beams is controlled by simultaneously varying the AOD drive frequencies by means of a field-programmable gate array (FPGA). The four-wave mixing condition, $\mathbf{k}_w^{(j)}+\mathbf{k}_r^{(j)} = \mathbf{k}_s^{(j)}+\mathbf{k}_i^{(j)}$, is satisfied for each array element j by using telecentric scanning. The write and read light frequency shifts are compensated by additional AODs in a double-pass configuration (DPAOM). The measured average separation between array elements is 230 μm. The two highlighted elements represent a matter qubit, in which an atomic spin-wave in one of the elements represents logical 0, and in the other logical 1, see text for details. The atomic energy level diagram shows the Raman scattering sequence of write and read laser excitation and retrieval employed in the quantum memory, where $|a\rangle = |5s_{1/2}, F = 2\rangle, |b\rangle = |5s_{1/2}, F = 3\rangle, |c\rangle = |5p_{1/2}, F = 3\rangle$; the write field detuning $\Delta = 10$ MHz.

laser pulses of 3 μW power separated by 1.3 μs illuminate the memory array, with one pulse per element (see Fig. 6). The signal AOD is synchronously driven to direct the scattered signal field into a single mode collection fiber coupled to a photoelectric detector. If a signal field photoelectric event is not detected, a 100 ns long cleaning pulse of 10 μW power resonant with the $|a\rangle - |c\rangle$ transition returns the atoms to level $|b\rangle$. Once a signal photodetection event is recorded, the write process is stopped, and the FPGA measures the time of this event with a resolution of 5 ns. After a further 10 μs delay, the spin-wave excitation is converted to the idler field using a 200 ns long read laser pulse of 500 μW power. An idler field photoelectric detection event terminates the protocol. This sequence is repeated at a frequency of 6.1 kHz for approximately 100 cycles over a period of 14 ms, and the retrieval efficiencies of each element are measured. The retrieval efficiency of element k is defined as the ratio of the number of signal-idler coincidence counts $C_{si}^{(k)}$ to the number of signal counts, $C_s^{(k)}$, over the data acquisition period $\eta^{(k)} \equiv C_{si}^{(k)}/C_s^{(k)}$. The central element has the largest retrieval efficiency, 2.1%, while the array average is 1.1%.

2.2 *Quantum Memory Array Size*

The total number of elements in the array is an important parameter to maximize. This parameter depends on the physical size of the interacting media, scanning ability of the addressing device, and the requirements on access time and crosstalk between elements. In our case, the maximum number of elements in a linear array is limited by the light beam scanning range $\theta D/\lambda$, where θ and $D = 0.3$ mm are the angular range and aperture diameter of the scanning element and $\lambda = 795$ nm is the wavelength of light. For an AOD, the angular range is $\theta = \lambda \Delta f/V$, where $V = 660$ m/s is the velocity of sound. Therefore, the number of elements that can be addressed is $N \simeq \Delta f \Delta T$, where $\Delta T = D/V \simeq 0.4$ μs is the access time; for the parameters of our experiment, $N \sim 10$.

It is important to make sure that the crosstalk is sufficiently small. The degree of crosstalk experienced by a given element can be quantified by perturbing its nearest neighbors prior to read-out and comparing the read-out efficiency with that measured in the absence of perturbation. Specifically, our perturbation consists of 10 cleaning pulses sent to each of the two nearest neighbors of the excited element; for edge elements, 20 pulses are sent to the neighboring element. We extract the average crosstalk $\kappa = \langle \kappa^{(k)} \rangle$ assuming $\eta_p^{(k)} = (1 - \kappa^{(k)})^{20} \eta^{(k)}$, where $\eta^{(k)}$ is the read-out efficiency without perturbation and $\eta_p^{(k)}$ is the perturbed efficiency for element k.

Measured in this way, the crosstalk can be estimated assuming the linear dependence of the retrieval efficiency on the atomic population: $\eta = \alpha \sum_{m=-F_b}^{F_b} N_{sw}^{(m)}$, where $N_{sw}^{(m)}$ is an effective number of atoms in the mth Zeeman sublevel of the $|b\rangle$ state and α is a normalizing coefficient. After one cleaning pulse, the perturbed retrieval efficiency is $\eta_p = \alpha \sum_{m=-F_b}^{F_b} N_{sw}^{(m)} (1 - p_{b \to c}^{(m)})$, where $p_{b \to c}^{(m)} c = \int_{-\infty}^{\infty} \gamma \rho_{ee}^{(m)}(t) dt$ is the $|b, m\rangle \to |c, m\rangle$ transition probability. In the limit of a small crosstalk, the total crosstalk is $\kappa = N \kappa_1$, where N is the number of cleaning pulses and $\kappa_1 = 1 - \eta_1/\eta$ is the crosstalk after one pulse. Therefore, the crosstalk is

$$\kappa_1 = 1 - \frac{\alpha \sum_{m=-F_b}^{F_b} N_{sw}^{(m)} (1 - p_{b \to c}^{(m)})}{\alpha \sum_{m=-F_b}^{F_b} N_{sw}^{(m)}} = \sum_{m=-F_b}^{F_b} w_m p_{b \to c}^{(m)}, \tag{1}$$

where w_m is a normalized population of the mth sub-level: $w_m = \frac{N_{sw}^{(m)}}{\sum_{m=-F_b}^{F_b} N_{sw}^{(m)}}$.

The weights of the Zeeman sublevels w_m can be calculated as a sum of decay probabilities to the mth sub-level from the excited state, accounting the population distribution of the excited state defined by a linearly polarized write pulse: $w_m = \frac{X_m^{(-1)} + X_m^{(+1)}}{\sum_{m=-F_b}^{F_b} (X_m^{(-1)} + X_m^{(+1)})}$, $X_m^{(q)} = (C_{m-q\ q\ m}^{Fc\ 1Fb} C_{m-q\ 0\ m-q}^{Fa\ 1\ Fc})^2$, where $C_{m\ q\ m'}^{F\ lF'}$ are Clebsch-Gordan coefficients. There are only σ^+ and σ^- decay channels, since a signal photon is detected with a linear polarization perpendicular to the write pulse polarization. In the case of $F_a = 3$, $F_b = 2$, $F_c = 3$, mostly $|m| = 2$ sub-levels are populated: $w_{\pm 2} = 34/91$, $w_{\pm 1} = 10/91$, $w_0 = 3/91$.

The transition probability $p_{b \to c}^{(m)}$ due to the linearly polarized Gaussian cleaning pulse exciting $\Delta m = 0$ transitions was calculated numerically using Optical Bloch Equations, given that the pulse length is comparable to the decay rate $\tau \sim 1/\gamma$, such that the system is not in a steady state. The result is very close to a steady state with a correction factor of $\chi(\tau) = 0.7$ for $\tau = 47$ ns for the Gaussian intensity profile $I(r,t) = I_0 \, e^{-(t/\tau)^2 - 2(\frac{r-d}{w})^2}$, where the peak intensity $I_0 = 0.24$ mW/cm^2, pulse duration $\tau = 47(12)$ ns, ensembles separation $d = 233$ μm, read waist $w = 115$ μm, and r is a radial coordinate. The steady excited state population is $\rho_{ee}^{(m)}(r) = (\frac{\Omega^{(m)}(r)}{\gamma})^2 = (\frac{4d_{(m)}^2}{c\epsilon_0\hbar^2\gamma^2})\frac{I(r,0)}{2} = \frac{I(r,0)}{2I_{sat}^{(m)}}$, where $\Omega^{(m)}(r,t) = \frac{d_{(m)}E(r,t)}{\hbar}$, is the Rabi frequency of the π transition $|b,m\rangle \to |c,m\rangle$, $E^2(x,t) = \frac{2I(x,t)}{c\epsilon_0}$, where c is the speed of light, ϵ_0 is the permittivity of vacuum, $d_{(m)}$ - dipole moment matrix element for the π $|b,m\rangle \to |c,m\rangle$ transition. The saturation intensity for a π transition from the mth level is $I_{sat}^{(m)} = \frac{c\epsilon_0\hbar^2\gamma^2}{4d_{(m)}^2}$. At distance r, the crosstalk is:

$$\kappa_1(r) = \sum_{m=-F_b}^{F_b} w_m \int_{-\infty}^{\infty} \gamma \frac{I_0 \, e^{-(t/\tau)^2-2(\frac{r-d}{w})^2}}{2I_{sat}^{(m)}} dt = \sqrt{\pi}\gamma\tau I_0 e^{-2(\frac{r-d}{w})^2} \sum_{m=-F_b}^{F_b} \frac{1}{I_{sat}}, \quad (2)$$

where $\frac{1}{I_{sat}} = \sum_{m=-F_b}^{F_b} \frac{w_m}{I_{sat}^{(m)}} = \sum_{m=-F_b}^{F_b} \frac{4d_{(m)}^2 w_m}{c\epsilon_0\hbar^2\gamma^2}$ is the effective saturation intensity for the population distribution w_m; for our scheme, $I_{sat} = 6.89$ mW/cm^2.

Finally, the crosstalk averaged over a spatial Gaussian distribution of a spin-wave $e^{-2(\frac{r}{w_s})}$, where w_s is the waist of a signal mode, is:

$$\kappa = \frac{\int_{-\infty}^{\infty} e^{-2(\frac{r}{w_s})^2} \kappa(r)dr}{\int_{-\infty}^{\infty} e^{-2(\frac{r}{w_s})^2} dr} = \sqrt{\pi}\chi(\tau)\frac{\zeta I_0 e^{-2(\frac{\zeta d}{w})^2}}{2I_{sat}} \gamma\tau, \quad (3)$$

where $\zeta = 1/\sqrt{1+(w_s/w)^2}$ - factor of the spatial overlap of the modes.

The calculated crosstalk of 1.0(5)% for the parameters used in the experiment is in a good agreement with the average value of 1.5(6)% measured for 12 elements in the linear array. The crosstalk could clearly be reduced by increasing d and reducing the RF noise of the AOD driving field. The crosstalk between different elements due

14
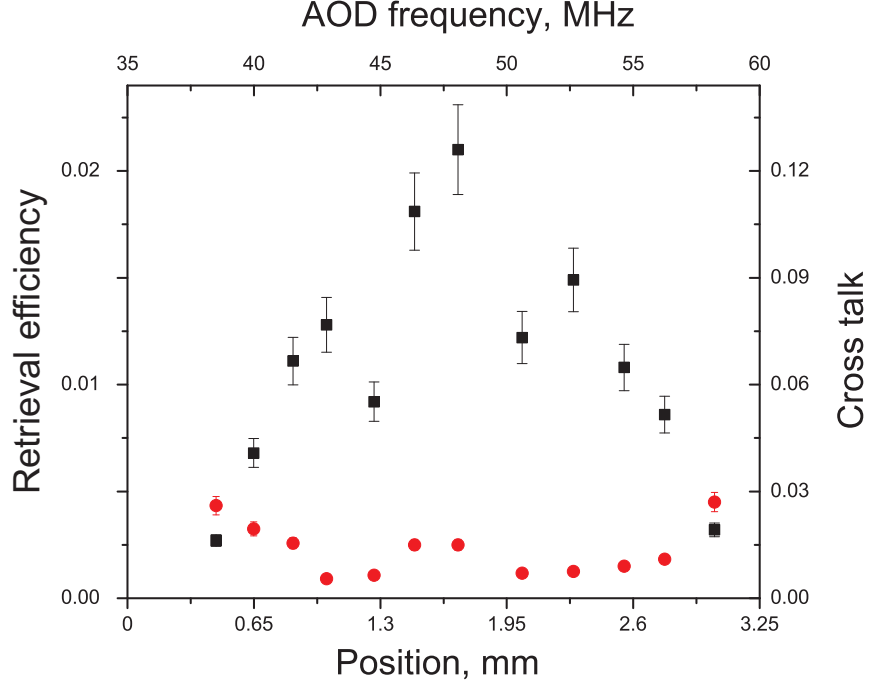
Figure 7: Measured idler efficiency for different elements: each frequency represents a different element location (bottom axis), corresponding to the AOD scanning frequencies (top axis). The right axis shows cross-talk per cleaning pulse.

to atomic motion is negligible, since the average atomic velocity in the MOT is $v \sim$ 0.1 m/s and the displacement s of an atom during a spin-wave storage time of 10 μs is about 1 μm, and therefore $s \ll d$.

2.3 Entanglement in a multiplexed quantum memory

With crosstalk at the level of 1-2%, a matter qubit is created using the two arbitrary elements (j, k) of the array. The matter qubit is ideally entangled with a light qubit, which is encoded in the corresponding spatial modes of the signal field. The matter-light entanglement is investigated by measuring the violation of Bell's inequality for the signal and idler fields scattered from elements j, k.

Two spatially separated write pulses of 250 ns duration illuminate ensembles j and k, simultaneously generating the signal field by Raman scattering. The two spatially distinct write pulses are generated by providing the AOD aligned in the $+1$

diffraction order with two different frequencies $f_j > f_k$ corresponding to ensembles j and k. To compensate for the dependence of the excitation probability on write field frequency, we adjust the corresponding write field intensities. An atomic spin-wave in elements j, k represents logical $|0\rangle, |1\rangle$, respectively. This matter qubit, subscript "a," is entangled with the photonic qubit, subscript "p," represented by the signal field in modes j, k corresponding to logical $|0\rangle, |1\rangle$:

$$\frac{|1\rangle_a^{(j)}|1\rangle_p^{(j)} + e^{i\phi_s}|1\rangle_a^{(k)}|1\rangle_p^{(k)}}{\sqrt{2}} = \frac{|1\rangle_a|1\rangle_p + e^{i\phi_s}|0\rangle_a|0\rangle_p}{\sqrt{2}} \tag{4}$$

After a 150 ns delay, the element j and k spin-wave excitations are converted to idler fields with two read pulses of 200 ns duration generated by an AOD aligned in the $+1$ diffraction order and driven by frequencies f_j and f_k as before. The read pulses are detuned by $\pm(f_j - f_k)/2$ from the $|a\rangle \to |c\rangle$ transition, for elements j and k, respectively.

We measure the joint signal and idler field photodetection rate $C_{si}^{(j,k)}$ as a function of the signal and idler phases, ϕ_s and ϕ_i. The latter are varied by adjusting the phases of element k's signal and idler AOD RF driving fields with respect to those of the write, read signal fields (Fig. 8), which are transferred to the optical phases via Bragg diffraction in the acousto-optical deflectors.

It is important to arrange the radio frequency signals and the AOD diffraction orders properly in order to obtain stable interference fringes independent of the RF generator's frequency drifts of $\sim 10^{-9}$/day. During a typical data acquisition time of one hour at 50 MHz frequency, this drift can produce a phase shift on the order of $2\pi \times 50 \cdot 10^6 \times 10^{-9}/24 \times 3600 = 15\pi$. This phase shift reduces the interference visibility to zero.

In order to avoid the visibility reduction due to the phase drifts, the write/read fields are created by the $+1$ diffraction order while the signal/idler fields are directed to the signal/idler AOD, aligned in the -1 diffraction order and driven by the same RF
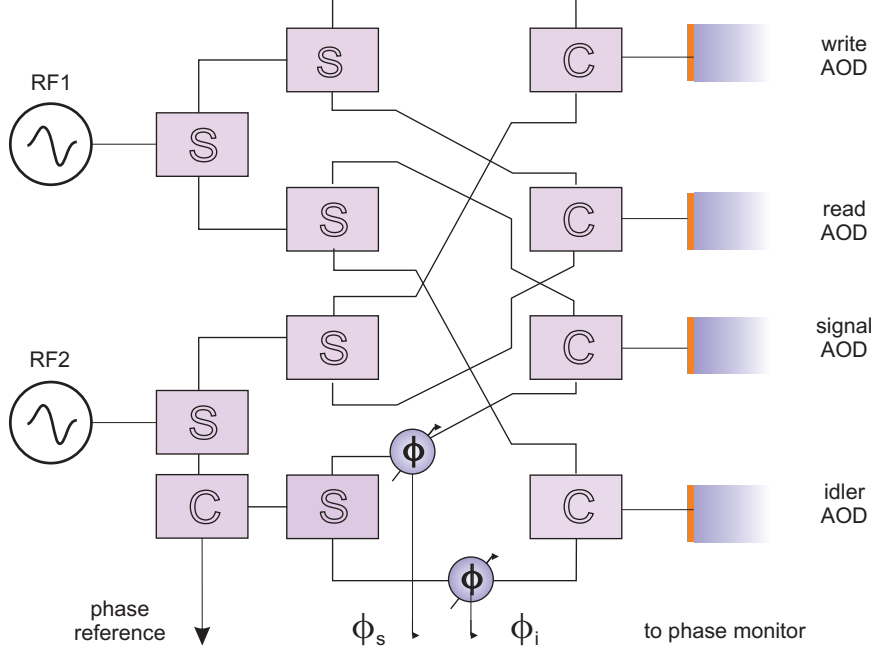
Figure 8: Essential elements of radio frequency generation for acousto-optical deflectors. RF1 and RF2 are the radio frequency function generators. S/C are power splitter/combiners. D is a directional coupler, ϕ is a variable phase shifter. The phase shifters are capable of shifting a signal by 20 ns with a resolution of 1 ns, and BNC barrel adapters are used to obtain an accuracy of 0.5 ns. This corresponds to phase shifts of up to 2π with several degrees of accuracy.

signals as the write/read fields. As a result, the random phase of each RF generator is added to the write field and then subsequently subtracted from the signal field. Therefore, the relative phase of the two signal fields is insensitive to the phase drifts of the RF sources.

Furthermore, the signal/idler fields traverse the same optical elements and as a result the interferometer is passively stable. The stability has been confirmed experimentally by monitoring the interference fringes over several weeks.

We observe the characteristic sinusoidal dependence $C_{si}^{(j,k)}(\phi_s, \phi_i) \propto 1 + V^{(j,k)} \cos(\phi_i + \phi_s)$, where $V^{(j,k)}$ is the visibility. Joint signal-idler detection data is shown for various element pairs in Fig. 9 and Table 1. These show high visibility fringes in all cases, including the (1,12) pair corresponding to the edge elements where the frequency detuning of write and read fields is largest. The measured visibility deviates from its

17
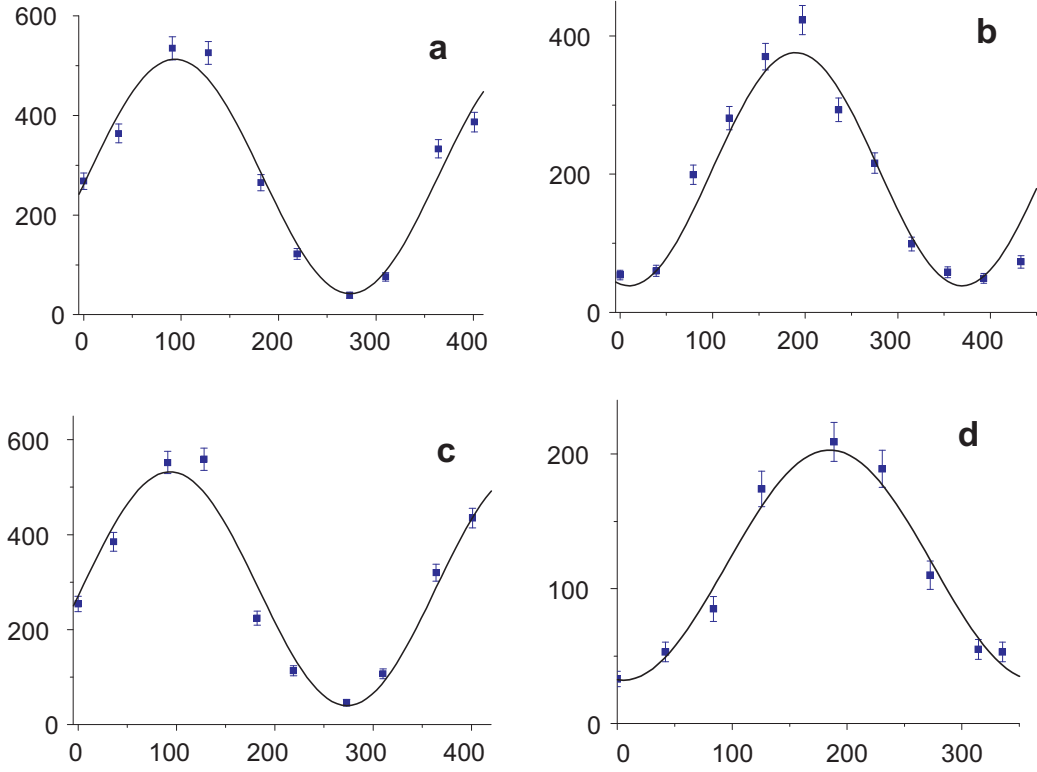
Figure 9: Measured coincidence fringes as functions of a signal phase ϕ_s, corresponding to array elements (7,8) (a), (5,10) (b), (7,10) (c), and (1,12) (d). Sinusoidal fits give corresponding visibilities 0.86(2), 0.81(2), 0.79(1), 0.73(3). Each data point has an acquisition time of 5 min. The effective repetition rate is 100 kHz and each trial takes 1.5 μs. Error bars represent a ± 1 standard deviation based on photoelectron counting statistics.

Table 1: Measured interference visibility V_{exp} and retrieval efficiency η_i for different combinations of quantum memory elements (j, k); V_{bal}^{max} is the visibility corresponding to g_{si}^{max}, the measured value of the normalized cross-correlation function.

j	k	V_{exp}	V_{bal}^{max}	g_{si}^{max}	$\eta_i, 10^{-2}$
5	8	$88 \pm 1\%$	88.9%	17	0.9
7	8	$86 \pm 2\%$	91.7%	23	1.0
7	10	$79 \pm 1\%$	90.5%	20	0.8
5	10	$81 \pm 2\%$	88.9%	17	0.9
1	12	$73 \pm 3\%$	88.2%	16	0.8

maximum expected value $V_{bal}^{max} = 1 - 2/g_{si}^{max}$ because of the imbalance of g_{si} values for the elements in a pair: $V \equiv \frac{C_{si}^{max} - C_{si}^{min}}{C_{si}^{max} + C_{si}^{min}} \approx \frac{2\sqrt{g_{si}^{(j)} g_{si}^{(k)}}}{g_{si}^{(j)} + g_{si}^{(k)}}$, for $g_{si}^{(k,j)} \gg 1$. The measured visibilities are greater than the minimum visibility for the Bell inequality violation of $1/\sqrt{2} \approx 71\%$, therefore any pair could form an operable matter-qubit.
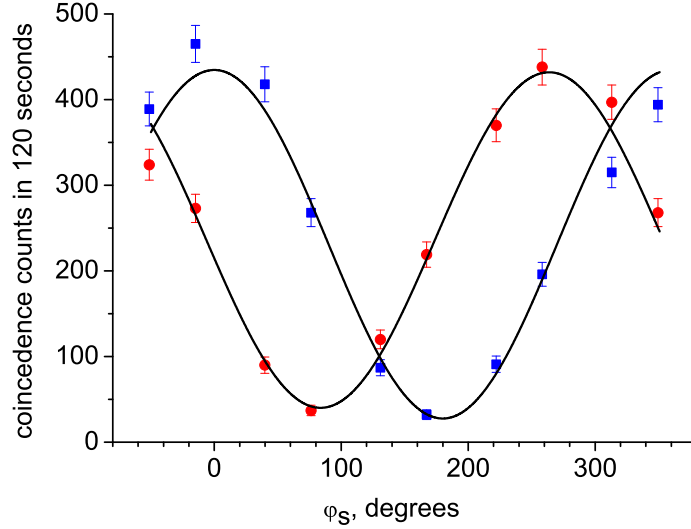
Figure 10: Interference fringe of coincidence counts from elements number 5 and 8 as functions of ϕ_s for $\phi_i=0°$, squares and $\phi_i= 90°$, circles. The solid curves are fits by a function $C_s \eta_i (1 + V \cos(\phi_i + \phi_s + \phi_0))/2$ with visibilities V =(0.88(2), 0.83(2)) and phase offsets ϕ_0=(0(1)°, 5(3)°) for curves with $\phi_i = 0°$ and $\phi_i = 90°$, respectively.

Table 2: Measured correlation function $E(\phi_s, \phi_i)$ and S for ensemble 5 and 8.

ϕ_i	ϕ_s	$E(\phi_s, \phi_i)$
$-90°$	$45°$	0.625 ± 0.016
$-90°$	$135°$	0.562 ± 0.017
$0°$	$45°$	0.510 ± 0.018
$0°$	$135°$	-0.683 ± 0.017
		$|S| = 2.38 \pm 0.03$

To investigate matter-light entanglement, elements 5 and 8 were arbitrarily selected for further analysis. In Fig. 10 we show the data for $C_{si}^{(5,8)}$ as a function of ϕ_s for $\phi_i = 0$ and $\phi_i = \pi/2$, respectively, fitted to the normalized correlation function $E^{(j,k)}(\phi_i, \phi_s) = V^{(j,k)} \cos(\phi_i + \phi_s)$ [54–56]. A classical local hidden variable theory yields Bell's inequality $|S| \leq 2$, where the Bell parameter $S \equiv E(\phi_s, \phi_i) + E(\phi'_s, \phi_i) - E(\phi_s, \phi'_i) + E(\phi'_s, \phi'_i)$ and the superscripts j and k are suppressed. Measured values of the correlation function E using the set of angles $\phi_s = 135°$, $\phi'_s = 45°$, $\phi_i = -90°$, $\phi'_i = 0°$, are listed in Table 2 and demonstrates a violation of Bell's inequality, $|S| = 2.38 \pm 0.03$.

In conclusion, a multiplexed array of 12 independent addressable quantum memory elements is demonstrated. Such multiplexed memory elements are essential components of long-distance quantum entanglement distribution in the absence of sufficiently long storage times. Furthermore, one can improve the number of addressable elements by multiplexing in both transverse dimensions. These memory arrays also enable local entanglement generation [57, 58], which, when combined with frequency conversion as described in the following chapters, makes the quantum memory elements compatible with existing low-loss telecommunication channels. Quantum repeaters using such arrays offer communication rates that are several orders of magnitude faster than those achievable through equivalent parallel systems.

CHAPTER III

NON-DEGENERATE NON-COLLINEAR FOUR-WAVE MIXING IN A COLD DENSE ATOMIC GAS

In this chapter, a non-degenerate non-collinear four-wave mixing process with cold atoms is described. In Section 2, the realization of this process in a cold optically thick gas of Rubidium-87 demonstrates low noise wavelength conversion between 795 nm and 1367 nm light fields, achieving efficiencies up to 65%. In Section 2, a novel Extended Dark Magneto-Optical Trap (EDMOT) used to create cold atomic ensembles with optical thicknesses of >150 is described. The extension of the conversion process to an arbitrary polarization of light is presented in Section 4. The high efficiency and noiseless conversion process ensures the preservation of the quantum state of the converted light for applications in quantum optics, as demonstrated in Chapter 4.

3.1 Four-wave mixing

Light-matter interaction is intrinsically a non-linear process, as light can significantly change the state of the matter it interacts with and matter can correspondingly change the state of light. Stark shifts, Rabi oscillations, saturation, and level couplings are examples of this non-linear interaction.

Fig.11 depicts a non-degenerate four-wave mixing process in momentum and energy domains, applied for a wavelength conversion from a near-infrared signal (s), to a telecom field (t) with pump fields (pI) and (pII). The three input electric fields
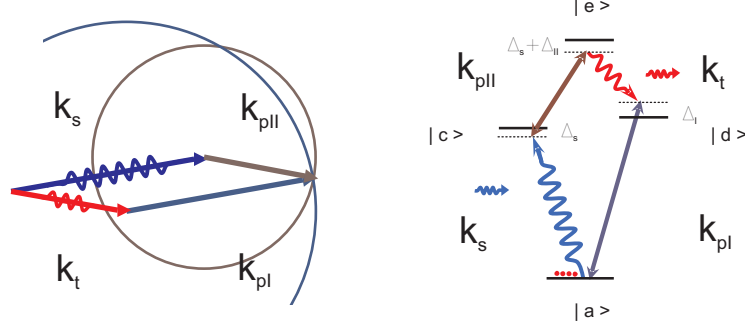
Figure 11: Momentum (left) and energy (right) conservation in a four-wave mixing process. The angle between the two k-vectors originating from the same point is set to a desired angle. Then the circles with radii of the other two fields wavenumbers, originating from the end of the vectors, represent possible orientations of the corresponding fields' wavevectors, and therefore the intersecting points of the two circles are the solutions for the phase-matching condition.

$E_i(t) = E_i e^{i\omega_i t + i\mathbf{k}_i \cdot \mathbf{r} + i\phi_i} + c.c.$, $i = s, pI, pII$ induce the oscillating polarization $\mathbf{P}(t)$:

$$P_i(t) = \epsilon_0 (\sum_j \chi_{ij} E_j(t) + \sum_{jk} \chi_{ijk}^{(2)} E_j(t) E_k(t) + \sum_{jkl} \chi_{ijkl}^{(3)} E_j(t) E_k(t) E_l(t) + ...) =$$

$$= P_i^{(\text{lin})}(t) + \chi^{(3)} E_s E_{pI} E_{pII} e^{i(\omega_s - \omega_{pI} + \omega_{pII})t + i(\mathbf{k}_s - \mathbf{k}_{pI} + \mathbf{k}_{pII}) \cdot \mathbf{r} + i(\phi_s) - \phi_{pI} + \phi_{pII}} \tag{5}$$

where $P_i^{((\text{lin})}$ is the linear component of the polarizability, ϵ_0 is the vacuum permittivity, E_i are the electric field components. Only the resonant electric susceptibilities χ are kept in the expression (5). The oscillating dipole moment density $\mathbf{P}(t)$ generates the corresponding electric field $E^{(t)} = E_0^{(t)} e^{i\omega^{(t)}t + i\mathbf{k}^{(t)} \cdot \mathbf{r} + i\phi^{(t)}}$, with the frequencies, wavevectors and phases satisfying the following energy conservation and phase-matching conditions (Fig. 11):

$$\hbar\omega_t = \hbar\omega_s - \hbar\omega_{pI} + \hbar\omega_{pII}, \tag{6}$$

$$\hbar\mathbf{k}_t = \hbar\mathbf{k}_s - \hbar\mathbf{k}_{pI} + \hbar\mathbf{k}_{pII}, \tag{7}$$

$$\phi_t = \phi_s - \phi_{pI} + \phi_{pII}, \tag{8}$$

where $\hbar$ is the reduced Plank constant. The $\chi^{(3)}$ electric susceptibility near atomic resonances, $\Delta_i \sim \Gamma$, can be calculated from the atomic polarizability:

$$\chi^{(3)} \sim \frac{n d_s d_{pI} d_{pII} d_t}{\epsilon_0 \hbar\Delta_s \hbar\Delta_{pI} \hbar\Delta_{pII}}, \tag{9}$$

where n is the atomic concentration, Δ_i are the light frequency detunings from the atomic resonances, Γ is the effective spontaneous emission rate of the excited levels, d_i are the dipole moments of the corresponding atomic transitions. By solving for the propagation equations for the four fields the four-wave mixing efficiency can be derived:

$$\eta = \frac{N_{\text{out}}}{N_{\text{in}}} = \frac{P_{out}\lambda_{\text{out}}}{P_{\text{in}}\lambda_{\text{in}}} = \sin^2(L\chi^{(3)}\sqrt{I_{pI}I_{pII}}\frac{\zeta}{c\epsilon_0\lambda}\text{sinc}(\Delta kL))e^{-\alpha L}, \qquad (10)$$

where L is the length of the media, $I_{pI,II}$ are the intensities of the pumps I, II, $\Delta k = |-\mathbf{k}_t + \mathbf{k}_s - \mathbf{k}_{pI} + \mathbf{k}_{pII}|$ is the phase mis-match factor, c is the speed of light, λ is the effective wavelength of the light fields, $\zeta \sim 2\pi$ is a geometrical factor, α is the linear absorption coefficient, $N_{\text{in/out}}$, $P_{\text{in/out}}$, $\lambda_{\text{in/out}}$ are the number of photons, power, and wavelengths of the input and output fields,. More detailed theoretical analysis of the frequency conversion is given in Refs. [32, 59].

These formulas provide a framework for improving the efficiency of four-wave mixing, suggesting several insights. Due to the exponential dependence on linear absorption a light induced transparency window is required. In the transparency regime the efficiency can be increased with higher optical thickness, $OD = \sigma nL$, because of the $\chi^{(3)}L \sim nL$ factor. A technique for creating a cold sample of $OD = 150$ and a 65 dB transparency regime, realized by light induced transparency due to the pump fields, is described in the following section.

3.2   *Extended Dark Magneto-Optical Trap*

Typical densities of $\sim 10^{10}$ cm^{-3} and optical thicknesses of ~ 30 for laser cooled and trapped atoms in Magneto-Optical Traps (MOTs) are not sufficiently high for an efficient four-wave mixing wavelength conversion. Vapor cells heated above $100\,^{\circ}$C can provide high optical thicknesses, but the Doppler broadening and geometrical factors significantly reduce the efficiency to 10^{-5} [60].
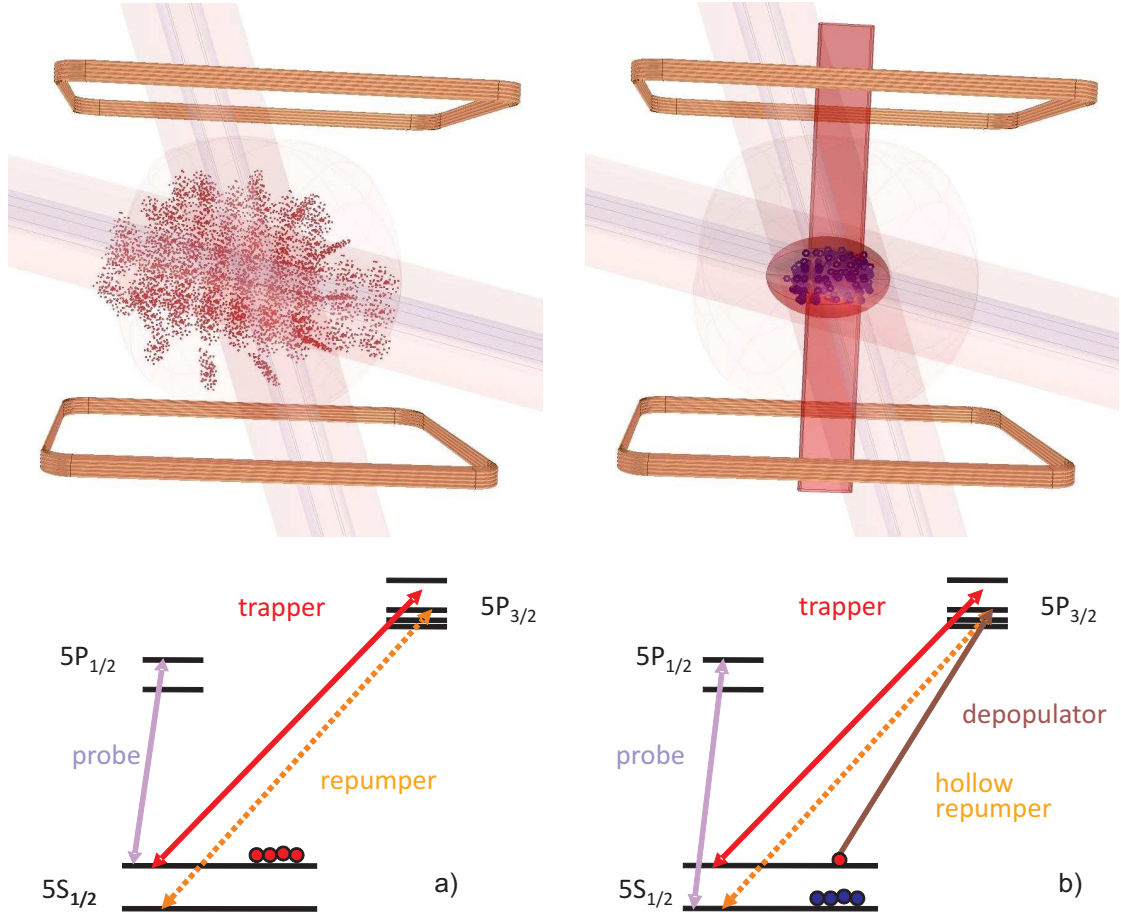
Figure 12: Principle of operation for the Extended Dark Magneto-Optical Trap (EDMOT). In a conventional Magneto-Optical Trap (MOT) (a) atoms are always in a bright state and continuously scatter light. The radiation pressure of this resonant light prevents atoms from condensing beyond $\sim 10^{10}$ cm^{-3}. In the EDMOT (b), the combination of a depopulator field and blocking the repumping field for the central part of the trap transfers cooled atoms into a dark state, reducing the radiation pressure and allows atoms to condense to concentrations of $> 2 \times 10^{11}$ cm^{-3}. The rectangular geometry of the magnetic coils increases the length of the sample, which also reduces radiation pressure in the radial directions and increases nL, the number of atoms per unit of area.
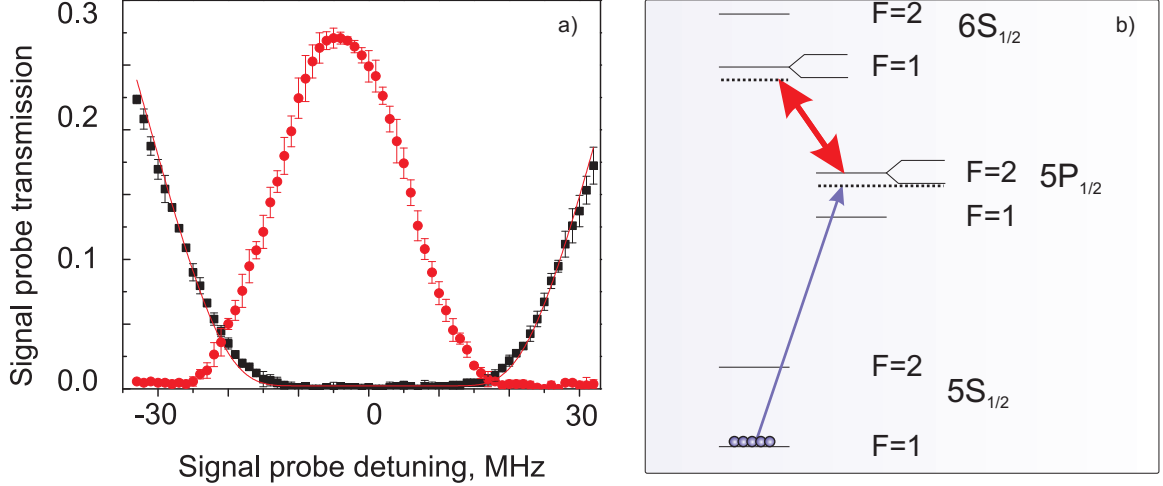
Figure 13: a) Transmission of the signal probe beam (b) through the sample of ^{87}Rb prepared in the extended dark magneto-optical trap. Without the pump fields (squares) the probe field experiences strong absorption (the fit $e^{-OD/(1+(\frac{\omega-\omega_0}{2\Gamma})^2)}$ and gives an on resonance optical depth of 152(2)). When pump II is on (pump I is off) a transparency window is created for the probe field (circles), which increases the transmission by 65 dB.

The atomic density in a MOT is limited by the radiation pressure due to the scattered cooling light. The radiation pressure can be significantly reduced by employing the dark configuration [61] and changing the aspect ratio with the rectangular geometry of the anti-Helmholtz coils [62], as shown on Fig. 12. The modified Extended Dark Magneto-Optical Trap (EDMOT) is based on a conventional MOT by employing two orthogonal hollow repumper beams with a 6 x 4 mm elliptical hole and a retro-reflected depopulator beam of rectangular shape 5 x 1.5 mm. The depopulator beam is detuned from the $|5S_{1/2}F=2\rangle \leftrightarrow |5P_{3/2}F=2\rangle$ transition by 11 MHz and has a power of 0.15 mW, while the repumper is tuned to the $|5S_{1/2}F=1\rangle \leftrightarrow |5P_{3/2}F=2\rangle$ transition. The magnetic field gradient is ∼10 G/cm in the transverse, and ∼4 G/cm in the longitudinal. The trapping beams have diameters (full width at $1/e^2$) of 30 mm, and a total power of 150 mW, detuned from the $|5S_{1/2}F=2\rangle \leftrightarrow |5P_{3/2}F=3\rangle$ transition by -24 MHz. A cigar-shaped ∅ ∼2 mm, L ∼6 mm sample of ^{87}Rb is produced at T ∼150 μK. The atoms are largely in the "dark" state $|5S_{1/2}F=1\rangle$ coinciding

with the initial state for frequency conversion.

The transmission of a 795 nm probe beam, scanned around the F=1 → F=2 transition (Fig. 13a), demonstrates $1/e$ optical thickness (OD) of 152(2), corresponding to a concentration of 2×10^{11} cm^{-3}, about one order of magnitude higher than without a dark modification. The linear absorption can be reduced by 65 dB in the light induced transparency regime, provided by the pump II field at 1324 nm (Fig. 13b). The light induced transparency is a combination of electromagnetically induced transparency and Autler-Townes splitting [63]. The transparency allows the converted fields to escape from the optically thick sample without exponential loss.

3.3   Wavelength conversion with four-wave mixing

Implementing the four-wave mixing scheme (Fig.11) with a cold Rubidium gas prepared in the EDMOT allows for efficient wavelength conversion between 795 nm and 1367 nm for interfacing quantum memory with telecom fibers. The geometry and the level schemes are shown in Fig.14. The signal field at 795 nm is incident on a cold ^{87}Rb atomic sample prepared in the hyperfine ground level $|a\rangle$, driven by the pump I and II lasers near-resonant to the $|a\rangle \leftrightarrow |d\rangle$ and $|c\rangle \leftrightarrow |e\rangle$ electronic transitions, respectively. A telecom 1367 nm wavelength field is generated on the $|e\rangle \leftrightarrow |d\rangle$ transition, consistent with energy and momentum conservation. The spectrum of the telecom field is shown in Fig. 16b. This down-conversion process can be reversed with an up-conversion process, where the incident telecom signal field is up-converted to the near-infrared 795 nm signal field.

In the transparency window, the up- and down- conversion efficiencies η_u and η_d are equal within the measurement accuracy (1 part in 30) and are defined as the ratio of the output number of photons to the input number of photons. The conversion efficiency $\eta = \eta_u = \eta_d$ is a function of optical thickness, three sets of field propagation angles, detunings, gaussian spot sizes, polarizations, and the geometrical overlap
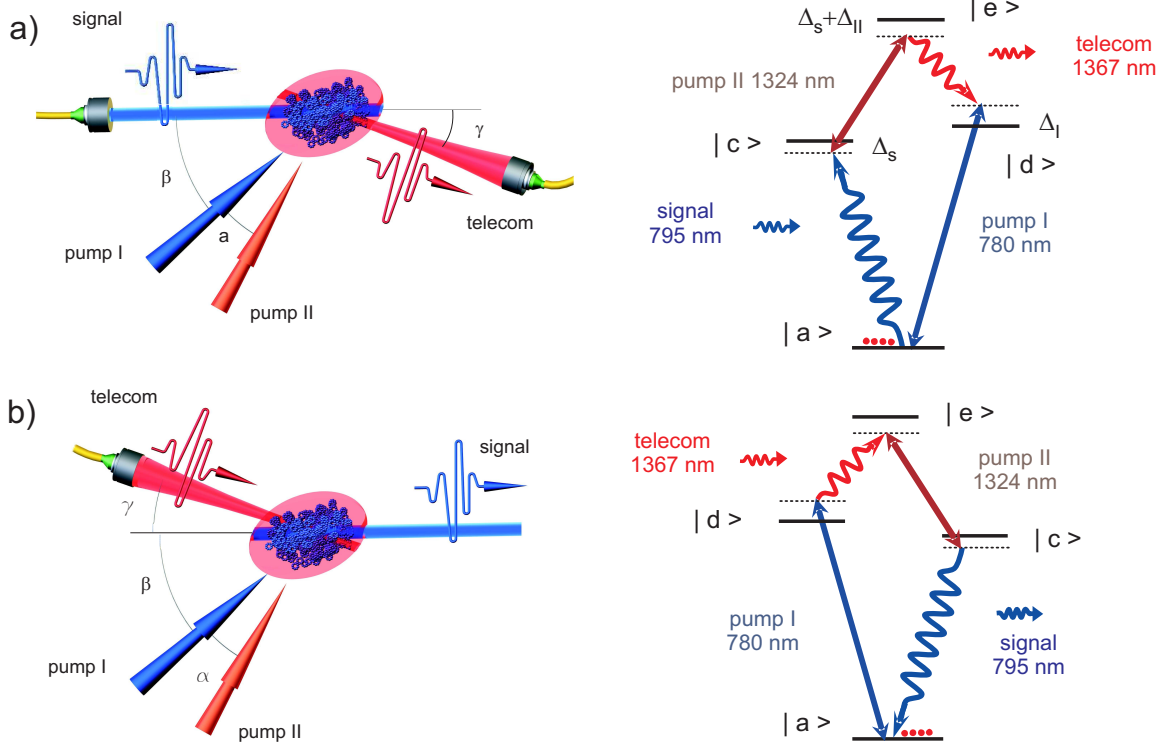
Figure 14: Geometry for frequency (a) down-conversion and (b) up-conversion four-wave mixing process in an optically thick cold gas of Rubidium, prepared in the EDMOT. All of the fields are linearly polarized at -25, 8, 16 and -30 degree angles to the normal of the plane of the wavevectors; the gaussian spot sizes of their modes are 0.55, 0.65, 0.18 and 0.20 mm, respectively. Parameters: $\alpha \approx \gamma = 0.55°$, $\beta = 1.7°$, $\theta = 0.9°$, $|a\rangle = |5S_{1/2}\ F = 1\rangle$, $|b\rangle = |5S_{1/2}\ F = 2\rangle$, $|c\rangle = |5P_{1/2}\ F = 2\rangle$, $|d\rangle = |5P_{3/2}\ F = 2\rangle$, $|e\rangle = |6S_{1/2}\ F = 1\rangle$, $\Delta_s = -2\pi \times 17$ MHz, $\Delta_I = 2\pi \times 41$ MHz, $\Delta_{II} = 2\pi \times 6$ MHz.

between the optical modes and the atoms. After an optimization procedure in this multidimensional phase space with many parameters coupled, the maximum conversion efficiency of 65% is achieved, fully utilizing all available pump power (Fig.15). This conversion efficiency approaches the maximum theoretical efficiency of 80% predicted for an OD of 150 [59]. The bandwidth is measured to be 30 MHz (Fig. 16a), which is likely to be defined by the transparency window, and therefore limited by the intensity of pump II. Finite geometrical overlap of the fields and spontaneous emission limit the efficiency. With more laser power available, the pump field sizes can be increased for better geometrical overlap, and the spontaneous emission can be
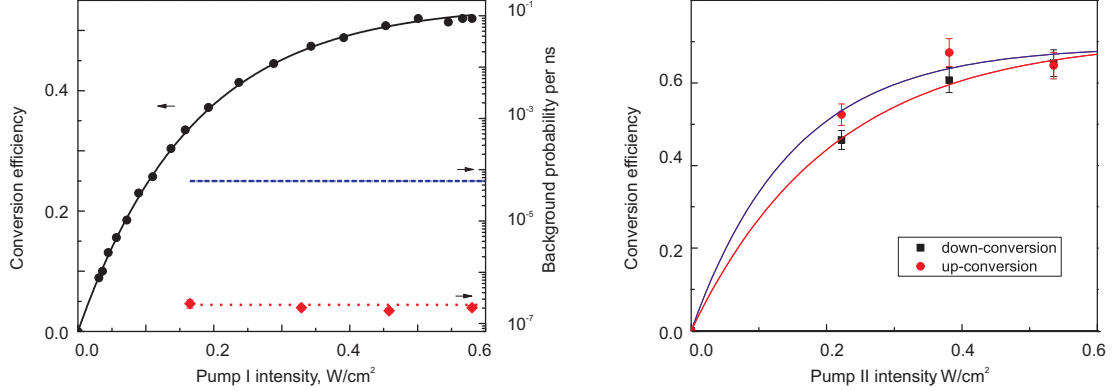
Figure 15: Frequency conversion efficiency η (circles) and noise level (diamonds) of the up-conversion telecom single photon detector as a function of the intensity $I_{pI} \equiv \frac{P_{pI}}{\pi w_{pI}^2}$ of the pump I; here P_{pI} and $w_{pI} = 0.55$ mm are the measured power and the gaussian spot size of pump I, respectively. The solid line is a fit of the form $\eta^{\max}(1 - \exp(-I_{pI}/I_s))$, with $\eta^{\max} = 0.54(1)$ and $I_s = 0.17(1)$ W/cm^2. The dashed line is the noise level of typical InGaAs/InP telecom detectors. Error bars represent ± 1 standard deviation based on photoelectron counting statistics.

reduced with greater detunings, compensated for with higher optical thickness.

Conversion efficiency of up to 30% was observed for the 795 nm $\leftrightarrow$ 1530 nm route (using the $4D_{3/2}$ upper level). The lower efficiency is likely due to the lower oscillator strength of the $5P_{1/2} \leftrightarrow 4D_{3/2}$ transition compared to that of the $5P_{1/2} \leftrightarrow 6S_{1/2}$ transition, but this may be improved by increasing the optical thickness.

In addition to high efficiency, frequency conversion should be a low-noise process for operation at the single photon level. The background noise level is measured by blocking the signal field and determining the probability of photoelectric detection in the signal mode within the 90 ns detection window. As illustrated in Fig. 16, this measured level is about 300 times lower than that of an InGaAs/InP telecom single photon counter. Telecom frequency conversion to near-infrared, together with the use of a silicon photon counter, therefore produces an excellent telecom photon detector.

The low noise is attributed to the non-collinear geometry and non-degenerate scheme, providing at least 130 dB noise suppression. Non-collinear geometry allows
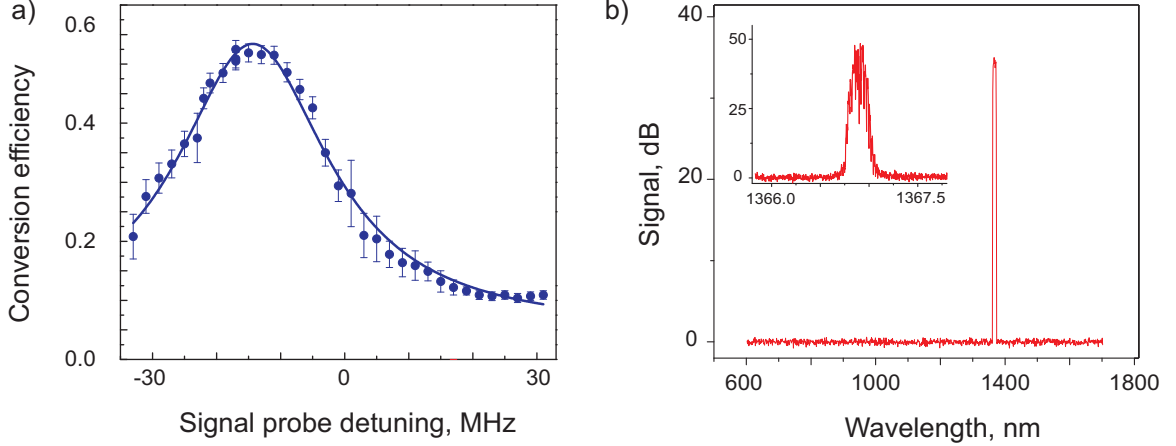
Figure 16: a) Measured frequency conversion efficiency η as the function of probe detuning. A Lorentzian fit gives a bandwidth of 29(3) MHz (full width at half maximum). Error bars represent ± 1 standard deviation based on measurement statistics. b) Measured spectrum of the telecom signal mode with weak laser light at 795 nm injected into the signal mode. The observed spectral linewidth in the inset is that of the optical spectrum analyzer (HP 86142A). The visible structure is due to a combination of limited sampling and the asynchronous relation between the spectrum acquisition and the signal field pulse sequence. The converted field has the expected 0.8 transmission efficiency through a long-pass 1300 nm filter (Thorlabs FEL1300), which attenuates the 780 nm and 795 nm light by more than 5 orders of magnitude.

for the separation of signal modes from the pump modes on the glass of the vacuum chamber, the primary source of the pump light scattering into the signal mode. Separation by 2.6 Gaussian beam waists gives a suppression of $e^{-2(2.6)^2} \approx -60$ dB. Non-degenerate scheme provides substantially different wavelengths, separated by more than 15 nm, such that interference filters can be used. Two such filters can provide an additional 70 dB of suppression.

Table 3: Residual noise of the frequency converter.

Noise source	s^{-1}
Scattering of pump fields	< 10
Fluorescence at 780 nm pump wavelength	< 10
Fluorescence at 795 nm signal wavelength	100
Silicon detector dark count rate	100
Total up-conversion detector dark count rate	200

29

At these low light levels, the non-elastic scattering of 780 nm light in the pump fiber becomes non-negligible even in the 795 ± 5 nm signal detector range, which requires a 5 nm band pass filter at 780 nm after the pump I delivery fiber.

The noise budget is shown in Table 3. It can be seen that the noise is fundamentally limited by the 795 nm fluorescence from the atomic sample. Since the 795 nm signal field is negligibly small, there are no resonant laser fields to excite atoms to the $5P_{1/2}$ level; however, fluorescence at 795 nm still can be detected. It is likely that the $5P_{1/2}$ level is populated with the collision processes of the atoms in the $5P_{3/2}$ level.

3.4 Polarization-independent frequency conversion

Light polarization is a common and convenient basis for a photonic qubit. Telecom frequency conversion therefore has to be polarization-independent to preserve the quantum information encoded in the light polarization. The light induced transparency and the four-wave mixing are polarization-dependent processes. Accordingly, only certain polarizations can be efficiently wavelength converted for a given set of levels. While the scheme involving $4D_{3/2}$ as the upper level allows for polarization-independent conversion, the efficiency is less than half that of the $6S_{1/2}$ upper level scheme. Since two conversion stages are required, this translates to a data acquisition time that is four times longer, undesirable in quantum optics experiments, given the week-scale integration times.

Alternatively, the high-efficiency scheme can be applied separately in time for the orthogonal components of the input field. The transparency condition can be maintained by rotating the polarization of the pumps by $\pi/2$ for each signal field polarization component. In order to maintain the original polarization information, amplitudes of the orthogonal linear polarization components and their relative optical phases have to be maintained.
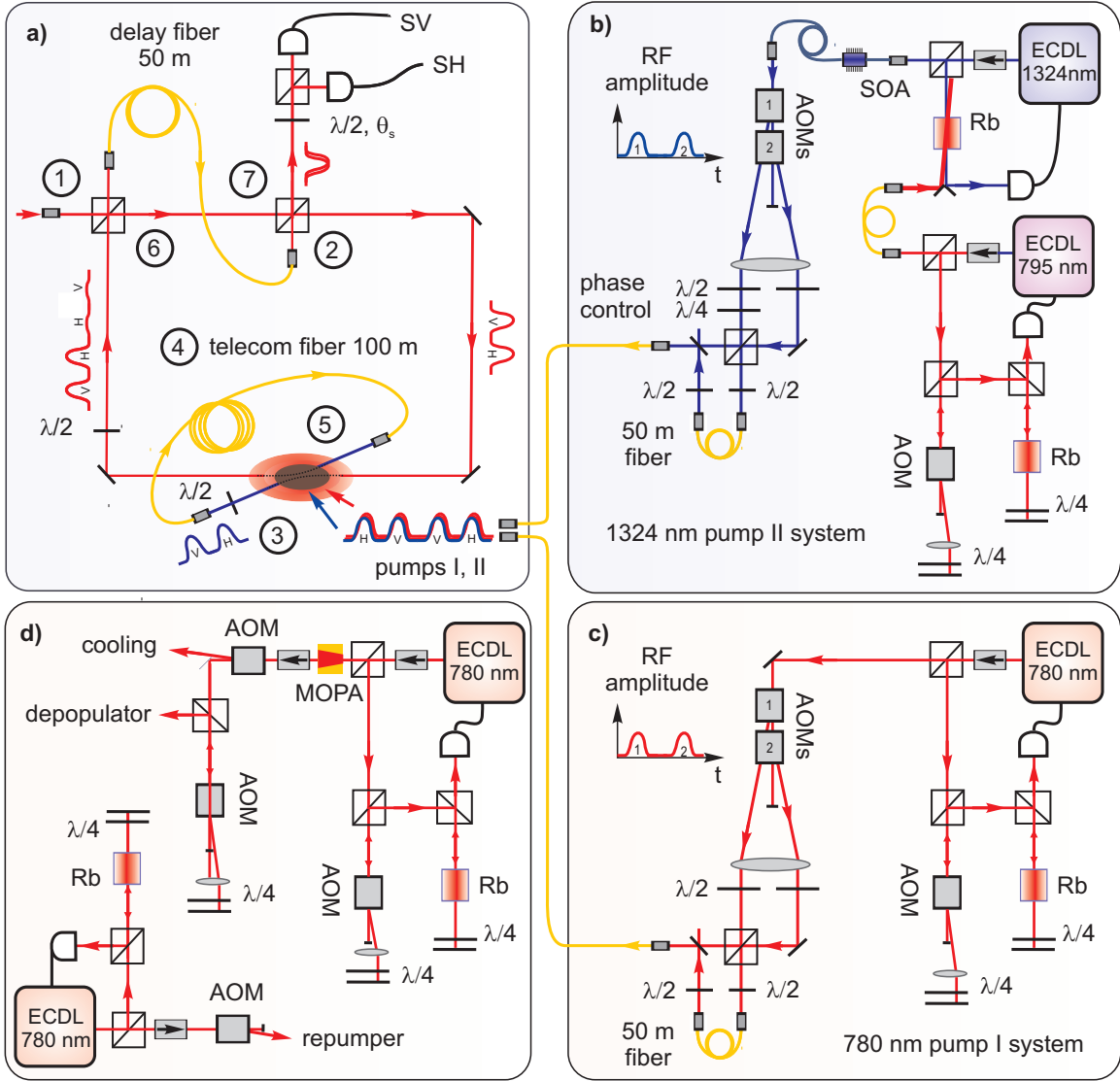
Figure 17: Experimental setup for the frequency conversion of an arbitrary polarization. a) Since the four-wave mixing is optimized only for a linear polarization parallel to the pump polarization, the incoming light is decomposed into two orthogonal polarizations, separated in time, independently converted with appropriate polarization pump pulses, and then recombined while preserving the phase information to maintain the original polarization state. The laser systems utilize External Cavity Diode Lasers (ECDLs). b) The 1324 nm laser is based on a standard 1310 nm telecom diode, producing ~ 2 mW of optical power that is amplified in a Semiconductor Optical Amplifier (SOA) to ~ 100 mW. The 1324 nm laser is locked to a two-photon resonance in a room temperature Rubidium gas with assistance of a 795 nm ECDL. c) The 780 nm pump I system is identical to the pump II system. d) Laser system for providing cooling, depopulator, and repumper beams for operation of the Extended Dark Magneto-Optical Trap (EDMOT).

In addition to the polarization-independent wavelength conversion, the polarization decomposition allows for a polarization qubit rotation by changing the optical phases of the pump fields, that are transferred to the signal fields. This provides compensation for the drifting birefringence of optical fibers and other optical elements between the wavelength converter and the quantum memory setup. The proper arrangement of the conversion sequence, and using the same fiber delay for the decomposition and recombination of the optical fields, ensures that the optical phase between the polarization components of the qubit is not sensitive to fluctuations in the interferometric setup, such that no active stabilization of the optical path is required. This phase noise rejection occurs if the conversion sequence is faster than the phase noise. Since the phase fluctuations are in the acoustic range <50 kHz, the conversion sequence length of 1 μs is sufficiently shorter than the acoustic fluctuation time scale.

A setup for the polarization-independent frequency conversion is presented in Fig. 17 and the evolution of the optical phases is given in Table 4. In step 1, the incoming signal field is decomposed on a polarization beam splitter, so the vertical polarization component is delayed by 235 μs in a 47 m long optical fiber. In step 2, the delayed vertical component is spatially overlapped with the not delayed horizontal polarization component on the second polarization beam splitter.

At the same time, the pump laser systems (Fig.17b,c) generate horizontally and vertically polarized laser pulses separated in time by 235 μs in two other 47 m long optical fibers(Fig. 17b). Two pulses of equal amplitude are created by dividing a laser pulse on a polarization beam splitter preceded by a pair of $\lambda/4$ and $\lambda/2$ waveplates. Changing the angles of the waveplates while maintaining the 50/50 intensity splitting ratio introduces a variable phase shift ϕ_c between the two fields ranging from $-\pi$ to π, which is transferred to the telecom field via the four-wave mixing phase matching condition (8).

Table 4: Phase changes during the down- and up-conversion sequence. "Slow" and "fast" correspond to the delayed and not delayed polarization components of the input field, ϕ_i is the initial phase between horizontal and vertical components of the input field, ϕ_c is the controllable phase introduced with down-conversion pump I pulses, and D_s, D_{pI}, D_{pII} are the phase shifts due to the signal, pump I, pump II delays, respectively.

Step	Result phases (fast, slow)
1	$(\phi_i, 0)$
2	(ϕ_i, Ds)
4	$(\phi_i + \phi_c, D_s - D_{pI} + D_{pII})$
5	$(\phi_i + \phi_c - D_{pI} + D_{pII}, D_s - D_{pI} + D_{pII})$
6	$(\phi_i + \phi_c - D_{pI} + D_{pII} + D_s, D_s - D_{pI} + D_{pII})$
7	$(\phi_i + \phi_c, 0)$

In step 3, these pump pulses are overlapped in space and time with the signal field pulses in the EDMOT satisfying the phase matching geometry, resulting in down-conversion. The generated telecom wavelength pair of vertically and horizontally polarized pulses is directed to a standard SMF-28 telecom fiber of 100 m length, where it propagates for 500 μs (step 4). The half-waveplate swaps the polarizations of the telecom field components such that the first pulse is vertically polarized and the second one has horizontal polarization.

In step 5, the output of the telecom fiber is coupled to the EDMOT, and so the telecom pulses are up-converted with another pair of pump pulses. The second pair of pump pulses for the up-conversion is generated in the same laser system as the first pair, but by using the orthogonal ports of the polarization beam splitters. In this way, the same delay fiber is used, resulting in the cancellation of the random phase shift, introduced by the fiber and optics of the delay line. Both pairs of pump pulses are generated from the same laser beam by using two AOMs in series for maximum utilization of the laser power.

In step 6, the vertical and horizontal components of the up-converted signal field

are split on the original polarization beam splitter, in order that the horizontal component is retarded by the same delay line that was used to delay the vertical components. Consequently, the random phase of the delay line is introduced to both components, therefore preserving the relative phase. After the delay, the two pulses are recombined (step 7) and directed to the polarization analyzer.
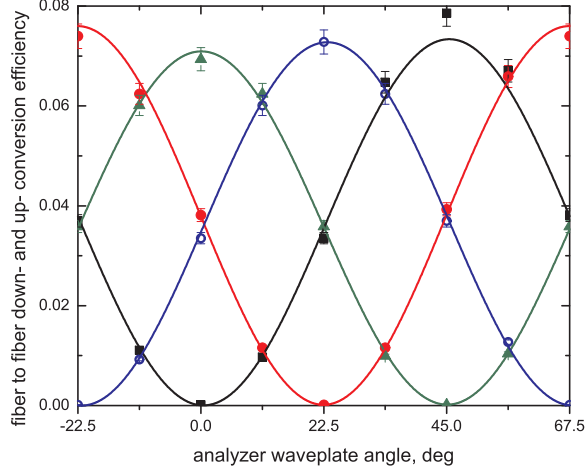
Figure 18: Performance of the polarization-independent wavelength converter. The polarization of the field after the down- and up-conversion sequence is measured for an input light field linearly polarized at 0° (black squares), 22.5° (red solid circles), 45° (green triangles), 67.5° (blue open circles). Solid lines - corresponding fits of the form $\eta(1/2 + V\sin(\frac{\phi-\phi_0}{4}))$ with the following parameters: efficiency, η :7.3(1)%, 7.6(1)%, 7.1(1)%, 7.3(1)%, visibility, V: 0.999(2), 0.996(3), 0.99(2), 1.00(3), and phase shifts ϕ_0: 45.5(1)°, 67.4(1)°, 0.1(2)°, 23.2(1)°, correspondingly. The goodness of the fits, $\chi^2 < 3$, $R^2 > 0.998$

The performance of the converter is quantified for four input light fields, polarized at $0°, 45°, 90°, 135°$ angles. The polarization of the field after the down- and up-conversion sequence is then measured (Fig. 18). The input polarization angle is preserved within 0.5°, and the contrast of more than 100:1 ensures that the linearity of the input polarization is maintained. Since an arbitrary polarization can be decomposed in this basis, this demonstrates polarization-independent frequency conversion that is sufficiently accurate for maintaining polarization entanglement, as described in the following chapter.

In conclusion, a wavelength conversion between 795 nm and 1367 nm is demonstrated. The low noise and high-efficiency wavelength conversion for an arbitrary polarization state can be utilized for interfacing the long-lived atomic quantum memories with the existing network of optical fibers with minimized losses in the 1.3-1.5 μm range. Experimental observations of the quantum correlations and the polarization entanglement of the telecom field with a remotely stored atomic excitation are described in the following chapter.

CHAPTER IV

A TELECOM INTERFACE FOR LONG-LIVED QUANTUM MEMORIES

This chapter is based on Ref. [32, 64].

Quantum memories based on cold atoms trapped in differential-light-shift-free optical lattices demonstrate both high read-out efficiencies and long lifetimes [32, 33, 64]. However, the matter excitation is coupled to the near-infrared (0.8 - 0.85 μm) transitions from ground states that are outside the transparency window (1.3 - 1.5 μm) of the telecom fibers (Fig.3). The wavelength conversion, described in the previous chapter, is ideally suited for interfacing the long-lived quantum memories with the existing network of telecom fibers. In this chapter experimental realizations of the telecom compatible long-lived quantum memories are presented, demonstrating quantum correlations and entanglement between telecom fields and stored matter excitations.

4.1 Quantum correlations of telecom light with quantum memory

Once the wavelength conversion between the quantum memory 795 nm and telecom 1367 nm wavelengths has been tested with coherent light, showing high efficiency and low noise, it can be utilized for the quantum memory signal field. The experimental setup is shown in Fig. 19. This describes single photon generation, storage, and retrieval based on the Duan-Lukin-Cirac-Zoller protocol (Fig.19a), with the wavelength conversion interface in which signal photons are down converted and transmitted in the telecom wavelength regime (Fig.19b).

To explicitly confirm that the telecom signal field and the long-lived spin waves
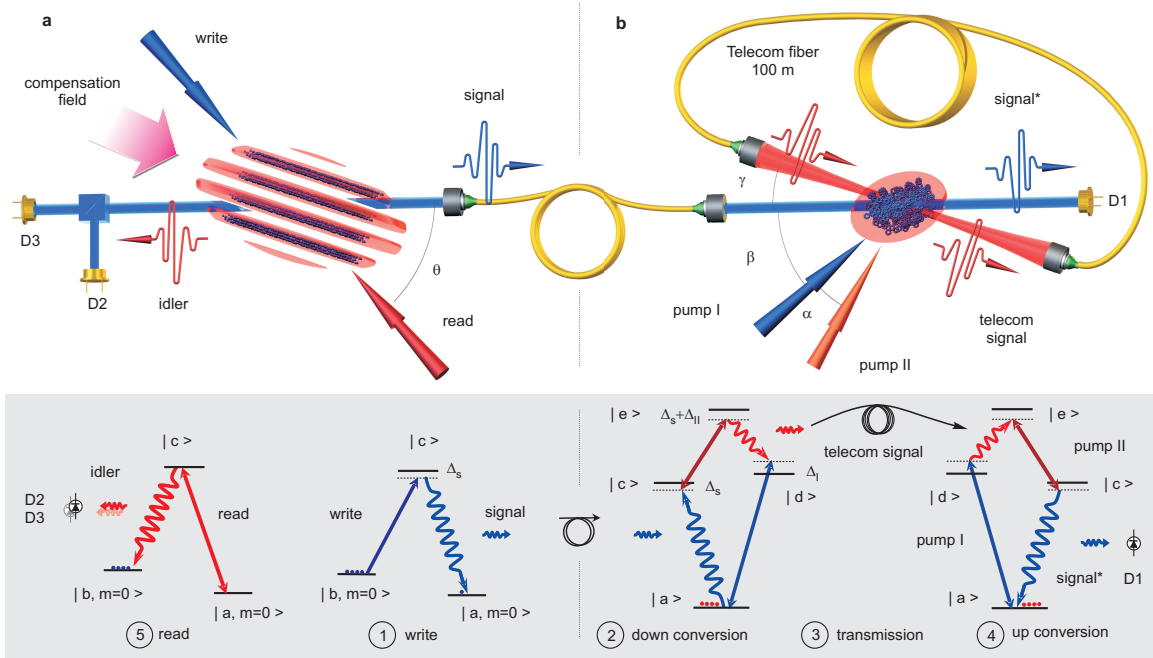
Figure 19: Essential elements of the atomic quantum memory with telecom photon interface. a) Long-lived quantum memory based on the first-order magnetically insensitive hyperfine coherences in sub-Doppler cooled ^{87}Rb atoms, confined in a 6 μm period 1D lattice with compensated differential Stark-shift. The temporal sequence of our protocol is labeled by steps 1-5. A weak write laser pulse, red detuned from the $b \leftrightarrow c$ transition, generates pairs of atomic spin wave excitations and write signal field photons by Raman scattering, step 1. The write signal field is directed, via optical fiber, onto a single photon detector (not shown) and a detection event heralds the presence of an atomic excitation in the lattice. Alternatively, the signal is directed into a frequency conversion setup, as shown in part b. Signal detection at D1 initiates a controlled storage period after which a read laser pulse, resonant to the $a \leftrightarrow c$ transition converts the stored spin-wave into an idler field by backward Raman scattering. The idler is directed to a beam splitter, step 5, followed by detectors D2 and D3, where photoelectric correlations are determined from the record of detection events. The gaussian spot size of the signal/idler mode is 110 μm. b) Successive frequency down- and up- conversion is realized by four-wave mixing. Four-wave mixing occurs between strong pump I (4.3 mW) and pump II (13 mW) fields and single-photon level ($\sim$20 aW) write signal and telecom signal fields of substantially different wavelengths (780, 1324, 795 and 1367 nm). In step 2, the write signal and pump fields generate the telecom signal ($e \rightarrow d$ transition). In step 3, the telecom signal is directed through a 100 m standard telecommunication fiber back to the atomic sample. In step 4, the telecom signal is up-converted to near-infrared light (signal*, $a \leftrightarrow c$ transition), which is detected with high efficiency by the Si single photon detector, D1. This detection event heralds the presence of a spin-wave atomic excitation in the lattice.
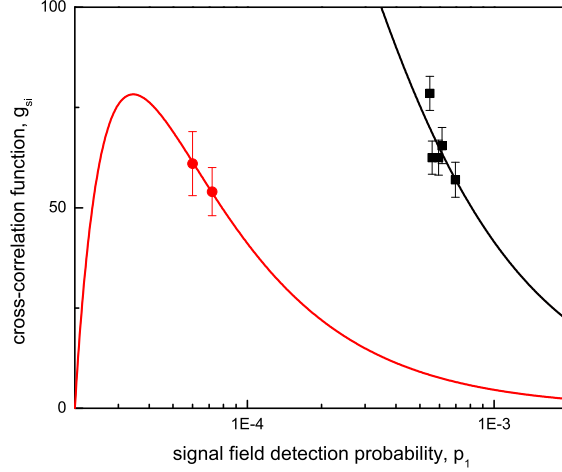
Figure 20: Normalized intensity cross-correlation function values for the original signal field (black squares) and the signal field down-converted to telecom wavelength and up-converted back for detection (red circles). Solid lines are theoretical values based on the measured losses and background levels according to formula (12).

cannot be described classically, joint photoelectric detection measurements on the signal and retrieved idler fields are performed. Specifically, the second-order intensity cross-correlation function g_{si} [65] and the α-parameter of Grangier *et al.* [66], determined from the photoelectric detection event probabilities at detectors D1-3, are measured. The protocol involves a sequence of trials, with each trial beginning with a write pulse and terminating with a clean pulse that resets the atomic state until the signal detector, D1, registers a photoelectric detection event. At that point, the sequence is terminated, and the prepared spin wave is stored for the time T_s, after which a read pulse converts the excitation into an idler field that is directed onto a beamsplitter followed by photodetectors D2 and D3.

The second-order intensity cross-correlation function is measured as the following combination of joint detection probabilities:

$$g_{si} = \frac{p_{12} + p_{13}}{p_1(p_2 + p_3)}. \tag{11}$$

With the given transmission and detection probabilities of the signal/idler fields (t_1,

$t_{2|3} = t_2 = t_3$), and the dark count probabilities of the detectors $B_i, i = 1, 2, 3$, the maximum value of g_{si} can be calculated as:

$$g_{si} = \frac{t_1}{p_1(1 + \frac{(B_2+B_3)t_1}{t_{2|3}(p_1-B_1)})}. \tag{12}$$

Fig. 20 demonstrates the values of g_{si}, measured for the original 795 nm and down-converted 1367 nm signals. The wavelength conversion preserves the value of the intensity correlations and decreases p_1 by the total down- and up-conversion loss factor of 10. It is consistent with formula (12) and the total transmission of the 795 nm signal from the input of the signal mode fiber to detector D1 of 0.1, a product of 0.82×0.82 (two fiber coupling efficiencies, one each for the 795 nm and 1367 nm fields) $\times 0.52 \times 0.52$ (down- and up-conversion efficiencies) $\times 0.55$ (transmission coefficient, mostly due to losses on the uncoated glass vacuum cell and optical filters).

The measured retrieval efficiency η refers to photoelectric detection probabilities per read pulse, determined by the sum of probabilities $p_2 + p_3$ to detect photoelectric events at D2 and D3, respectively. The measured passive losses from the atomic sample to the detector in the idler channel produce an efficiency factor of $0.25 \pm 10\%$. *Intrinsic* efficiencies η_{int} and ϵ_{int} are therefore greater than η and ϵ by a factor of 4, respectively, as shown in Table 5. The uncertainties given are based on the statistics of photoelectron counting events. All the measured idler efficiencies are verified to be independent of p_1, so that they have negligible background contributions.

The anticorrelation parameter α is given by the ratio of various one-, two- and three-fold photoelectric detection probabilities measured by the set of detectors D1,D2, and D3 [66]:

$$\alpha = \frac{p_1 p_{123}}{p_{12} p_{13}}.$$

The signal field is detected at D1, while the idler field is incident on a beamsplitter followed by photodetectors D2 and D3. α is determined from the measured set of joint photoelectric detection probabilities on the three detectors, D1-3, (Fig. 17). The value

$\alpha = 1$ delineates regimes of classical (uncorrelated) ($\alpha \geq 1$) and quantum ($0 \leq \alpha < 1$) electromagnetic fields. The limiting case, $\alpha = 0$, implies perfect pairwise signal field-memory correlations, such as the weakly excited two-mode squeezed vacuum state [67], or the single-photon state of the idler field conditioned upon a detection event at D1.

The results after storage periods of 60 and 100 ms without wavelength conversion are shown in Table 5a, along with the corresponding measured and intrinsic (normalized by optical losses) retrieval efficiencies. The measurement of the α-parameter after an 11 ms storage period with the telecom signal field is presented in Table 5b. The measurement is achieved by converting the telecom signal field into a near-infrared field via the second pass in the EDMOT and followed by detection at D1. The duration of data acquisition was 138 hours. The measured efficiency of wavelength conversion for the signal field is consistent with the value η^{max} determined with the coherent laser field, as explained in the caption of Fig. 16. Given the measured single and double coincidence detection rates, the classical threshold for triple coincidences was ≈ 4 events, whereas a zero value is observed. That detection of classical fields with the protocol is verified to give $\alpha = 0.96 \pm 0.06$, consistent with the expected value of unity. This shows that, enabled by the high frequency conversion efficiency and negligible noise, nonclassical memory-signal behavior is maintained throughout the two sequential frequency conversion steps.

The approach demonstrated here is a step towards entanglement distribution over thousands of kilometers. By using widely separated elements of this type, telecom wavelength light could be generated by phase-coherent write processes, with conversion and interfered on beam-splitters at intermediate locations, extending the scale of the network to previously unattainable distances. As a next step, an entanglement of a photonic telecom polarization qubit and a long-lived spin-wave is demonstrated, which is described in the next section.

Table 5: (a) Measured values of α (see text), measured efficiency η, and intrinsic efficiency η_{int}; (b) Measured value of α, measured efficiency η, and intrinsic efficiency η_{int} when the 795 nm signal field is first converted to telecom wavelength, passed through a 100 m telecom fiber, and converted back to a 795 nm field. Error bars represent ± 1 standard deviation based on photoelectron counting statistics, calculated from the mean values divided by the square root of the number of triple coincidences measured with detectors D1, D2 and D3.

	T, ms	α	η	η_{int}
(a)	60	0.00 ± 0.07	1.9%	7%
	100	0.18 ± 0.12	1.2%	5%
(b)	11	0.00 ± 0.27	1.9%	7%

4.2 Telecom field entangled with Matter

Entanglement distribution is one of the ultimate goals of quantum telecommunication. In addition to quantum key distribution opportunities, it provides a way of verifying the axiomatics of quantum physics theory questioned by the Einstein-Podolsky-Rosen (EPR) paradox [20]. While the entanglement phenomenon is now routinely demonstrated, an experiment with the simultaneously closed detection and locality loopholes [21] has not been performed yet. In order to remove the locality loophole, the entanglement has to be distributed over a distance that is longer than classical information can propagate. The detection loophole occurs if the state detection efficiency is not sufficiently high. It is challenging to satisfy both of these conditions simultaneously. Entanglement distribution via a telecom fiber is a step towards the genuine resolution of the EPR paradox .

Here a measurement of entanglement between an atomic spin-wave memory qubit and a telecom field qubit, at a storage time of 10 ms is demonstrated. The high-efficiency and low-noise wavelength conversion between NIR and telecom fields in an optically-thick, cold Rb gas, as described in the Chapter 3, is at the core of the experimental protocol. The memory qubit employs two spatially distinct spin-waves,
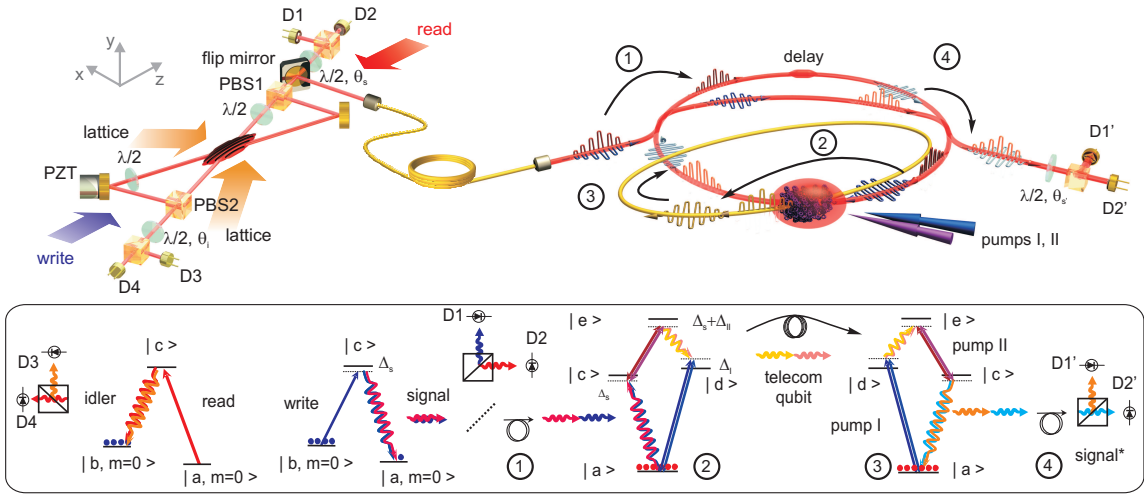
Figure 21: Left side: A write laser (270 μm mode waist) generates spin-waves in atomic ^{87}Rb, confined in a 1-D lattice with magnetically-compensated clock transition light shifts. Trap depth $U_0 = 56$ μK, trap frequencies $(\omega_x/(2\pi), \omega_y/(2\pi), \omega_z/(2\pi)) = (8100, 116, 10)$ Hz. The experimental protocol is based on a sequence of write/clean pulses, terminated by photodetection of the signal field at D1 or D2 [1, 2]. After a storage period, the stored spin-wave qubit is converted by the read laser to an idler field qubit and a polarization measurement of the latter is performed. Signal and idler fields intersect at the center of the trap at an angle of $\pm$ 0.9° with respect to the z-axis, and have a waist size of 120 μm. Two signal (idler) paths are overlapped on PBS1 (PBS2). The interferometric path length difference is stabilized so that the signal-idler polarization state at the output of PBS1 and PBS2 has the form $\propto (|H\rangle_s|H\rangle_i + |V\rangle_s|V\rangle_i)$. An auxiliary laser at 766 nm (not shown), intensity-stabilized and frequency-locked to the potassium D_2 line, is used for that purpose. Right side: Successive frequency down- and up- conversion of the signal field qubit is realized by four-wave mixing in cold ^{87}Rb. A polarizing beamsplitter separates the H- and V- components of the signal field and the latter is delayed by an optical fiber (step 1). In step 2, the write signal and pump fields generate the telecom signal ($e \rightarrow d$ transition), which is directed through a 100 m standard telecommunication fiber back to the atomic sample. In step 3 the telecom signal is up-converted to a NIR signal ($a \leftrightarrow c$ transition). After its two polarization components are temporally overlapped (step 4) using the same interferometric arrangement used to separate the incoming NIR signal, a polarization measurement is performed. High-efficiency detection is achieved by the Si single photon detectors, D1′ and D2′. The inset shows the Λ-type atomic levels used for the DLCZ scheme (left) and the cascade configurations used for wavelength conversion (right). Parameters: $|a\rangle = |5S_{1/2}\ F = 1\rangle$, $|b\rangle = |5S_{1/2}\ F = 2\rangle$, $|c\rangle = |5P_{1/2}\ F = 2\rangle$, $|d\rangle = |5P_{3/2}\ F = 2\rangle$, $|e\rangle = |6S_{1/2}\ F = 1\rangle$, $\Delta_s = -2\pi \times 17$ MHz, $\Delta_I = 2\pi \times 41$ MHz, $\Delta_{II} = 2\pi \times 6$ MHz.

both based on the $m = 0 \leftrightarrow 0$ clock transition between hyperfine ground levels. The qubit spin-wave, pinned by an optical lattice to reduce motional dephasing, is lifetime-enhanced by mixing the clock states using a bias magnetic field to offset inhomogeneous, differential ac-Stark shifts [33, 68]. The Bell inequality violation measurements indicate that the memory qubit is entangled with the NIR qubit for as long as 0.1 s, a 30-fold improvement on the results of Ref. [31].

The differential-light-shift-compensated memory qubit is shown in the left panel of Fig. 21. A magneto-optical trap (MOT) captures ^{87}Rb atoms from a background vapor. After compression and cooling the atoms are transferred to a one dimensional optical lattice formed by interfering two circularly polarized 1064 nm beams intersecting at an angle of 9.6° in the horizontal plane (a 6.3 μm lattice period). The waists of the lattice beams are ≈ 0.2 mm and their total power is typically 12 W. The cigar shaped atomic cloud has $1/e^2$ waists of 0.15 mm and 1 mm, respectively, and contains about 10^7 atoms. After loading, the atoms are prepared in the $|+\rangle \equiv |5^2S_{1/2}, F = 2, m = 0\rangle$ state by means of optical pumping. The magnetic field is set to the "magic" value (4.2 G for our 1064 nm wavelength lattice [33]) to equalize the ac-Stark shifts of the clock states.

Raman scattering of a weak linearly polarized write laser field transfers a fraction of the atomic population into the $|-\rangle \equiv |5^2S_{1/2}, F = 1, m = 0\rangle$ clock state generating a signal field offset in frequency from the write field by the ^{87}Rb ground-level hyperfine splitting of 6.8 GHz. The memory qubit is based on two spatially distinct spin-waves [16, 69]. The interferometric arrangement for the associated signal and idler field modes is shown in Fig. 21. Two Gaussian modes of the signal field centered at angles $\pm 0.9°$ to the write field wave-vector $\mathbf{k_w}$ direction are combined on a polarizing beamsplitter (PBS1), and directed to either the polarization measurement setup involving detectors D1 and D2 for spin-wave memory/NIR field entanglement

analysis, or, via an optical fiber, to the wavelength conversion setup to generate memory/telecom field entanglement. The signal field photoelectric detection probability per experimental trial is in the range $10^{-4} - 10^{-3}$ and can be varied by adjusting the write field power/detuning.

The detection of the signal photon implies a momentum change $\hbar(\mathbf{k_w} - \mathbf{k_s})$ of the atoms, where $\mathbf{k_s}$ is the signal field wavevector. An atom at position $\mathbf{r}_\mu$ contributes to the spin-wave excitation with a phase factor $e^{-i(\mathbf{k_w}-\mathbf{k_s})\cdot\mathbf{r}_\mu}$; the atom experiences additional phase modulation due to the local value of the differential ac-Stark shift. The collective atomic excitation, imprinted with this phase grating, is the *write* spin wave. The spin wave coherence is essential for efficient coupling to a single spatial electromagnetic field mode in the memory retrieval stage.

The retrieval, or read process, is performed after a defined storage period. A read field pulse converts the stored spin-wave excitations into an idler field by Raman scattering, Fig. 1. The idler emission is collected in the two Gaussian spatial modes of the detected signal field, but with opposite propagation directions ($\mathbf{k_i} \approx -\mathbf{k_s}$). The two idler modes are combined on a polarization beamsplitter (PBS2) and directed to detectors D3 and D4 for polarization analysis.

In the arrangement shown in Fig. 21, the vectors $\mathbf{k_w} - \mathbf{k_{s_j}}$ for each of the two qubit spin-waves, $j = 1, 2$, are at angles $\phi \approx \pm 0.5°$ to the lattice axis (x-axis). The efficiency of light storage and retrieval is measured as a function of storage time to characterize the coherence properties of the two spin waves. Storage of a classical field is achieved by counter propagating the light in the signal field fiber, while the read light is used in the role of a control field. In this geometry the stored spin waves are of the same 50 μm period and have a similar spatial envelope as the single excitations created via the DLCZ protocol. The spin-wave period is much longer than that of the lattice, resulting in a strong suppression of motional dephasing.

The polarization states of both the signal and idler fields are measured using a

polarizing beam splitter and two single photon detectors, D1, D2 for the signal and D3, D4 for the idler (additional technical details are given in Ref. [31]). The joint signal-idler detection rates between detector Dn, $n = 1, 2$ and detector Dm, $m = 3, 4$ are denoted by $C_{nm}(\theta_s, \theta_i)$. Here θ_s and θ_i are the angles through which the polarization is rotated by the respective half-waveplates. The rates $C_{ij}(\theta_s, \theta_i)$, $i = 1, 2, j = 3, 4$ exhibit sinusoidal variations as a function of the waveplates' orientations. In order to account for the unequal efficiencies of the detectors (D1, D2) and (D3,D4), each correlation measurement includes flipping the polarization of both signal and idler fields by $\pi/2$ within the data set. The Bell's inequality violation $|S| \leq 2$ is checked by measuring polarization correlations between signal and idler fields at certain canonical angles, where $S = E(\pi/4, \pi/8) + E(0, \pi/8) + E(0, -\pi/8) - E(\pi/4, -\pi/8)$; here the correlation function $E(\theta_s, \theta_i)$ is given by [54–56]

$$\frac{C_{13}(\theta_s, \theta_i) + C_{24}(\theta_s, \theta_i) - C_{14}(\theta_s, \theta_i) - C_{23}(\theta_s, \theta_i)}{C_{13}(\theta_s, \theta_i) + C_{24}(\theta_s, \theta_i) + C_{14}(\theta_s, \theta_i) + C_{23}(\theta_s, \theta_i)}.$$

The measured sinusoidal variation of $E(\theta_s, \theta_i)$ as a function of θ_i for fixed θ_s is shown in Fig. 3. In Table 6 the values of E and the Bell parameter S are listed for two values of storage time: 1 ms and 0.1 s. The measured idler photodetection probabilities for the data in Table 6 are 1.7% at 0.1 s and 4% at 1 ms. Normalized by the passive transmission and detection losses (0.25), the intrinsic atomic excitation retrieval efficiency after 0.1 s storage is 7% (16% at 1 ms).

To convert the signal photons produced by the write process into telecom wavelength light non-degenerate non-collinear four-wave mixing, described in the Chapter 3, is utilized. A cigar-shaped ($\varnothing \sim 2$ mm, L ~ 6 mm) sample of ^{87}Rb gas is prepared, in level $|a\rangle$ with an optical depth of ~ 150, in an extended dark magneto-optical trap (EDMOT).

The polarization-stable wavelength conversion is achieved by splitting the two polarization components of the optical field and delaying the (vertically polarized) V-component by 235 ns (Fig. 17). By switching the polarization of both pump

(a)   (b)
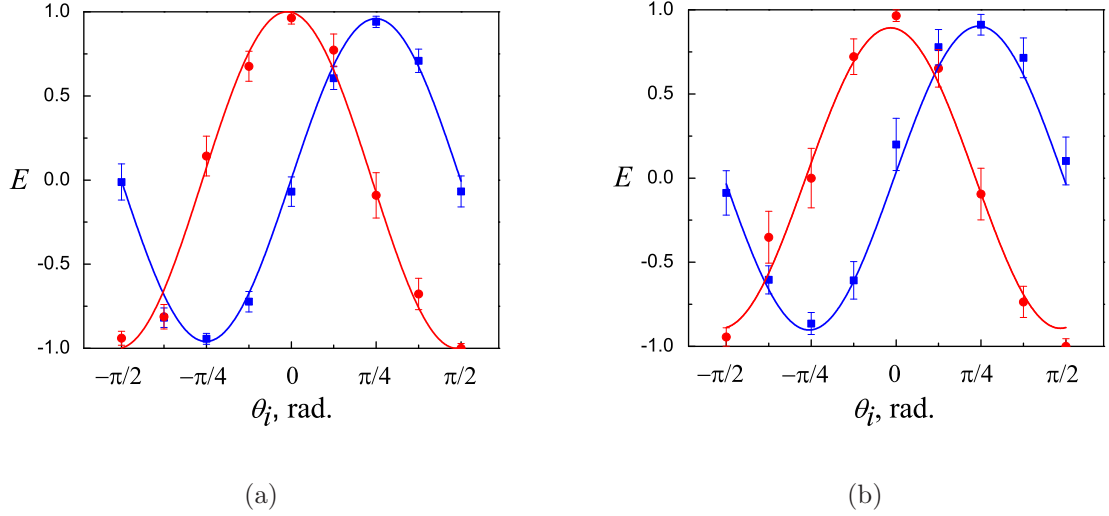
Figure 22: Measured values of the correlation function $E(\theta_s, \theta_i)$ as a function of θ_i for 1 ms storage. Circles are representation of $\theta_s = 0$, squares are for $\theta_s = \pi/4$. The curves are sinusoidal fits to the data. (b) Measured correlation function $E(\theta_s, \theta_i)$ when the 795 nm signal field is first converted to telecom wavelength, passed through 100 m of telecom fiber, and converted back to a 795 nm field, for 1 μs storage. Circles are for $\theta_s = 0$, squares are for $\theta_s = \pi/4$. The curves are sinusoidal fits to the data.

fields to orthogonal settings while the V-component interacts with the atoms, high transparency and high (54%) conversion efficiency for both (horizontally polarized) H- and V- components is achieved. The conversion efficiency is lower than the 65% observed for a single polarization component as a result of the limited power available for pump II and the denser atomic sample used to compensate for the undesirable effects of hyperfine optical pumping.

Table 6: Measured correlation function $E(\theta_s, \theta_i)$ and S for 1 ms and 100 ms storage times. These are based on 582 events and 1001 events, respectively.

		$E(\theta_s, \theta_i)$	
θ_s	θ_i	1 ms	0.1 s
$\pi/4$	$-\pi/8$	-0.78 ± 0.05	-0.65 ± 0.05
$\pi/4$	$\pi/8$	0.71 ± 0.07	0.67 ± 0.05
0	$-\pi/8$	0.75 ± 0.05	0.66 ± 0.05
0	$\pi/8$	0.66 ± 0.06	0.68 ± 0.05
		$S = 2.90 \pm 0.12$	$S = 2.66 \pm 0.09$

Table 7: Measured correlation function $E(\theta_s, \theta_i)$ and S when the 795 nm signal field is first converted to telecom wavelength, passed through 100 m telecom fiber, and converted back to a 795 nm field. Storage times are 1 μs and 10 ms, based on 986 and 667 events, respectively.

		$E(\theta_s, \theta_i)$	
θ_s	θ_i	1 μs	10 ms
$\pi/4$	$-\pi/8$	-0.54 ± 0.05	-0.61 ± 0.06
$\pi/4$	$\pi/8$	0.65 ± 0.05	0.72 ± 0.06
0	$-\pi/8$	0.78 ± 0.04	0.75 ± 0.05
0	$\pi/8$	0.58 ± 0.05	0.56 ± 0.07
		$S = 2.55 \pm 0.10$	$S = 2.64 \pm 0.12$

The level of dark counts for commercially available InGaAs/InP telecom wavelengths single photon detectors is too high for our purposes. Instead, a reverse wavelength conversion sequence, from 1367 nm to 795 nm is employed, Fig. 17. The H- and V- components of the regenerated NIR signal field are subsequently recombined. A half-wave plate, a polarizing beam splitter and two Si single photon detectors D1' and D2' complete the measurement of the polarization state of the telecom signal field qubit. The combined transmission measured for the NIR signal qubit from the input of the signal field fiber to detectors D1' and D2' is 7.5(5)%, with a factor 0.25 contribution from passive optical elements and fiber coupling losses (0.8 for both telecom and NIR fields). The interferometric configuration for the signal field that is sketched in the right panel of Fig. 17 is designed to cancel out phase fluctuations occurring on a time scale slower than 1 μs, so that active stabilization of the interferometer is not required. The ellipticity of the signal field, acquired due to the birefringence of the optical fibers, is removed by adjusting the phase difference between the H- and V- components of the pump II pulses employed for the up-conversion, as described in Chapter 3. With coherent light input the polarization state is preserved after transmission and conversion with a power contrast of greater than 100 to 1. A drift of the polarization fringes on a timescale of two days was negligible, for either coherent laser or signal field inputs to the wavelength conversion set-up.

The measured sinusoidal variation of $E(\theta_s, \theta_i)$ as a function of θ_i for fixed θ_s is shown in Fig. 22, for a short period of 1 μs. In Table 7 we give the measured values of E and the Bell parameter S for 1 μs and for 10 ms storage; longer storage times were not employed due to the prohibitively long data acquisition time required. The measured idler photodetection probabilities for the data in Table 7 are 5% at 1 μs and 2.8% at 10 ms. The data was taken with larger lattice beams (0.26 mm waist sizes instead of 0.2 mm for the data without wavelength conversion) resulting in a revival behavior of the retrieval efficiency in the 30-100 ms region; we attribute this to atomic motion along the long axis of the trap.

In summary, preservation of memory/light entanglement through two stages of telecom wavelength conversion, for 10 ms storage, is confirmed by measuring the Bell parameter of 2.64(12), more than 5 sigma above the classical threshold.

In conclusion to this chapter, the telecom interface based on the four-wave mixing process in a cold atomic gas maintains the quantum state of the input light, which is demonstrated by measuring the second order intensity correlation, the alpha parameter, and polarization entanglement with matter. As the intrinsic down- and up-conversion efficiencies are already close to unity, further improvements are mainly of engineering character. With higher power laser systems, anti-reflection coatings, and better optical elements the wavelength converter can reach ideal conversion efficiency. Combined with second scale quantum memories [70], this system exhausts the benefits of the probabilistic quantum telecommunication protocols based on cold atoms in magneto-optical and dipole traps. In the following chapters, a substantially different system using triply charged ions of Thorium-229 is described. Thorium-229's uniquely optically accessible nuclear states may provide a better paradigm for long-distance quantum telecommunication and metrology.

CHAPTER V

LASER COOLED THORIUM-229

This chapter is partially based on Ref. [7, 71].

Thorium-229 is a unique nucleus due to its isomer nuclear transition with ~ 8 eV [39] energy, which is remarkably low when compared to the typical keV and MeV nuclear energy scales. The corresponding nuclear levels promise hour-scale coherence times, which can be utilized for clocks or long-lived quantum memories. Additionally, the nuclear transition is likely to be highly sensitive to variations of fundamental constants. Producing laser-cooled Thorium-229 for the first time is presented in this chapter. The laser cooled ^{229}Th^{3+} ion is a promising system to identify the energy of the isomer state and to utilize the extraordinary properties of this nuclear transition. In Section 1, relevant properties of Thorium-229 and its triply charged state are presented. Sections 2 and 3 contain detailed information about the experimental apparatus and techniques for obtaining laser-cooled ^{229}Th^{3+} ions.

5.1 Thorium properties

5.1.1 Nuclear properties

Thorium is an actinoid with the atomic number 90. Among its 27 isotopes, the most stable are ^{228}Th, ^{229}Th, ^{230}Th, ^{232}Th. Thorium-232 is the only primordial isotope with a half-life time of 14.05 billion years and a specific radioactivity of 4.07 kBq/g. The half-life time of Thorium-229 is significantly shorter (7340 years), and the specific radioactivity is higher (7.34 GBq/g). The natural abundance of Thorium-229 is zero; however, it is produced during the alpha decay of Uranium-233 in nuclear reactors and can therefore can be obtained at a price of about one hundred thousand dollars per milligram. While Thorium-229 is the alpha-emitter, the decay chain
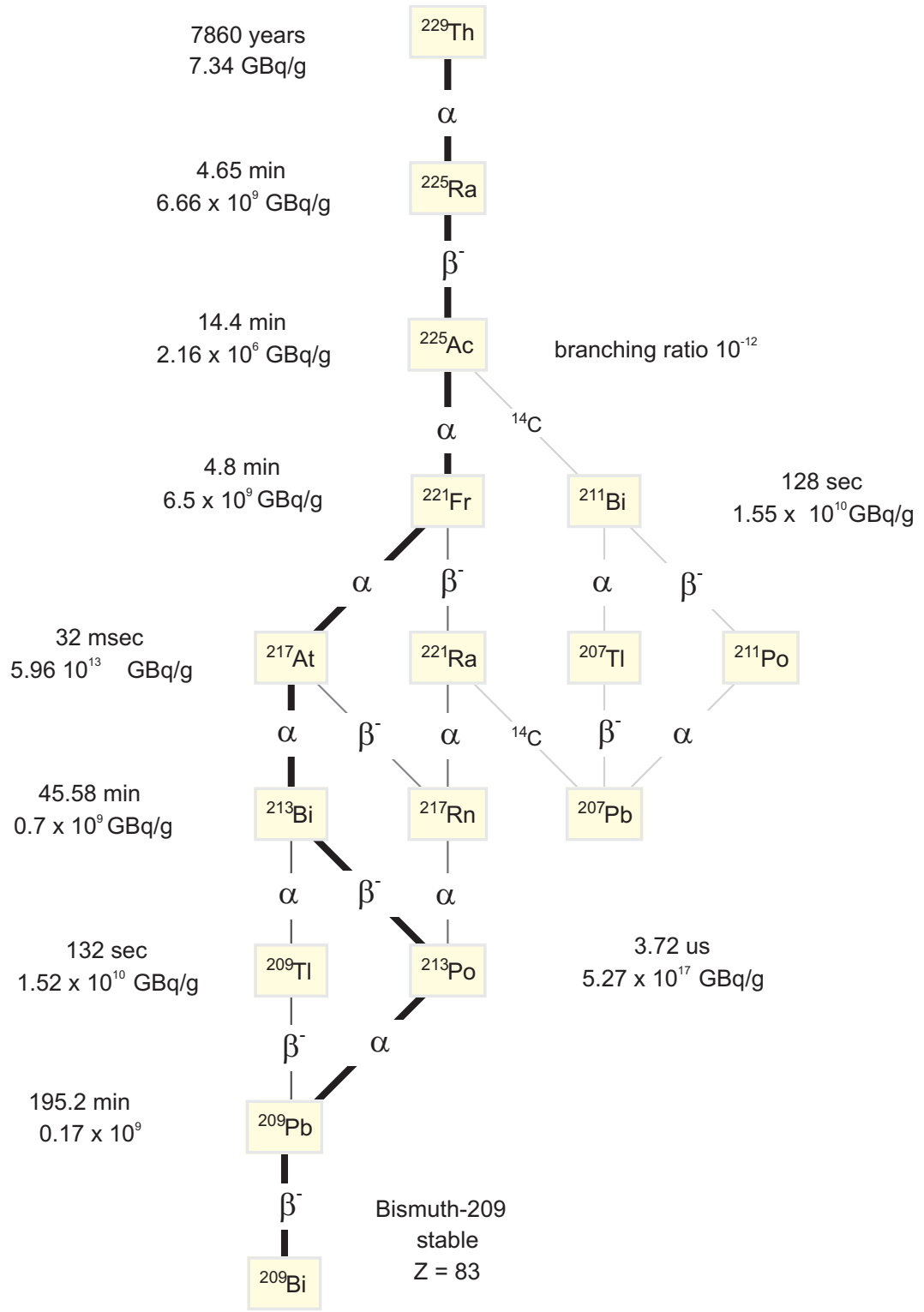
Figure 23: Lifetimes and radioactivity in gigabecquerel per gram for Thorium-229 and its decay products.

.

(Fig.23) products create significant amounts of beta and gamma radiation that are detectable through a stainless steel vacuum chamber. It was observed that ejected decay products contaminate distant parts of the vacuum chamber and become primarily the beta radiation sources. Radiation safety is the foremost concern during assembly and disassembly of vacuum chambers with Thorium-229 samples; strict rules of radiation safety must be followed during operations with open sources of Thorium-229. Once the Thorium-229 is sealed in a vacuum chamber, the stainless steel walls provide sufficient shielding for a safe work environment. With 40 μg of Thorium-229 nitrate salt in our vacuum chamber, the Geiger counter reads $\sim$ 200 counts per minute at $\sim$ 2 inches away from the sample. Since the average human working distance is substantially greater than that of two inches, the annual dose of radiation is well below the natural background of 300 mrem.

The nuclear and atomic experiments combined with theoretical calculations revealed many of the nuclear properties. Of relevance to this work are the radius of the Thorium-229 nucleus, $r_{rms} = 5.6807 \pm 0.0509$ fm [72], the difference in mean-square radius from the 232 isotope to the 229 isotope, $\delta\langle r^2 \rangle = \langle r^2 \rangle_{229} - \langle r^2 \rangle_{232} = -0.334(45)$ fm^2 [72], spectroscopic nuclear electric quadrupole moment of the ground state, $Q = 3.149(32)$ eb [73], spectroscopic nuclear magnetic dipole moment of the ground state, $\mu = 0.45(4)\mu_N$ [74], Coulomb energy $V_C = 967$ MeV [49], and the energy of the nuclear isomer state of 7.6(5) eV [39], with a recent revision to 7.8(5)eV [75]

5.1.2 Atomic properties

A neutral Thorium atom has four valence electrons that are responsible for the complex electronic structure of neutral Th atoms and Th$^+$, Th^{2+} ions. Neutral Thorium spectroscopy was done with inline laser ionization [76], and laser two-photon spectroscopy of trapped ^{232}Th$^+$ was performed in the environment of a quenching buffer gas at pressures of $\sim 10^{-3}$ Torr [77]. However, the abundance of metastable states

complicates further study and manipulation of these multivalent atoms. The monovalent nature and consequent low number of metastable states make triply charged Thorium atoms favorable for precision spectroscopy and manipulation.

Thorium triply charged ions, and the Thorium-229 isotope in particular, have not been extensively studied prior to this work. Only three electronic transitions in ^{232}Th^{3+} were measured with laser spectroscopy [52] and none in the Thorium-229 isotope. Limited information about its energy structure is available from the discharge spectroscopy of the pre-laser era, first performed in 1936 by R. J. Lang [78]. Further experimentations were conducted by P. F. A. Klinkenberg and R. J. Lang in 1949 [79], G.W. Charles in 1958 [80], B.A. Palmer and R. Engleman, Jr. in 1983 [81]. Findings to date were analyzed and summarized in 1988 by P. F. A. Klinkenberg [82]. Measurements of the energy levels feature systematic shifts of up to 10 GHz, and only a few manifolds of the excited states are mapped (Fig.24).

The atomic structure theory for thorium has recently been developed by several groups. The level energies, the dipole moments, and the lifetimes of Th^{3+} were calculated by U. I. Safronova et. al. [83]. The energies follow the experimental data [82] accuracies of ~ 10 GHz. The hyperfine electric quadrupole B coefficients and isotope shifts of several Th^{3+} electronic levels, with respect to the nuclear quadrupole moment and the nuclear radii changes, have been calculated by J. C. Berengut et. al. [49].

It is remarkable that the electronic transitions from the ground state lie in the near-infrared and visible range, rather than the deep ultra-violet as it might be expected for ions with high charge numbers. This is an example of the so-called "Coulomb crossing," a result of the competition between Coulomb interaction and the electron shielding effect [84]. In neutral atoms, electrons with larger angular momenta L can have energies significantly higher than the electrons with smaller momenta but larger principal quantum number n due to the electron shielding effect. For example,
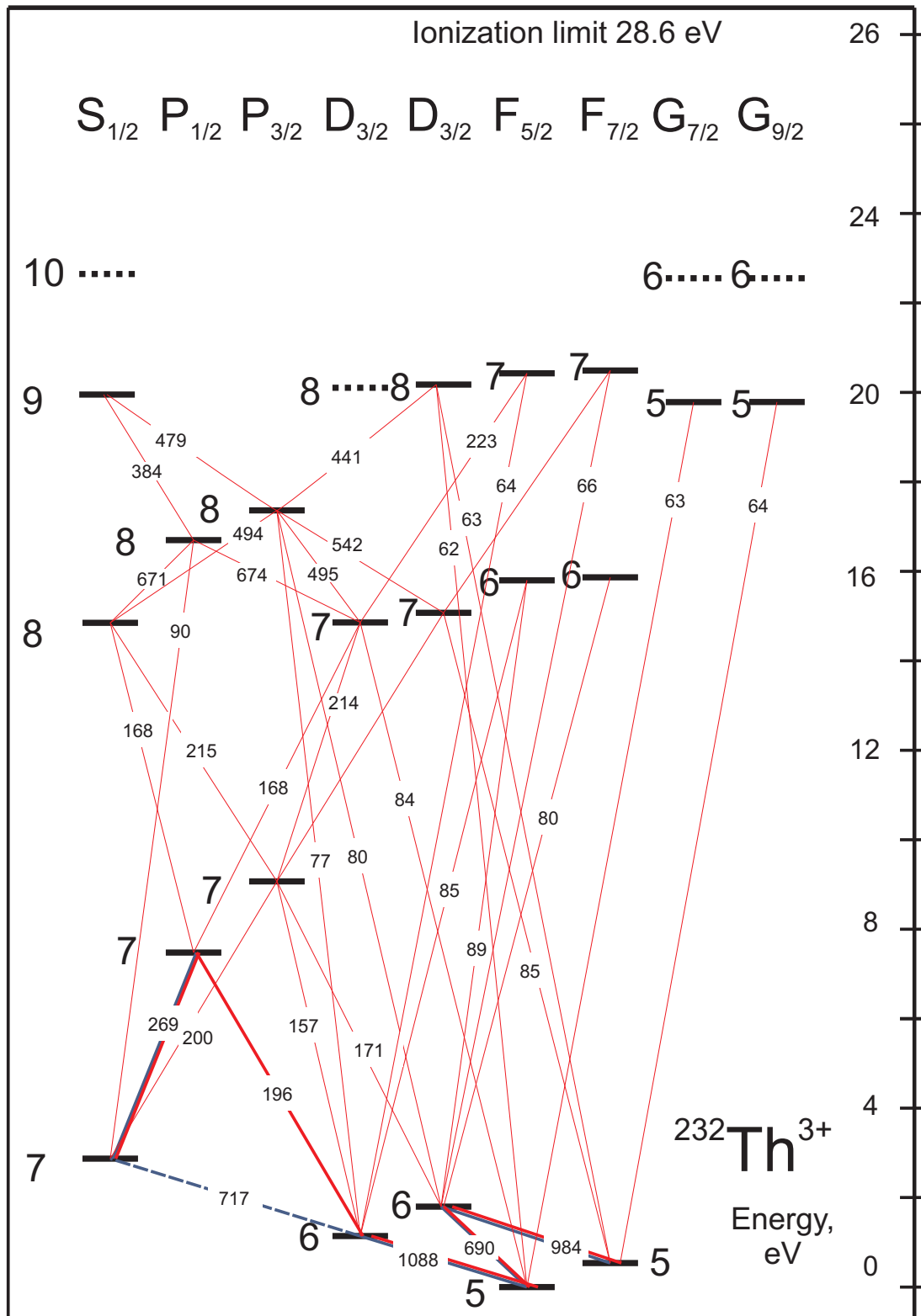
Figure 24: Grotrian diagram of $^{232}\text{Th}^{3+}$ ion. Red lines were observed with a discharge fluorescence, blue lines were laser excited.

.
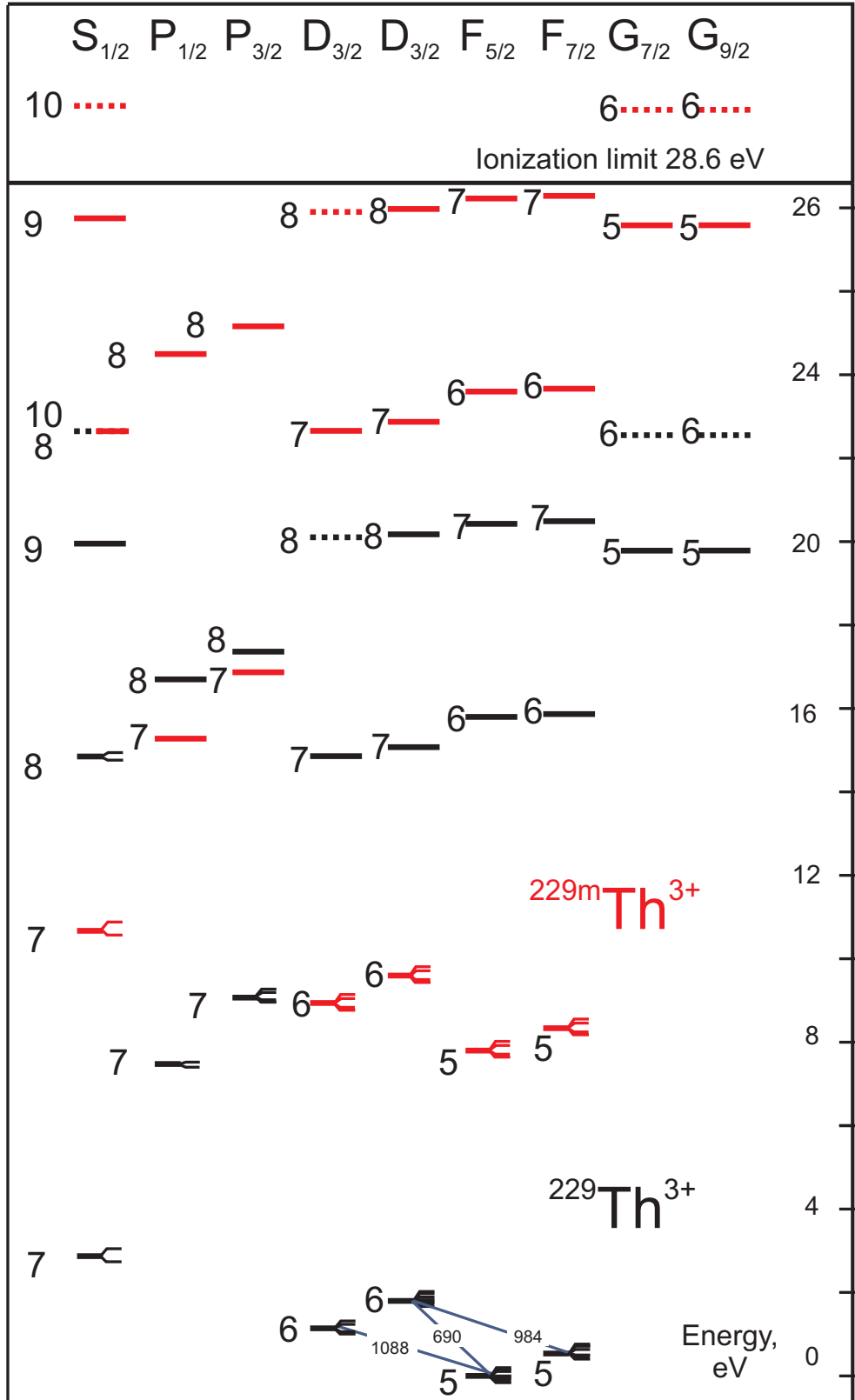
Figure 25: Grotrian diagram of ^{229}Th^{3+} ion. Blue lines correspond to laser excited transitions.

consider that a neutral Thorium atom the $5F$ orbital is above $7S$. At the other limit, when all the electrons except one are taken away, the atom becomes hydrogen-like and the same n levels are nearly degenerate, regardless of angular momentum ($E_{5F} \approx E_{5S}$). At this limit, a higher principal quantum number n corresponds to a higher energy. Th^{3+} is in the intermediate cross-over regime, where the $5F, 6D, 7S$ levels are separated by energies corresponding to red (690 nm, 717 nm) and near-infrared (984 nm, 1088 nm) transitions.

This crossover regime brings the transitions to the convenient optical domain where diode lasers are available. However, due to the larger angular momenta, the overlap of $5F$,$6D$ wavefunctions is substantially smaller with respect to the typically used S-P transitions. The reduced overlay leads to smaller transition dipole moments and narrower linewidths of ~ 100 kHz , complicating fluorescence detection and the laser cooling of these ions.

5.1.3   A Thorium nuclear clock

In 2003, Peik and Tamm pointed out that many of the standard external field shifts in atomic clocks could be suppressed or avoided in a ^{229}Th^{3+} optical nuclear transition by utilizing the $|7S_{1/2}\rangle$ electronic level within both the nuclear ground and isomer manifolds [40]. This pioneering proposal illuminated a way toward a next generation clock; however, their system is still subject to two important ion-clock limitations: The proposed $m_F = 0 \leftrightarrow m_F = 0$ clock transition experiences a significant second-order differential Zeeman shift (~ 70 kHz/mT^2), while electric-quadrupole decay of both clock states limits the clock linewidth to ~ 1 Hz. These limitations can be avoided by utilizing $|5F_{5/2}, I_g = 5/2; F = 5, m_F = \pm 5\rangle \leftrightarrow |5F_{5/2}, I_m = 3/2; F = 4, m_F = \pm 4\rangle$ stretched states. This configuration allows the thorium nuclear transitions at 160(10) nm to form a primary frequency reference approaching 10^{-19} inaccuracy in a local frame [7].

Such high accuracy is possible for several reasons. First, the nuclear transitions are much less perturbed by the external electromagnetic fields because the nuclear magneton is $m_p/m_e \approx 1840$ smaller than the Bohr magneton for electrons. In addition, the external fields are typically shielded by the electron cloud, providing further suppression of the external perturbation to the nucleus. Thorium is also one of the heaviest elements in the periodic table; the time-dilation shift due to the motion of the atom in the trap is therefore reduced. The relatively narrow Th^{3+} electronic transitions allow for ground state cooling, which also aids in decreasing this systematic shift. Finally, the nuclear transition linewidth of $\sim 100\,\mu$Hz and the clock transition frequency $f_{\text{clk}} \approx 2 \cdot 10^{15}$ Hz provide a Q-factor of $\sim 10^{19}$.

A scheme for utilizing this unique nuclear transition is presented in Fig. 26. The clock is composed of the $|5F_{5/2}, I_g = 5/2; F = 5, m_F = \pm5\rangle \leftrightarrow |5F_{5/2}, I_m = 3/2; F = 4, m_F = \pm4\rangle$ transitions. When the frequencies of these transitions split by a weak magnetic field are averaged, they form a virtual clock transition. The ideal state detection is done with the shelving method, utilizing the electronic 690 nm and 984 nm transitions, which are spectrally resolved for the nuclear ground and isomer manifolds. Finally, a $^{232}Th^{3+}$ ion is used for sympathetic cooling. The $^{232}Th^{3+}$ 1088 nm cooling transition is sufficiently detuned from the $^{229}Th^{3+}$ 1088 nm transition due to the large 10 GHz isotope shift, and therefore does not induce a prohibiting light shift.

The dominant systematic shifts are presented in Table 8. When the clock states are chosen to be the eigenstates in the uncoupled basis $|F = I + J, m_F = \pm F\rangle = |J, \pm J\rangle \otimes |I, \pm I\rangle$, the quadratic Zeeman shift is zero and the sensitivity of the nuclear transitions to the environment is dominated by the residuals of the hyperfine and monopole interaction with the electrons [7]. Considering a typical electron admixture level of $\sim 10^{-5}$, the electromagnetic field shifts become smaller by approximately 5 orders of magnitude when compared to the electronic transitions. A detailed analysis
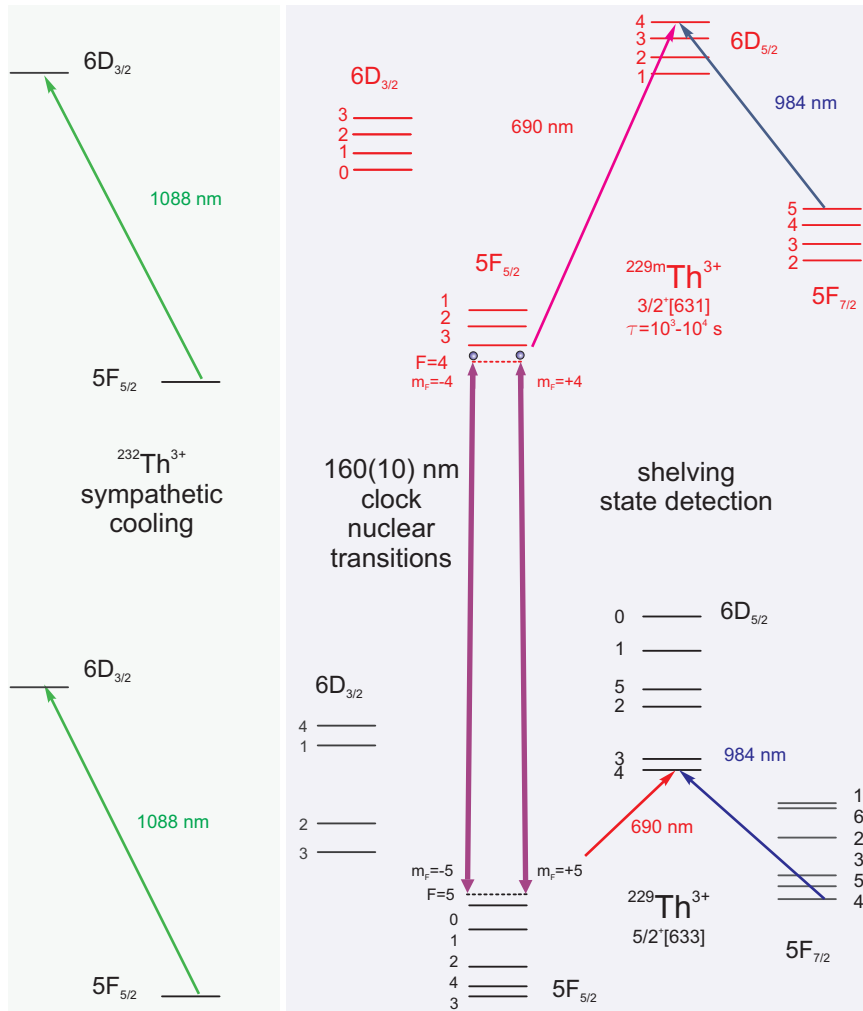
Figure 26: A thorium nuclear clock can be based on the $|5F_{5/2}, I_g = 5/2; F = 5, m_F = \pm 5\rangle \leftrightarrow |5F_{5/2}, I_m = 3/2; F = 4, m_F = \pm 4\rangle$ transitions of a single $^{229}\text{Th}^{3+}$ ion. A single clock $^{229}\text{Th}^{3+}$ ion is sympathetically cooled with a $^{232}\text{Th}^{3+}$ ion. The electronic 690 nm and 984 nm transitions are used for near-unity state detection efficiency (repumper fields are not shown).

.

is provided in Ref. [7].

The isolation of the Thorium nucleus from the environment may allow for a long coherence time even when it is confined in a crystal lattice, promising a solid-state, long-lived quantum memory and solid-state optical clock [41, 42, 85].

Table 8: The systematic shifts for a ^{229}Th^{3+} clock in terms of fractional frequency units $(\Delta f/f_{\text{clk}})$.

Effect	Shift (10^{-20})	Uncertainty (10^{-20})
Excess micromotion	10	10
Gravitational	0	10
Cooling laser Stark	0	5
Electric quadrupole	3	3
Secular motion	5	1
Linear Doppler	0	1
Linear Zeeman	0	1
Background collisions	0	1
Blackbody radiation	0.013	0.013
Clock laser Stark	0	$\ll 0.01$
Trapping field Stark	0	$\ll 0.01$
Quadratic Zeeman	0	0
Total	18	15

The major obstacle towards a thorium nuclear clock is the direct laser excitation of the nuclear transition. The large $\sim 10^{15}$ Hz uncertainty of the nuclear transition frequency and the narrow $\sim 100\,\mu$Hz linewidth makes it a non-trivial task. In this work, a system for the first excitation of this nuclear transition with illumination of the ions for less than a day is developed and described in this and subsequent chapters.

5.1.4 ^{229}Th^{3+} enhanced sensitivity to fundamental constant variation

One of the most attractive features of Thorium-229 is the sensitivity of the ground-isomer nuclear transition to the variation of fundamental constants. Flambaum et al. have predicted that such a frequency ratio is likely to be highly sensitive to the relative variation of the strong interaction parameter and the fine structure constant, with the enhancement factor K possibly reaching as high as 10^6 [8, 45, 46]. This enhancement

is due to the fact that nuclear energy changes on the MeV scale, when compared to the eV atomic energy scale. Although the complexity of this nuclear system makes theoretical evaluation of K difficult [47, 48], a reliable empirical determination of the enhancement factor [49] can be obtained from spectroscopy. The sensitivity of the nuclear transition frequency to α variation is proportional to the change in the nuclear Coulomb energy (ΔV_c) between the ground (g) and isomer (m) states [49]:

$$\frac{\Delta V_c}{(MeV)} \approx -506\frac{\Delta \langle r^2 \rangle}{\langle r^2 \rangle} + 23\frac{\Delta Q_0}{Q_0}, \tag{13}$$

where $\Delta \langle r^2 \rangle = \langle r_m^2 \rangle - \langle r_g^2 \rangle$ is the change in the nucleus radius, and $\Delta Q_0 = Q_m - Q_g$ is the change in the nuclear electric quadrupole moment. These terms can be evaluated with optical and microwave spectroscopy of the ground and isomer level manifolds by measuring the isomeric field shift and hyperfine constant coefficients, as demonstrated here for measurements of Q_g and the ^{229}Th - ^{232}Th relative isotope shifts. These measurements should provide a reliable empirical determination of the enhancement factor with little or no dependence on the nuclear model assumed.

The temporal variation of α can be measured by monitoring the ratio of the frequency of the nuclear transition and that of an atomic (electronic) clock transition, e.g., in Al+, Sr, or in the same ^{229}Th^{3+} ion to mitigate systematic frequency shifts, e.g. with the octupole transition at 432 nm featuring high sensitivity to the alpha variation [86].

5.2   *Apparatus*

The overview of the experimental setup is shown on Fig 27. The apparatus utilized in this work for creating, trapping, and laser cooling ^{232}Th^{3+} and ^{229}Th^{3+} consists of four main parts: a linear Paul trap, vacuum chamber, laser system, and imaging system. All components are described in further detail in this section.
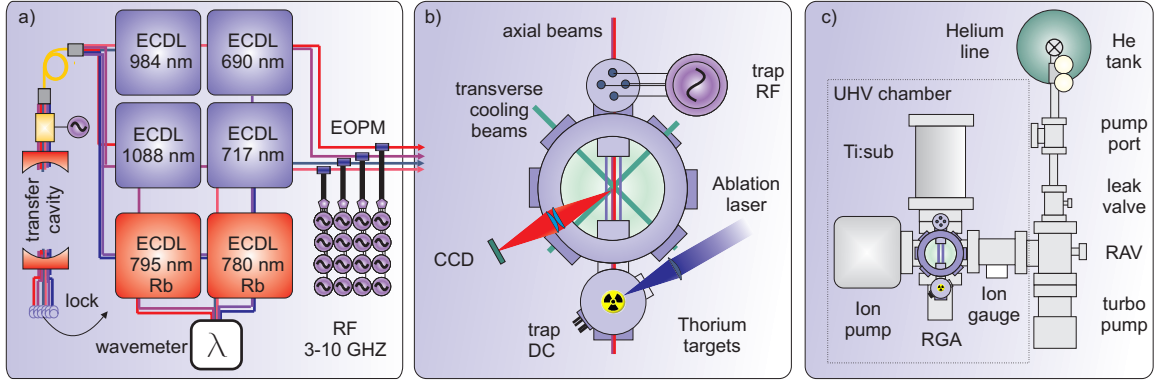
Figure 27: Overview of the experimental setup. a) External Cavity Diode Lasers (ECDL) generate 690 nm, 717 nm, 984 nm, 1088 nm light fields with frequency accuracies of < 100 kHz provided by the transfer cavity locked to a Rb D_2 line. Multiple sidebands of 0-10 GHz are created with Electro-Optical Phase modulators (EOPM). b) Linear rf trap in the octagon of the UHV can be loaded with ions created by the ablation system. Imaging system is used to detect single ions trapped and laser cooled in the trap. c) Ion and Ti:sublimation pumps reduce background pressure to $< 10^{-11}$ Torr, measured by the ion gauge. Helium line, connected to the main UHV chamber with a right angle valve (RAV), is used to supply $< 10^{-4}$ Torr of Helium for the intermediate buffer gas cooling.

5.2.1 Radio Frequency ion trap

The trap design is shown in Fig. 28, 29. The trap is operated in the balanced mode with four dc biased, high-voltage rf signals $U_r + V_0\cos(\Omega t)$ applied to the four rods with the following typical parameters: $\Omega/2\pi = 4.3 - 8$ MHz, $V_0 < 1.5$ kV, $U_r < 200$ V. The radius of the trap $R = 3.3$ mm and the effective radius $R' = 3.9$ mm (Fig.28) provide sufficient confinement of the ions, low scattering of the laser beams, and high optical access with a numerical aperture (NA) of 0.63.

To create sufficient axial confinement with convenient DC voltages, two tube electrodes of length 68 mm and 83 mm, are mounted coaxially with the rf potential and are separated by $L = \zeta Z_0 = 22$ mm at the trap center. The electrodes are biased at $U_z = 0.3 - 50$V. The tapered geometry of the tube's inner diameters creates a potential gradient along the trap axis, inducing ion accumulation and strong confinement between the tubes.
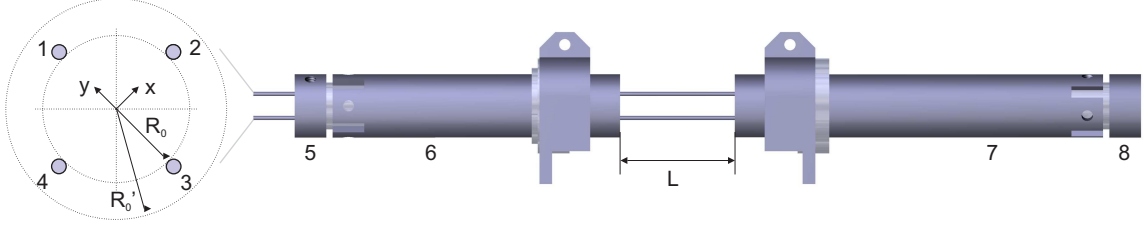
Figure 28: Geometry of the Paul trap for the trapping and laser cooling of Th^{3+} ions. DC biased rf signal is applied to the rod electrodes 1-4, spaced by $2R_0 = 6.6$ mm, which creates radial confinement. DC voltages on electrodes 6 and 7 confine ions in the longitudinal direction. Electrodes 5 and 8 provide additional confinement and time-of-flight mass filtering during loading.
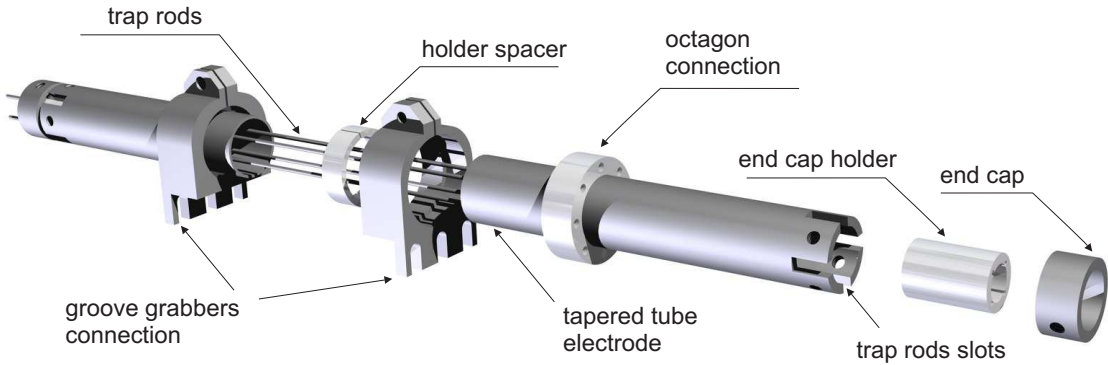
Figure 29: Disassembly of the Paul trap shows the mechanical connections. The electrical connections are made with stainless steel wires spot welded to the electrodes.

The confinement of an ion of mass m and electric charge Q is characterized by the pseudo-harmonic potential, U, and secular frequencies, $\omega_i, i = x, y, z$:

$$U = \sum_{i=x,y,z} \frac{m\omega_i^2 i^2}{2}, \quad \omega_i \approx \frac{1}{2}\Omega\sqrt{a_i + \frac{q_i^2}{2}}(|\mathbf{q}|, |\mathbf{a}| \ll 1), \tag{14}$$

$$q_x = -q_y = q = -\frac{4QV_0}{mR'^2\Omega^2}, q_z = 0 \tag{15}$$

$$a_x = -\frac{4QU_z}{mZ_0^2\Omega^2} + \frac{8QU_r}{mR'^2\Omega^2}, \tag{16}$$

$$a_y = -\frac{4QU_z}{mZ_0^2\Omega^2} - \frac{8QU_r}{mR'^2\Omega^2}, \tag{17}$$

$$a_z = \frac{8QU_z}{mZ_0^2\Omega^2}, \tag{18}$$

where $\zeta \approx 2$ is a geometrical factor .

For this geometry and electric field strengths, the single-ion radial trap frequencies $\omega_{x,y}/2\pi$ for both isotopes are varied between 2 10 kHz - 1 MHz and the axial frequencies $\omega_z/2\pi$ are varied between 15 - 55 kHz during experimental sequences. The motion of a single ion is a harmonic "secular" motion at secular frequency ω_i, with fast amplitude modulation at the rf frequency, called "micromotion":

$$r_i(t) \approx r_{1i}\cos(\omega_i t + \phi_{0i})[1 + \frac{q_i}{2}\cos(\Omega t)], \tag{19}$$

where $\mathbf{r}$ is the position, and ϕ_{0i} is an initial phase. This motion is derived by solving for the Mathieu equations: $\ddot{\mathbf{r}} + [\mathbf{a} + 2\mathbf{q}\cos(\Omega t)]\frac{\Omega^2}{4}\mathbf{r} = 0$. The Th^{3+} ions of amu ≈ 77 are confined for a range of q and a parameters characterized by the stability diagram Fig. 30, which is utilized to filter 80 <amu <$\sim$ 60 with q-ramp down and up protocols that are further described in the next section.

The average kinetic energy of the ion motion in the i-th dimension is

$$E_{Ki} \approx \frac{1}{4}mr_{1i}^2(\omega_i^2 + \frac{1}{8}q_i^2\Omega^2) + \frac{4}{m}(\frac{Qq_iE_i^{dc}}{(2a_i + q_i^2)\Omega})^2 + \frac{1}{64}m(q_iR\alpha\phi_i^{ac}\Omega)^2(1 - \delta_{i,z}), \tag{20}$$

where ϕ_i^{ac} is the phase shift between the voltages of opposite rods $V_0\cos(\Omega t + \frac{1}{2}\phi_i^{ac})$, E_i^{dc} - static electric field components. It consists of a "thermal" energy of secular motion and a kinetic energy of micromotion. While the secular motion can be cooled, the micromotion is driven by the electric field generated by a rf circuit of virtually infinite power, and hence cannot be cooled.

The micromotion consists of the fundamental component and the "excess" created by the parasitic fields due to the asymmetry of the phases and the amplitudes of the rf fields, and the static electric field $\mathbf{E}^{dc}$. The excess portion of the micromotion must be minimized in order to achieve low temperatures with laser cooling. For this purpose, the lengths of the rf transmission wires inside the vacuum chamber are matched and the same phase rf signal pairs are interconnected with 2.2 nF capacitors at the feedthrough for balancing the amplitudes and the phases. Ceramic beads are used to insulate the wires and ensure sufficient distances from other conductors to
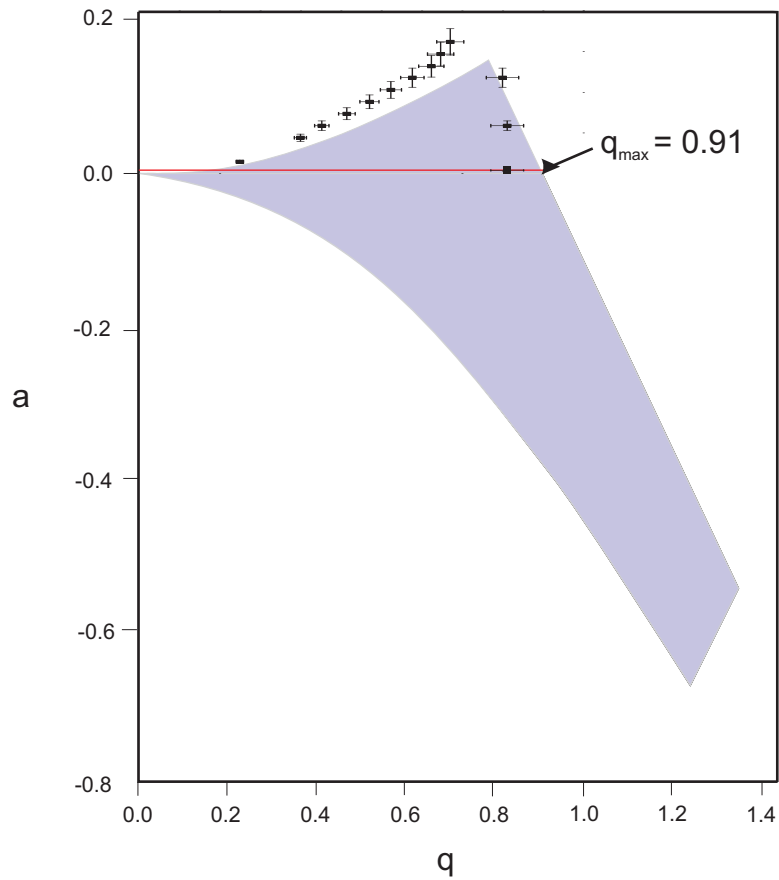
Figure 30: A stability diagram for a hyperbolic Paul trap (shaded region). Experimental data points taken at the edge of the stability of Th^{3+} in the rf Paul trap with cylindrical electrodes. Typically, operation happens at $a \approx 0$, where q is varied from 0.03 to 0.8 to allow for heavy and light mass filtering.

avoid parasitic capacitances. A static DC electric field can be created in both x and y dimensions by the DC biases of the rods for compensation of the static electric field due to the geometric asymmetry and contact potentials formed by the trap electrodes and ablated material.
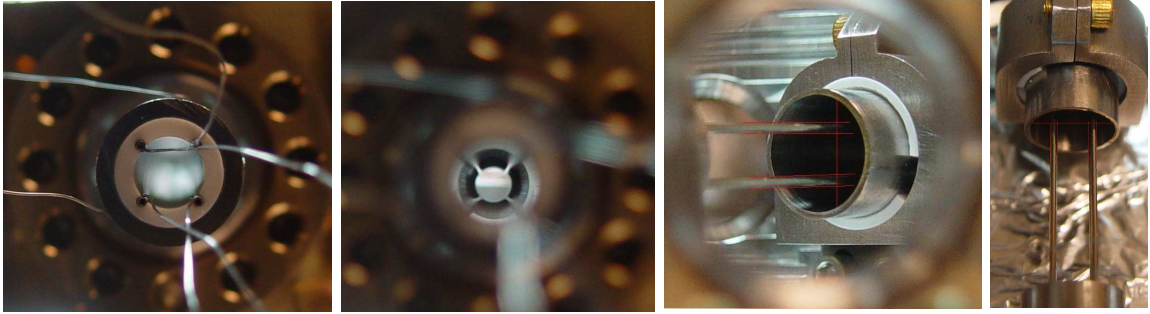
Figure 31: Photographic measurements of the trap alignment. Manual assembly precision of $\sim 150\,\mu\text{m}$, corresponding to 5% of the characteristic trap radial dimensions, is achieved.

For ion loading and time-of-flight filtering, two 6 mm-long ring electrode biased at 250 V are situated at the extreme ends of the trap. The ring electrode voltages are pulsed down to ground and back in sync with ion ablation, allowing the Th^{3+} to enter the trap while blocking much of the slower-moving Th^{2+} and Th^{+}.

The trap insulator parts are machined from Macor, a high loss tangent ceramic, requiring minimized exposure of these parts to high voltage to prevent overheating. This requirement is satisfied since the high voltage rf is needed only for loading and mass filtering, which constitutes a negligible fraction of the experiment duty cycle. In laser cooled regimes, typical rf amplitudes of less than 200 V do not cause noticeable heating.

The trap is assembled to ensure the high accuracy of the alignment. Due to the restrictions for the mounts and the low rigidity of the trap rods, the precision of the alignment is determined by the assembler. With multiple iterations of assembly and photographic measurement (Fig. 31), the misalignment is kept below 150 μm, corresponding to <5% of the characteristic trap radial dimensions.

5.2.2 Ion trap RF source

Efficient loading and mass filtering requires a high q-parameter that scales with the rf amplitude and the driving frequency as V_0/Ω^2. Simultaneously, a higher driving frequency Ω is needed for laser cooling to alleviate the excess micromotion energy due to electrostatic field $E_K^{DC} \sim 1/\Omega^2$. In order to maximize the driving frequency while maintaining $q_{max} \sim 0.9$ for Th^{3+} ions, the trap is driven in the balanced mode with a high voltage four-channel rf source with controllable amplitude (Fig. 32), based on the upgraded SRS RGA electronics. The rf source utilizes the so-called push-pull technique to drive the primary coil of the step-up toroid TR3 with high current at the driving frequency Ω. The latch logical outputs control the dual MOSFET drivers, which gate the main MOSFETs Q1 and Q2. These power transistors create a square waveform current through the primary of the transformer TR3, where only the first harmonic is resonantly amplified, resulting in the four output voltages created by the four secondaries. Each high-voltage rf output is biased for applying static radial electric fields for micromotion minimization. The rf amplitude is controlled by an analog signal gating the MOSFET Q0 that varies the power supply voltage from 0 to 120 V. The circuit draws ~ 1 A at 100 V at maximum power, generating four rf signals up to 1.5 kV amplitudes at frequencies up to 20 MHz, defined by the resonance frequency of the toroid-trap-rods system.

Precise timing of the transistor gating signals is crucial for efficient resonant voltage generation. For this purpose, the clock signal at the doubled rf frequency triggers the latch that generates two synchronous logical signals. The clock signal must be carried in a well-shielded cable and properly connected as close to the latch as possible for the same timing reason. At the frequencies > 10 MHz, the proper clock signal may be produced by biasing a high quality rf generator.

In order to maximize the driving frequency $f = (2\pi\sqrt{(L_0N + L_t)(C_0N + C_t)})^{-1}$, while maintaining sufficiently high $q \sim V_0 \sim N$, the inductance L_t and the capacitance
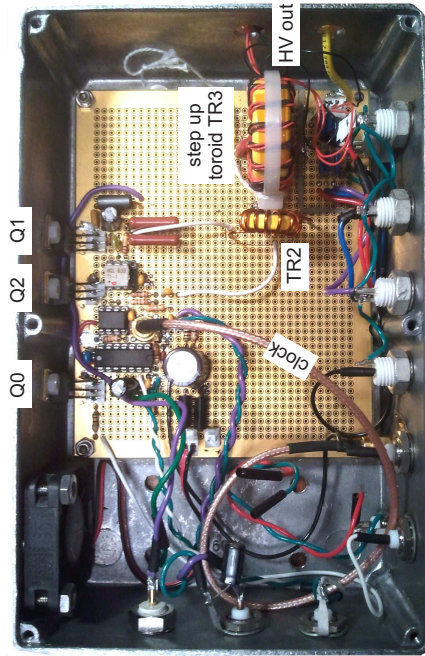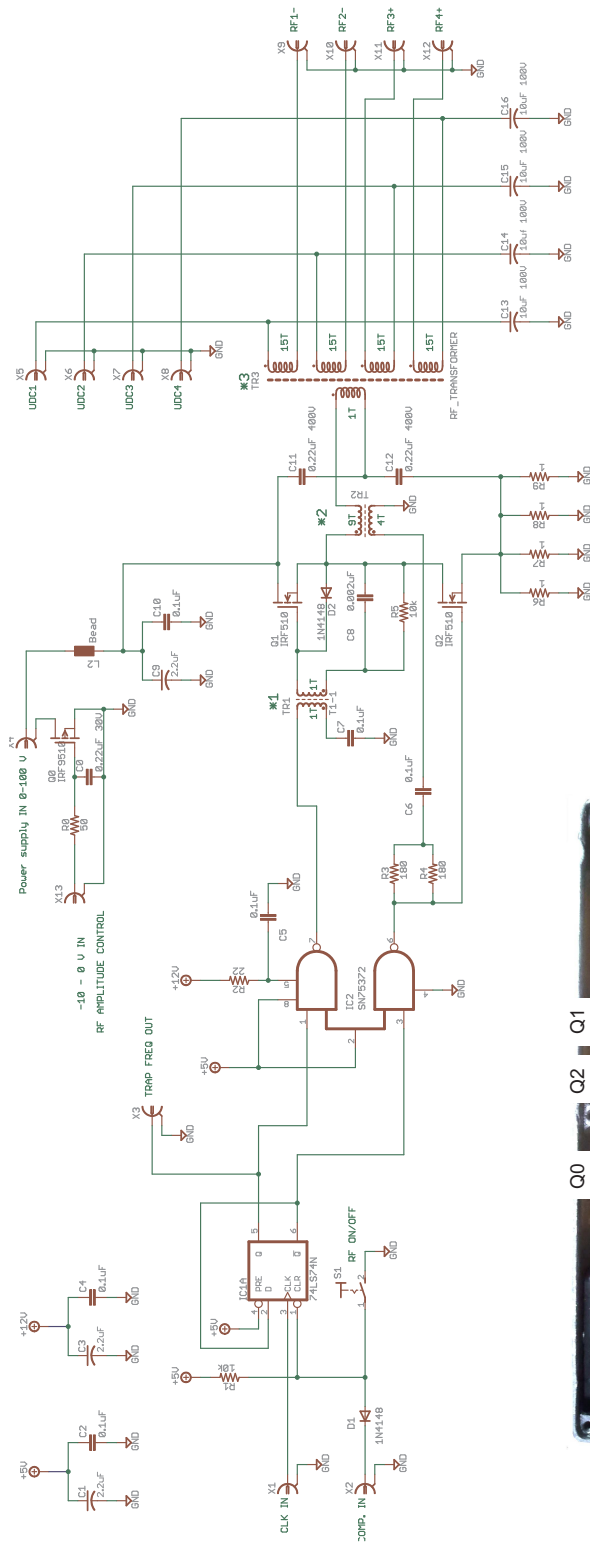
Figure 32: The RF circuit used to generate four sinusoidal high voltages with variable amplitudes up to 1.5 kV$_{pk2pk}$ at frequencies up to 20 MHz with a signal to noise that is better than 60 dB.

C_t of the trap rods and delivery wires are minimized by connecting the step-up toroid TR3 as close to the feedthrough as possible. L_0 and C_0 are the inductance and capacitance of one turn of the TR3 secondaries. The data shown in Fig.33 indicates the resonant frequency is dominated by the step-up toroid TR3.
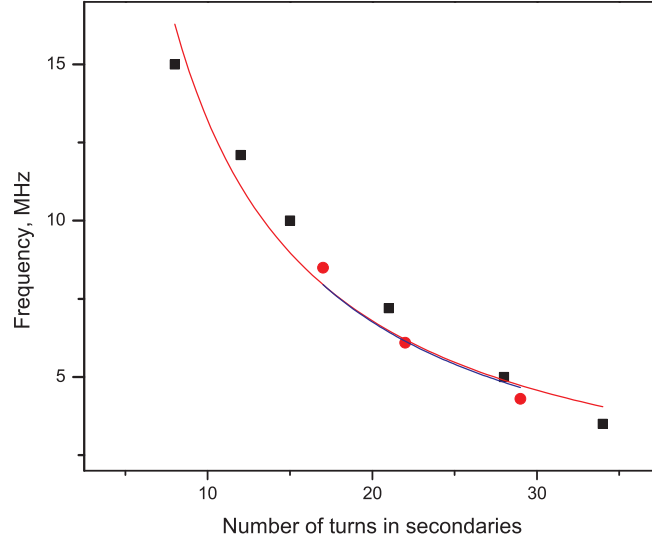
Figure 33: Dependence of the resonant frequencies for two different rf traps upon the number of turns in the secondaries. The curves are fit to the function $f_0/(N - N_0)$ with the parameters f_0=880(40); 850(50) MHz, N_0=0.6(6); 0(fixed).

5.2.3 Vacuum system

The lifetime of the ions in the trap determines the necessary level of vacuum. Several common rules need to be applied in the vacuum design. First, all materials have to be UHV compatible, including the samples substrates. Vacuum conductances and pump speeds of >100 l/s need to be sufficient to achieve pressures $< 10^{-11}$. Mechanical connections should not create gas pockets; particularly, screws have to be slot vented to avoid gas pockets created by the threads and the tips of the screws. Finally, using non-evaporative getters (NEG) placed at the trap may significantly improve the vacuum level.

The rf Paul trap is mounted in the 4.5" spherical octagon of the ultra-high vacuum chamber (Fig.27,34c). Eight viewports provide sufficient optical access for the laser

beams and the imaging system. The linear translation stage with the target samples (Fig. 34) is located near the trap entrance, such that the target is only 10 mm away from the trap.

The Thorium-229 and Thorium-232 nitrate samples are prepared by depositing a solution of $Th(NO_3)_4$ on a 2x2 mm^2 area of a 99.99% pure aluminum substrate (Alfa Aesar 40761). The aluminum substrate allows for an efficient mass filtering, since aluminum and thorium ions have sufficiently different mass to charge ratio. The highest mass-to-charge ratio of Al is 27 amu/e, which is well below Th^{3+} mass-to-charge ratio of 77 amu/e). High purity of the aluminum substrate is neccessary to avoid pollutants with the mass-to-charge ratio close to 77 amu/e.

The viewports have an anti-reflection coating for 984 nm to reduce the scattering of the laser light into the 984 nm imaging system. In order to avoid leaks of the viewports, it is vital to follow the specifications for the maximum temperature, maximum temporal, and spatial temperature gradients. This particularly applies to ordering anti-reflection coatings for the viewports, especially for quartz viewports with low-temperature bond seals. By default, anti-reflection coating companies cool down freshly-coated optics very rapidly, exceeding maximum temporal temperature gradient of the quartz viewports resulting in leakage. A custom order that specifies the maximum temperature and heating and cooling times can avoid this potentially catastrophic issue.

After two weeks of baking at 190 °C, the 40 l/s ion pump and the Ti:sublimation pump allow for $< 10^{-11}$ Torr pressure as measured with the ion gauge. The metal Thorium-232 sample is baked for a second time with local heating by a 8 W cw laser.

The Helium line is connected to the main UHV chamber for introduction of the buffer gas (Fig.27c). High purity (99.999%) Helium gas is supplied by a 300 liter cylinder with a built-in purifier (AirGas, HE BIP300). The pressure is controlled with a stainless steel high purity regulator (AirGas, Y12-C445B580) connected with
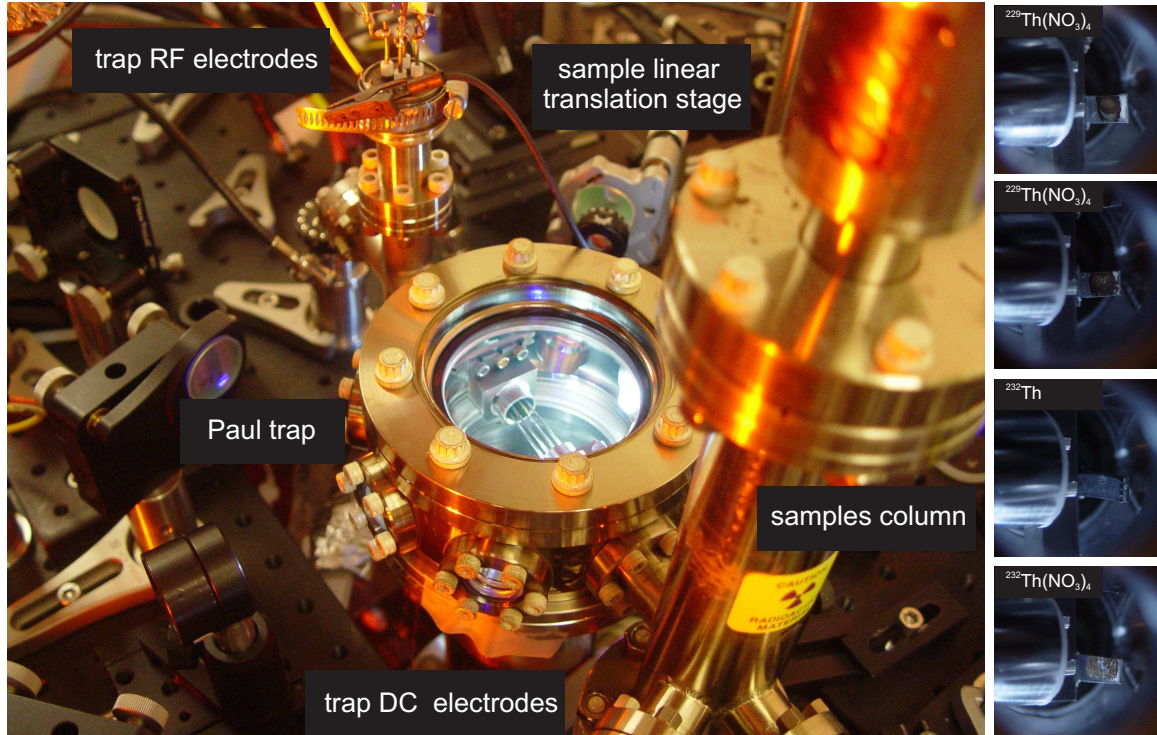
Figure 34: Apparatus for trapping and laser cooling ^{232}Th^{3+} and ^{229}Th^{3+} . The RF Paul trap is mounted in a vacuum chamber with background pressure $< 10^{-11}$ Torr (left panel). A column of targets on a translation stage contains samples of Thorium-232 metal, Thorium-232 nitrate, and two samples of Thorium-229 nitrate (right panel).

a bellow to a 2.75" ConFlat right angle valve for baking and a leak valve. The leak valve's maximum conductance of 0.1 l/s is not enough for efficient baking of the Helium line using pumping from the main chamber, requiring additional pumping for the high pressure side of the Helium line. Finally, the leak valve is connected to the main chamber and a turbo pump through a 4.5" T-angle valve. Using this system, the main UHV chamber can be decoupled from both the turbo pump and the leak valve, which is used to maintain UHV during annual turbo pump replacement.

5.2.4 Laser system

The light fields for exciting visible and near-infrared electronic dipole and quadrupole transitions are created by 690 nm, 717 nm, 984 nm, and 1088 nm External Cavity

Diode Lasers (Fig.27a), with estimated linewidths of < 200 kHz. All laser frequencies are stabilized against a transfer cavity locked to a rubidium wavelength. The sidebands produced by fiber-coupled electro-optical phase modulators (EOPM) are applied for exciting the electronic transitions.

Two broadband concave mirrors form the transfer cavity that is mounted inside a small vacuum chamber. The length of the cavity is stabilized to the 780 nm laser locked to the ^{87}Rb $F = 2 \rightarrow F = 3$ and $F = 2 \rightarrow F = 2$ crossover. An auxiliary 795 nm laser is utilized to select the same cavity length by matching the AOM shifted ^{87}Rb $F = 1 \rightarrow F = 2$ transition with a specific transmission peak of the transfer cavity. The transmission frequencies drift in time with increasing pressure due to the absence of pumping. A FSR decrease from 526.951(4) MHz to 526.838(6) MHz in 20 months is observed. All four laser fields are coupled to the cavity with a common fiber, improving stability and simplifying the optical setup. The low-level chromatic aberrations of the fiber coupler and mode-matching lenses lead to simultaneous cavity mode matching of all four light fields.

The Free Spectral Range (FSR) of 526 MHz is sufficiently large to use the Fizeau interferometers wavemeter (LM-007) to unambiguously lock Thorium lasers to the correct cavity transmission peaks. The 690 nm, 717 nm, 780 nm, 984 nm, and 1088 nm laser fields are combined in a mechanical 1x16 fiber optical switch (Lightwavelink FOSW-1-16-L-9-3), and coupled to the wavemeter. The switch control and the wavemeter data acquisition are combined in one LabView program.

Each of the four fiber-coupled EOPM (EOSpace) for 690 nm, 717 nm, 984 nm, 1088 nm lasers is driven with a multi-component rf signal of < 1 W power to create sidebands for addressing ^{232}Th^{3+} and ^{229}Th^{3+} . Given the 984 nm, 690 nm, 1088 nm isotope shifts of ~ 10 GHz, the laser frequencies are locked in between the transitions of the two isotopes, such that the $3 - 8$ GHz -1 sidebands are resonant with the ^{229}Th^{3+} multiple hyperfine transitions and +1 order excites ^{232}Th^{3+} . The rf

signals are combined in 8-to-1 combiners (Minicircuits ZB8PD-622-S+), and 2x, 3x, 12x frequency multipliers are employed to bring 1 GHz maximum frequency rf generators to the 3-8 GHz range. The remaining input ports of the combiners are used to monitor the spectrum with a rf spectrum analyzer. Each multi-component rf signal is amplified separately and fed into the corresponding EOPM. It is important to maintain sufficiently low rf and optical powers such that frequency mixing, occurring in the rf amplifiers and the phase modulators, does not create parasitic atomic excitations. Third-order mixing processes were observed to generate misleading resonant frequencies. The modulated spectrum is monitored using short optical cavities with FSR≈20 GHz. Since the sidebands and the carrier may have substantially different polarization, the spectra are measured at the trap, where polarizations are defined by the polarization beam splitters.

The UV 269 nm line is excited by a doubled 539 nm light produced by an Optical Parametric Oscillator (OPO) pumped with 355 nm light, similar to the OPO described in the next chapter.

5.2.5 Imaging

The imaging of the ions is done with a NA=0.55 optical system, a 984 nm bandpass filter (5 nm bandwidth), and a low-noise CCD camera (AndOr iKon-M 934 Series). The optical system consists of a 2" diameter aspherical lens with a focal length of 40 mm and a 2" diameter achromatic lens with a focal length of 150 mm. The total detection efficiency of 7.4×10^{-3} is the product of the camera quantum efficiency at 984 nm of 15%, the filter transmission of 70%, and the collection efficiency of 7%. This is consistent with observed 300 counts in a 1 second integration time for a single ion, given the saturated 984 nm scattering rate of $\frac{7}{8} \times \frac{3}{10} \times 235$ kHz ≈ 62 kHz, where 3/10 is the population of the excited state, 7/8 is the 984 branching factor, and 235 kHz is the linewidth of the 984 nm transition. The signal-to-noise ratio of the image

is typically above 100 for laser-cooled ions and limited by the scattering of the 984 nm laser light.

The camera is initially focused on the images of the rods using 984 nm scattered light for their illumination. With known geometry, the focal plane of the imaging system is placed within $\sim 100\,\mu$m of the trap axis.

5.3 Trapping and Cooling

The previously-described apparatus is demonstrated to create ^{232}Th^{3+} and ^{232}Th^{3+} ions with the ablation of Thorium-232 metal, Thorium-232 and Thorium-229 nitrate salt samples, to filter out Th^{3+} from other species and charge states, and to laser cool it down to crystallization. The essential parts of the apparatus are illustrated in Fig. 35. A typical protocol starts with the ablation of one of the samples (Fig. 35a) with a 5 ns, ~ 100 μJ laser pulse at 355 nm. The generated plasma contains Th^{3+} ions along with the pollutant ions of the substrate and the products of the Thorium compounds. The plume propagates at about 10 km/s axially into the linear Paul trap, where the ions are trapped, mass filtered, and laser cooled with the optional assistance of a Helium buffer gas. The ion fluorescence at 984 nm is detected by the imaging system. In this section, the loading protocol is described in chronological order: ablation, mass filtering, and laser cooling.

5.3.1 Loading Th^{3+} with ablation from thorium metal and nitrate salt

Thorium is a refractory metal with a melting point of 2023 K, resulting in low vapor pressures. The total ionization energy towards Th^{3+} is the sum of the intermediate ionization steps.

$$E(\text{Th} \xrightarrow{6.08\text{eV}} \text{Th}^+ \xrightarrow{11.504\text{eV}} \text{Th}^{2+} \xrightarrow{20.003\ \text{eV}} \text{Th}^{3+}) = 37.587\text{eV}. \tag{21}$$

These factors make the photoionization [76] or electron ionization techniques less favorable for creating Th^{3+} than the laser ablation method that is used in this work.
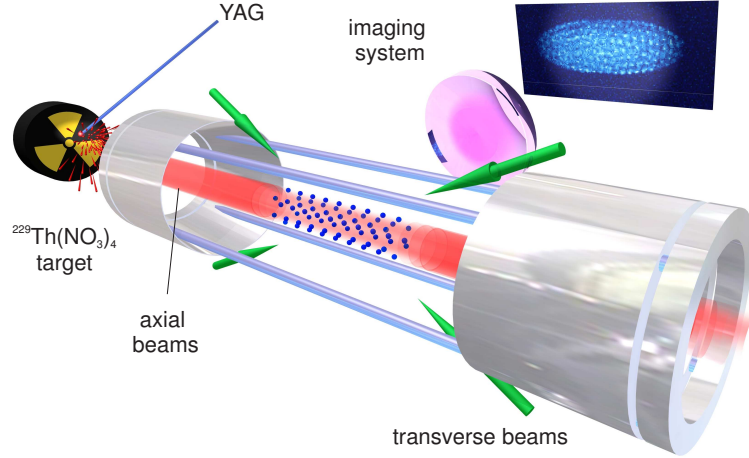
Figure 35: Essential elements of the experimental setup. ^{229}Th^{3+} ions are created via laser ablation from a thorium nitrate source and are injected axially into a four-rod linear Paul trap. Transverse laser beams at 1088 nm cool the ions to tens of Kelvin while axial beams at 690 nm and 984 nm cool the ions to crystallization. Ion fluorescence is collected transverse to the trap for isotope identification and imaging.

Triply charged ^{229}Th and ^{232}Th ions are created via ablation by a 100 μJ, 5 ns pulse at the third harmonic of a YAG laser focused to a 30(20) um spot size on a thorium nitrate or thorium metal source as shown in Fig. 27b. The alignment procedure for the ablation laser is done in two steps. First, rough alignment of the ablation focal point on the sample is done by visual detection of the ablation bursts. Second, the final positioning of the beam waist on the sample is optimized by maximizing the rf shorting signal.

The high ionization potential of 37.6 eV requires a high intensity of $\sim 400\,\mathrm{GW/cm^2}$ to produce a substantial amount of Th^{3+} . Since the plasma generation and the triple ionization are highly nonlinear processes, the concentration of Th^{3+} is strongly dependent on the intensity of the ablation laser. This is observed with the steep dependence that loading efficiency has on the intensity of the ablation laser and consistent with the absence of Th^{3+} in the plasma created by an ablation pulse of 250 MW/cm^2 at 337 nm in Ref. [87].

The speed of $\sim$ 10 km/s for the Th^{3+} corresponds to $\sim$ 40 eV kinetic energy.

A substantial fraction of the ions can therefore be decelerated by the electrostatic potential of the tube at voltages of $\sim 1-50$ V and the end cap at 0-250 V. A correlation between the optimum DC voltage and the ablation laser intensity is observed and is consistent with this hypothesis.

In addition to the electrostatic fields, the ions are influenced by the rf field before and after the rf field is shortened by the plasma. In accordance with Ref. [87] it has been observed that the loading efficiency is independent of the rf phase at the time of the ions entering the trap. While for the trap used in this work a successful loading event of Th^{3+} is 100% correlated with the shortening of the rf, it is believed that the absence of the rf field is not required for trapping based on the following two pieces of evidence. First, in the trap used in Ref. [52], loading was observed without rf shorting. Secondly, manual switching off the rf during loading only decreased loading efficiency.

Finally, once ions are sufficiently slowed to be trapped in the trap potential of ~ 10 eV depth created by the recovered rf and DC fields, ions are confined and cooled by either Helium buffer gas or laser light.

The ablation and loading are typically optimized with a Thorium-232 bulk metal sample, since it does not suffer from depletion and the dominant pollutants Th^+, Th^{2+}, and Th^{4+} are easily filtered. Loading from the bulk metal sample is substantially different from loading with a thin film of multi-element salt on a substrate. Mass filtration during loading becomes crucial for the efficient capture of the element of interest. Fig. 36 shows experimental results of laser ablation from the Thorium-232 nitrate sample and loading of the $^{232}Th^{3+}$ into the Paul trap. Some parts of the sample eventually become depleted as visualized in Fig. 34, necessitating the selection of a new spot after approximately 50 ablation events by moving the ablation laser position. The Fig. 36a presents more than 28 efficient loadings from one spot of the sample. Fig. 36b demonstrates the effect of a light mass filter, which suggests higher

concentration of the substrate material (aluminum) with each ablation event.

The ablation process features random behavior (Fig. 36) with two potential mechanisms responsible for this effect. First, since the surface of the sample is substantially modified with ablation as seen in Fig. 34 and the surface normal defines the direction of the plume propagation, it experiences significant deviations after each ablation event. Secondly, the ablation pulses eventually create a cavity, the walls of which can trap the plasma created at the bottom of the cavity. As observed by reduced rf shorting, it typically takes more than 30 pulses to reduce the amount of created plasma. In addition, sample depletion is possible in the case of loading from a thin film of thorium nitrate.

Compared to the photoionization or electron ionization, the ablation method has a disadvantage of creating a non-negligible amount of pollutants. In the case of thorium nitrate, the concentration of pollutants can greatly exceed the concentration of Th^{3+} (Fig.36). This makes the process of filtering crucial for fluorescence detection and laser cooling.
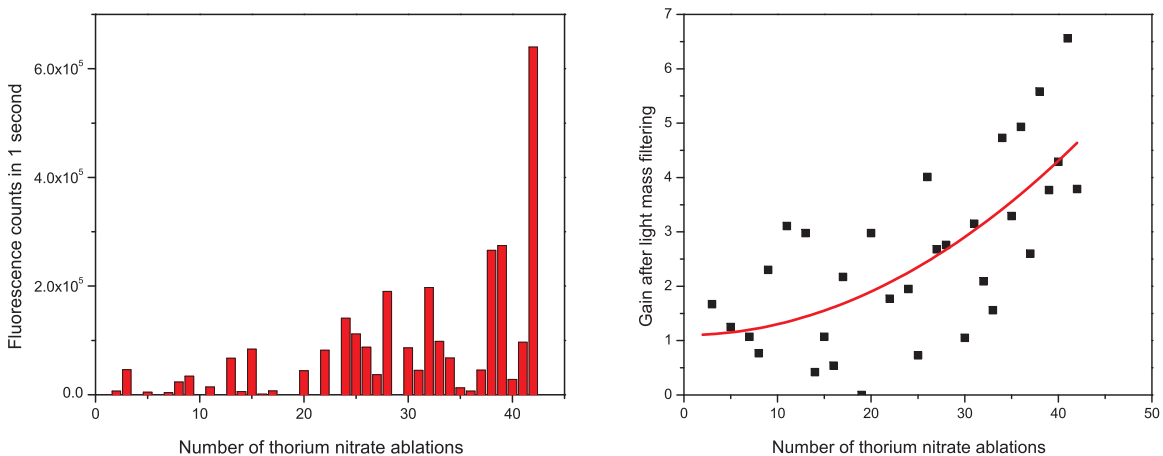
Figure 36: Statistics of loading from a fresh spot of a nitrate sample. Numbers of both $^{232}Th^{3+}$ and light mass pollutants increase on a scale of 20 ablation events.

5.3.2 Mass filtering purification

There are three different mechanisms used in this work for mass filtering: time-of-flight, trap stability parameters, and secular excitation. All three play an important role in the production of pure Th^{3+} crystals.

Time-of-flight filtering is accomplished by increasing the voltage of the front end-cap electrode from ~ 0 to 250 V when Th^{3+} ions are already in the trap, but the Th^{2+} and Th^+ reside outside the trap. The optimum time of the voltage ramp was experimentally found to be 10(2) μs. Depending on the trap geometry, this timing may or may not be dependent on the ablation laser intensity. This spatial separation happens due to the electrostatic force that is a function of the mass-to-charge ratio, providing higher acceleration and speed for Th^{3+} . While this filtering helps to purify the sample, it is not crucial for loading since an efficient loading is still observed even when the end-caps are kept at zero voltage. The Th^{2+} and Th^+ pollutants can be easily filtered out by trap stability modulation.

Trap stability is the most powerful and exhaustive filtering tool with an accuracy of ~ 3 amu. The idea can be elucidated with Fig.30. The trap is typically operated at small, but not zero, a-parameter shown as the red line on the plot. As a result, there are minimum and maximum values of the q-parameter where a particular mass is stable. For the trap used in this work, $q_{min} = 0.025 - 0.04$, and $q_{max} \approx 0.8$. If the rf voltage is set such that for Th^{3+} effective amu $= 77$ $q = q_{min} + \epsilon$, then for all the amu$> 77 + \Delta(\epsilon), q < q_{min}$. This condition leads to the ejection of these "heavy" ions from the trap, where ϵ is the uncertainty of the q_{min} and $\Delta(\epsilon)$ is the resolution of the mass-filter, which can be calculated from (15). This heavy mass filtering process is called "q-ramp down." The same applies for "q-ramp up" to filter out lighter masses: when the voltage is set such that $q = q_{max} - \epsilon$ for amu=77, lighter amu$< 77 - \Delta(\epsilon)$ are ejected. Both q-ramp down and q-ramp up are done on a 50 ms time-scale and expel $\approx 100\%$ of pollutants while keeping $\approx 100\%$ of Th^{3+} with a resolution of 3

a) loaded b) q-ramp up c) q-ramp up with secular excitation d) q-ramp up with secular excitation
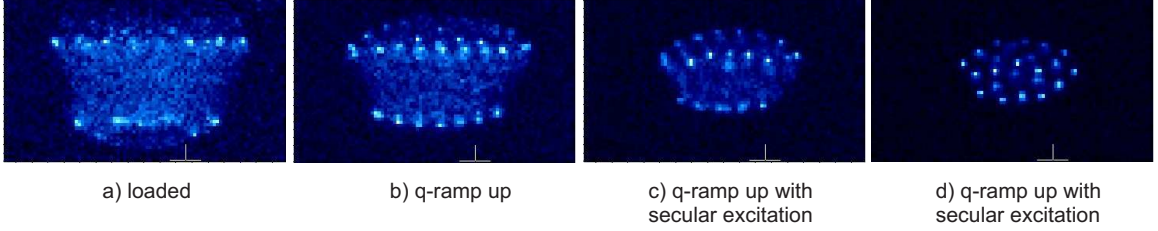
Figure 37: a) Crystal loaded from 232 salt. No secular excitation was applied during loading or q-ramp up. No ^{229}Th^{3+} fluorescence detected. b) q-ramp up without secular excitation c) first q-ramp up with secular excitation at 500 kHz, 5 V settings d) second q-ramp up with secular excitation at 500 kHz, 5 V settings

amu. While the range of the heavy mass filter is determined by the resolution, the range of the light mass filter depends on the maximum achievable q-parameter. This typically defines the driving frequency of the trap at a given trap radius and voltage amplitude limitation of the rf source.

When a higher driving frequency is desired, e.g. for better immunity to the excess micromotion due to static electric fields, the driving frequency can be increased to the level corresponding to $q_{max} = q_{load} \approx 0.4$, the minimum value of the q-parameter required for efficient loading. However, the range of the q-ramp up light mass filter is reduced to amu≈ 39, a value not sufficiently high for the operation. This trade-off can be alleviated by using the secular excitation filtering.

Secular excitation filtering is based on the mechanical resonance of the trapped ions with an external sinusoidal electric field. The secular frequencies are well defined for different mass-to-charge ratios, which leads to the resonant behavior of the heating rate. Ions with a particular mass-to-charge ratio can be driven out of the trap by a relatively small ($\sim$ mV/cm) amplitude electric field oscillating at the radial or axial secular frequencies while keeping the other ions trapped. This technique is used in this work to filter out lighter masses. An rf signal of 12 V amplitude is capacitively coupled to one of the trap rods with a transmission of about 10% by amplitude. Fig.37 illustrates the effectiveness of the secular excitation when q-ramp up is not reaching sufficiently heavy masses in the range of 40-77 amu. The broadband
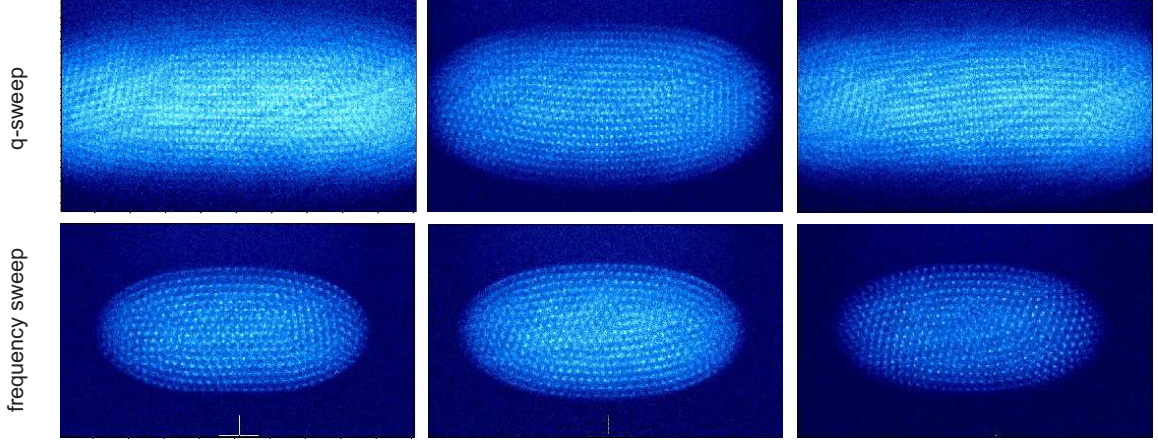
Figure 38: Comparison of the loading efficiency with fixed frequency (a) or q-parameter (b) secular excitation sweeps. The ions are loaded from the bulk Thorium-232 metal sample at the driving rf frequency of 8 MHz. The efficient mass filtering allows for laser cooling without the aid of the buffer gas cooling.

secular excitation filtering can be accomplished either by scanning the frequency of the excitation rf signal while keeping the q-parameter fixed, or by scanning the amplitude of the trapping rf field at a fixed secular excitation frequency. The latter method is easily implemented with the loading and q-ramp up protocol, since the q-parameter is scanned within a vast range. Scanning q-parameter provides a more uniform excitation than scanning frequency, therefore scanning q-parameter can perform a better filtering as observed in Fig. 38. For an 8 MHz trap driving frequency, it was found that a ~1 V, 450 kHz secular excitation during loading and q-ramp up protocol provides the best result.

5.3.3 Laser cooling of Th^{3+}

Once trapped and filtered, laser cooling is sufficient for bringing the ions from tens of thousands of Kelvin to crystallization, though overall yield is consistently $\lesssim$ 100 ions. To increase this yield by 1 - 2 orders of magnitude, a helium buffer gas of impurity $<$ 100 ppb is introduced into the vacuum system at a pressure of 10^{-5} Torr, providing initial cooling to approximately room temperature. The buffer gas is then removed to allow laser cooling to take place. Afterwards, the vacuum environment returns to
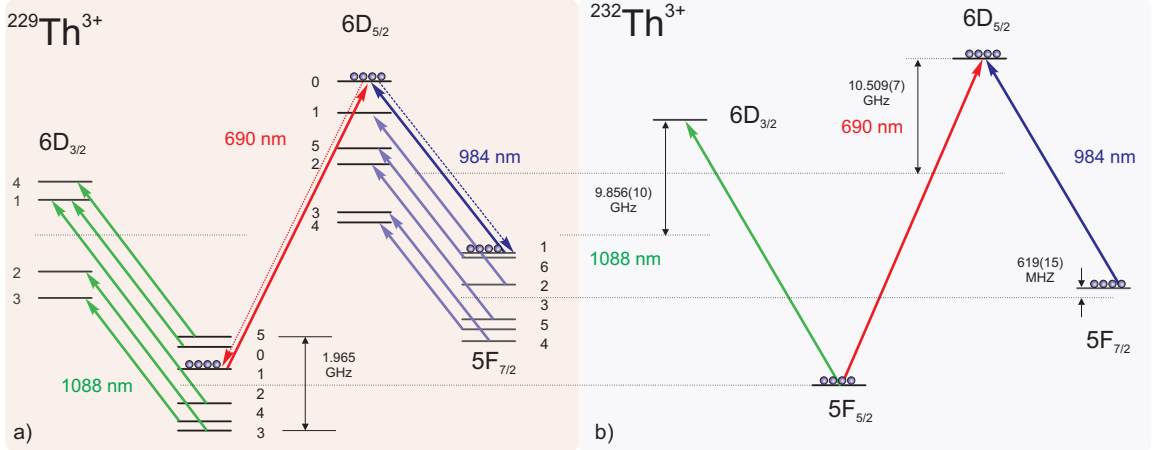
Figure 39: Various optical transitions in $^{232}\text{Th}^{3+}$ and between hyperfine levels in $^{229}\text{Th}^{3+}$ employed during laser cooling.

a base pressure of $< 10^{-11}$ Torr within a few minutes.

Laser cooling of trapped Th^{3+} isotopes proceeds in two stages. First, cooling ions from tens of thousands to tens of Kelvin is achieved by power-broadening the cooling transition to several hundred times its natural linewidths. Subsequently, laser intensities that power-broaden transitions to only several natural linewidths are implemented in cooling the ions into the mK regime.

To scatter light from and laser cool $^{229}\text{Th}^{3+}$ in the steady state, multiple optical fields are required to repump from the various ground ($5F_{5/2}$) and metastable ($5F_{7/2}$) hyperfine levels. Fig. 39 illustrates the relevant energy levels of $^{229}\text{Th}^{3+}$ and the scheme used in this work; the 1088 nm transitions are used in the high-temperature regime, and the closed $|5F_{5/2}, F = 1\rangle$, $|6D_{5/2}, F = 0\rangle$, $|5F_{7/2}, F = 1\rangle$ lambda system is used in the low-temperature regime. In this arrangement, the requirement of multiple finely tuned optical frequencies is relaxed, as only repumping by 1088 nm and 984 nm fields is needed to correct for the off-resonant excitation into the $6D_{5/2}$ manifold. The $^{232}\text{Th}^{3+}$ system has no hyperfine structure, and therefore no such complications arise [52].

In addition to the hyperfine dark states, quantum superpositions of the Zeeman
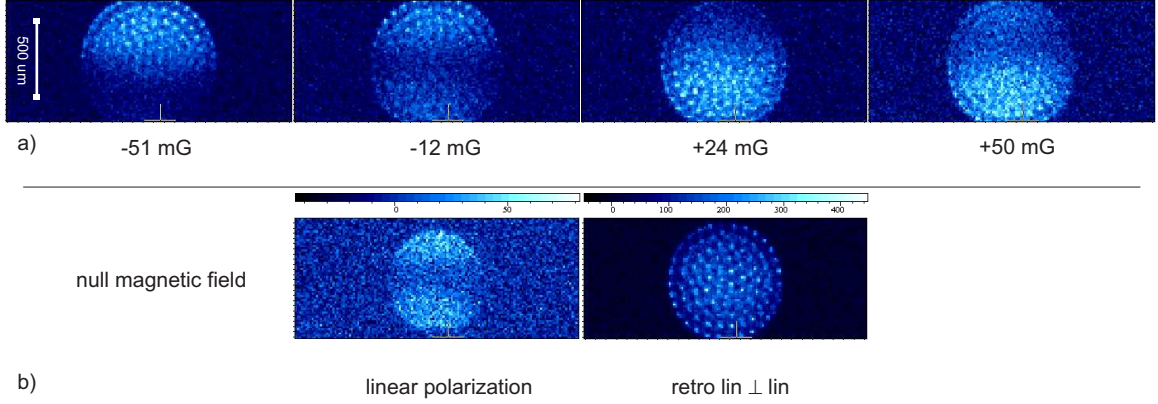
Figure 40: Laser-cooled crystals of ^{232}Th^{3+} . The dark regions are the effect of ions pumped into the dark states, which are superpositions of the Zeeman sublevels. a) With scanning of the DC magnetic field, the region of zero magnetic field required for dark state formation moves due to a magnetic field gradient of ~ 2 G/cm. b) The dark states can be avoided with a retroreflection and 90° polarization rotation of the excitation laser field.

levels with the same total angular momentum can also form dark states. Fig. 40 depicts such dark states, occurring at zero magnetic field. Destabilization of these dark states is crucial for laser cooling, since the scattering, and therefore the cooling rate, can be reduced by more than an order of magnitude (Fig.40b). A non-zero magnetic field and/or a mixed polarization of light is used in this work to prevent this type of dark state.

The 1088 nm transitions of both isotopes are engaged for cooling the sample to tens of Kelvin using two diode lasers. The ^{229}Th^{3+} light is initially passed through a fiber-based electro-optic phase modulator (EOM), acquiring rf sidebands in the 0.1 - 1 GHz range. In total, four 2 mm-diameter beams, oriented in a common plane, converge on the ions at 45 degree angles to the trap axis. The ^{232}Th laser, the ^{229}Th laser carrier, and rf sidebands are tuned such that spectral components are located 20 - 80 MHz below relevant transition frequencies. Each spectral component addressing ^{229}Th^{3+} carries about 1 mW of power per beam, and the ^{232}Th^{3+} field carries about 20 mW per beam. The lower ^{229}Th power is a result of EOM optical insertion loss and the distribution of laser power over multiple rf sidebands.

For low-temperature cooling, transitions from the $5F_{7/2}$ manifolds to the $6D_{5/2}$ manifolds are excited with light from a frequency-stabilized 984 nm diode laser that passes through an EOM, acquiring rf sidebands in the frequency range of 3-8 GHz. The spectral components are placed 3 MHz below the resonant frequencies of the ^{232}Th^{3+} and relevant ^{229}Th^{3+} transitions. The light is then directed to the ions with two 1 mm–diameter beams counter-propagating along the trap axis. Each beam contains about 20 μW of power per spectral component. This beam orientation minimizes the observed micromotion-induced Doppler broadening. A nearly identical system at 690 nm is used to excite from the $5F_{5/2}$ manifolds to the $6D_{5/2}$ manifolds; each 690 nm beam generally carries 60 μW of power in each relevant spectral component. When the ion temperature and Doppler width are reduced via initial 1088 nm laser cooling, the lambda system fields become relevant, cooling both isotopes to crystallization.

Fig. 41 pictures various Wigner crystals of ^{229}Th^{3+} and ^{232}Th^{3+}. The images were taken with different 690 nm fields present, controlling the level of 984 nm fluorescence from each of the two isotopes. The 10.5 GHz isotope shift is much larger than the broadened cooling transition widths of a few MHz, allowing for unambiguous isotopic identification. The relative abundance of the two isotopes (76% ^{229}Th and 24% ^{232}Th) in the thorium nitrate source is reflected in the observed composition of the dual-isotope crystals. When low-temperature laser cooling is not present for one of the two isotopes, an ultra-cold phase is maintained due to the apparent sympathetic cooling. For single-ion excitation and detection, the most robust geometric configuration is the linear ion chain, such as those shown in Fig. 41c,d. Ion localization and position control are maximized while micromotion-induced Doppler broadening and heating are minimized. Ions in this configuration are observed to survive in the trap for a large fraction of an hour. The lifetime is likely limited by charge exchange collisions and chemical reactions with background molecules, processes enhanced by the considerable electron affinity of Th^{3+} [88].
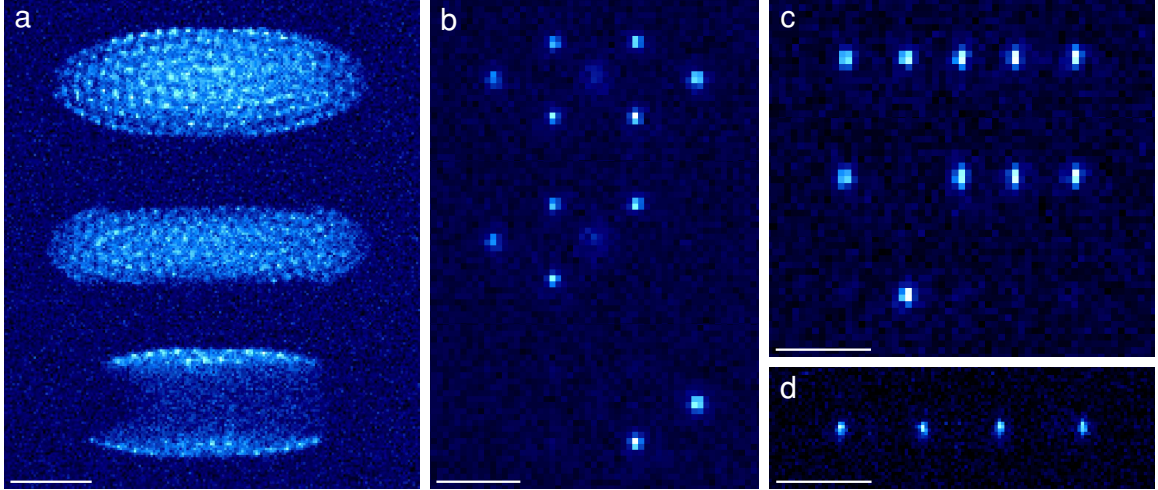
Figure 41: Trapped ^{229}Th^{3+} and ^{232}Th^{3+} ions, laser cooled to crystallization. (a) Three successive images were taken of ~ 200 crystallized Th^{3+} ions. The top image was taken with both ^{229}Th and ^{232}Th 690 nm fields present. The ^{232}Th 690 nm field was then removed for the middle image. For the bottom image, the ^{232}Th 690 nm field was reintroduced and the ^{229}Th 690 nm field simultaneously removed. The larger mass-to-charge ratio of ^{232}Th^{3+} causes its radial accumulation in the outer shells of the crystal. The short focal depth of the imaging system is apparent as most of the ^{232}Th^{3+} shell is out of focus. The integration time is 1 s for all three images. (b), (c) The same imaging protocol used in (a) is used on smaller samples. The integration time is 2 s for all images. (d) A linear chain of four ^{229}Th^{3+} ions is shown. The integration time is 3 s. The scale bar in (a) is 500 μm and in (b)-(d) are 100 μm.

Once the isomer level is found, a single ion within a linear crystallized chain (Fig. 41c,d) can be excited to the isomer manifold, and its hyperfine structure and isomeric level shifts may be accurately measured. This information would allow both unambiguous identification of the isomer level and for an empirical determination of the isomer transition sensitivity to α variation [49].

5.3.4 Lifetime of Thorium ions in a trap

The lifetime of Th^{3+} ions is severely shortened on account of their high charge of 3+. This property makes them prone to exchanging charges with background gases and undergo chemical reactions. The cross sections of such processes are typically greater for higher charge numbers. Also, due to the ablation nature of creating triply charged ions, it is difficult to trap ions without a buffer gas. Both ablation and buffer gas
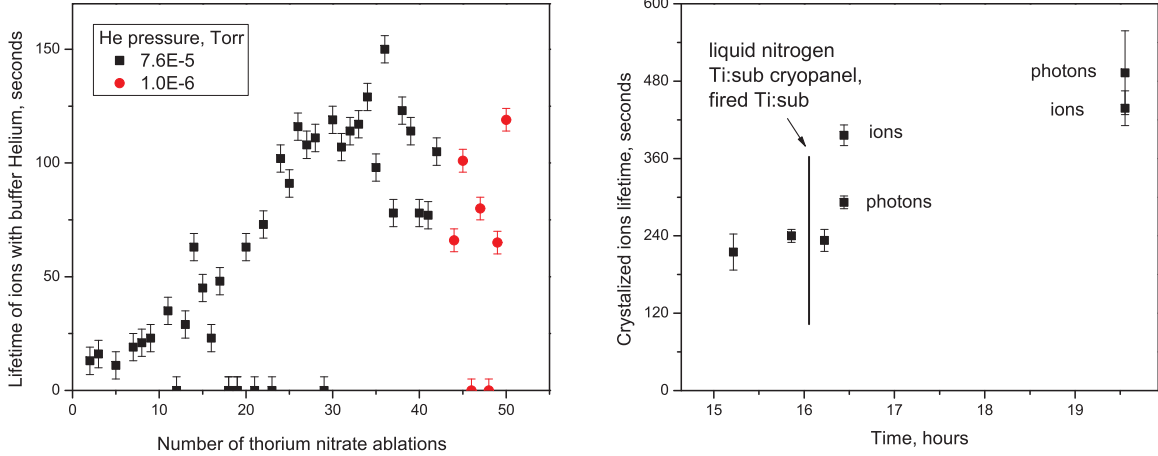
Figure 42: Dependence of $^{232}Th^{3+}$ lifetime in the trap, measured by total fluorescence or by counting the imaged ions. Increase in lifetime with number of ablations suggests that the surface of the sample is being cleaned with the ablation events.

introduce extra pollution.

The impurities of the buffer gas can limit the lifetime of Th^{3+} ions to a few minutes, as indicated in Fig. 42. Decoupled from the buffer gas line, it takes several hours of pumping of the main chamber to restore the lifetime limited by the main chamber background pressure, which is on the order of 20 minutes as measured with ions loaded without buffer gas. Ideally, buffer gas should be avoided because of this drawback.

While reliable loading of $^{232}Th^{3+}$ without a buffer gas from a Thorium metal sample has been demonstrated, loading from a nitrate in a vacuum is not as consistent due to the narrow set of ablation parameters, the sample condition, and purification requirements. The major difference in the case of loading from a nitrate is that the plasma plume mainly consists of a substrate element, not the ion of interest. Hence, mass filtering has to be perfectly tuned and exhaustive, and sets high requirements on the q-parameter that translates to a lower RF driving frequency and a higher voltage amplitude. Loading efficiency and laser cooling also strongly depends on the secular and driving frequencies, with higher frequencies being more advantageous. This trade-off between filtering requirements and high driving frequency
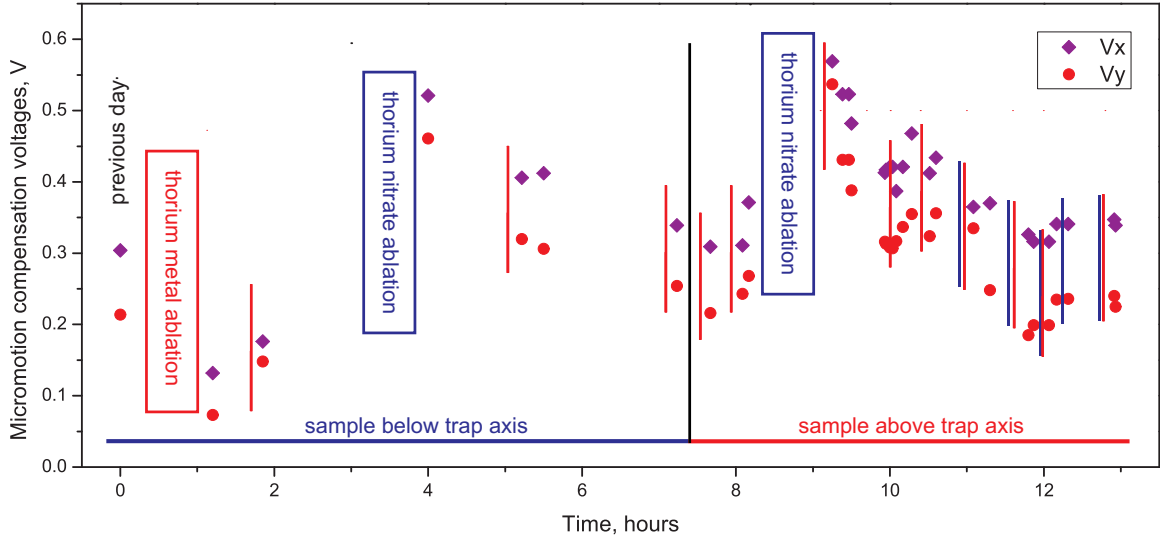
Figure 43: Typical change of the micromotion compensation voltages during a period of 13 hours. Large increases are correlated with nitrate ablation events, likely due to created contact potential on the trap electrode surfaces.

requirements, combined with the other trap parameter restrictions such as trap radius tied to imaging limitations and trap contamination due to ablation, leaves no overlap of optimum parameters for a single Paul trap. A solution to these conflicting requirements is a segmented trap design where loading, mass filtering, and laser cooling are spatially separated.

5.3.5 Contact potentials due to ablation

In addition to increasing the background gas pressure, the ablation process creates a macroscopic number of atoms that enter the Paul trap, which coats the trap electrodes and creates a contact potential of up to 0.5 V. Fig. 43 depicts changes of the electric field at the ion location with respect to time and ablation events. This change can also occur due to other sources of electric field or heat. For instance, it has been observed that turning the ion gauge for about 1 minute increased the DC offsets by 150 mV.

A single ablation event can change the contact potential by almost half a volt, but not necessarily every time. This inconsistency is due to the random nature of

ablation process, since the ablation laser pulse dramatically modifies the surface (Fig. 34).

The electric potentials restore on the scale of few hours. Since the DC electric field in the radial directions on a scale of V/mm increases the kinetic energy up to $10,000$ K, prediction of the DC offsets plays a crucial role in laser cooling. After each ablation event new values for the contact potentials may need to be found without any feedback signal, since at such temperatures the ions can be significantly Doppler broadened and the fluorescence is below the measurement noise.

This problem can be solved by extending the trap design to multiple trap regions to hide the electrodes for the final ion location from the ablation plasma.

To conclude, this chapter introduced the experimental apparatus for trapping and laser cooling ^{232}Th^{3+} and ^{229}Th^{3+} ions. The next chapter presents the main results obtained with this system.

CHAPTER VI

THORIUM-229 SPECTROSCOPY

This chapter is partially based on Ref. [71].

In this chapter, the spectroscopy of ^{229}Th^{3+} ions is presented. The first measurements of the ^{229}Th^{3+} hyperfine structure and the isotope shifts with respect to ^{232}Th^{3+} are presented in Section 2. Based on these measurements, new values for the Thorium-229 nuclear electric quadrupole moment and the nuclear radius difference with respect to the Thorium-232 are derived. The search for the nuclear isomer transition via an electron bridge is discussed in Section 4. To reach the 7P$_{1/2}$ state for the nuclear transition excitation with an electron-bridge, the 717 nm and 269 nm transitions were excited, as described in Sections 5 and 6. The frequency of the $6D_{3/2} \rightarrow 7S_{1/2}$ electric quadrupole transition at 717 nm, and the lifetime of the 7S$_{1/2}$ metastable state are measured for the first time.

6.1 Search for unknown transitions

In general, the search time required to find an atomic transition energy with a single atom can be estimated as

$$T = N_{\text{steps}} \times T_{\text{step}} \sim \frac{\Delta\omega}{\Omega^2}, \tag{22}$$

where $\hbar\Delta\omega$ is the energy range over which the search is conducted, $\Omega = d_{\text{eff}}E/\hbar$ is the resonant optical excitation Rabi frequency, and d_{eff} is the equivalent electric dipole moment of the transition. This result can be obtained by considering Rabi oscillations, when light coherence (τ_l) and atomic coherence (τ_a) times are much longer than the Rabi oscillation period $T_R \sim 1/\Omega$, since $N_{\text{steps}} \sim \Delta\omega/\Omega$, and $T_{\text{step}} \sim 1/\Omega$. Interestingly, formula (22) holds at any combinations of τ_l, τ_a, T_R values. The

numerical factor in front of the expression (22) should be accounted for the search time estimates as it can reach a value of ~ 10. In the next sections, searching for electronic electric dipole, electric quadrupole, and nuclear magnetic dipole transitions is described.

6.2 Measurement of the $^{229}Th^{3+}$ hyperfine structure

Cold ions are ideal for spectroscopy and precision measurements because of their negligible Doppler broadening and long interrogation times. In order to obtain cold $^{229}Th^{3+}$ ions, and effectively manipulate their internal states, optical transition frequencies between the multitude of hyperfine levels must be known at the level of a few MHz. Prior to this work, $^{229}Th^{3+}$ transitions were known with 2 GHz accuracy, based on the $^{232}Th^{3+}$ data [52], theoretical calculations [49, 89], and the nuclear properties of Thorium-229 [74]. The accuracy of 2 GHz is determined by the uncertainties of the nuclear radii of the Thorium isotopes, and the nuclear magnetic dipole and the electric quadrupole moments.

The hyperfine structure is determined by the nuclear spin, I, electron angular momentum, J, magnetic dipole (A) and electric quadrupole (B) hyperfine coefficients. The Thorium-229 nucleus in the ground state possesses a nuclear spin of $I = 5/2$. Its interaction with the electron angular momenta $Jg = 3/2, 5/2, 7/2$ of 1088 nm, 690 nm, 984 nm, leads to a complex hyperfine structure of $4 + 6 + 6 = 22$ levels, and $12 + 15 + 15 = 42$ lines. The higher order moments are typically negligible, however the $^{229}Th^{3+}$ nuclear octupole and hexadecapole moments are expected to be measurable due to the nuclear properties and high angular momenta of the ground and metastable states. The transition energies follow the expression [90]:

$$\delta E_{e,g} = \frac{K_e}{2}A_e + \frac{\frac{3}{2}K_e(K_e+1) - 2I(I+1)J_e(J_e+1)}{4I(2I-1)J_e(2J_e-1)}B_e$$
$$-\frac{K_g}{2}A_g - \frac{\frac{3}{2}K_g(K_g+1) - 2I(I+1)J_g(J_g+1)}{4I(2I-1)J_g(2J_g-1)}B_g + \Delta, \tag{23}$$

where the subscript g(e) indicates the ground (excited) state, and Δ represents the relative isotope shift common to all optical transitions between a given pair of hyperfine manifolds.

In order to laser cool $^{229}\text{Th}^{3+}$ and observe its fluorescence, at least 12 transitions have to be addressed by laser fields simultaneously to avoid dark hyperfine states. The number of unknowns can be reduced to 11, consisting of four pairs of A and B coefficients and three isotope shifts. Because of the initial uncertainties of 2 GHz, 10 MHz Rabi frequencies, and the multidimensionality of the search phase space, the task of finding these transitions is non-trivial. However, due to the large number of ions $> 10^4$ and sensitive fluorescence detection, the laser light can be broadened to a few GHz covering the uncertainty region. This allows for a fast search protocol described later in this section.

Ideally, the search can be done with cold $^{229}\text{Th}^{3+}$ ions, but the unknown atomic spectrum prohibits laser cooling. Alternatively, a sympathetic cooling provided by other ion species can be used. In our case, the Thorium-229 sample contains 30% of Thorium-232, such that laser-cooled $^{232}\text{Th}^{3+}$ can be used for sympathetic cooling of the $^{229}\text{Th}^{3+}$ ions. However, due to the intrinsically low scattering rate of Th^{3+} and the excess micromotion due to the ablation contact potentials, the sympathetic cooling by $^{232}\text{Th}^{3+}$ was not reliably reproducible for the spectroscopy of $^{229}\text{Th}^{3+}$ ions. Direct laser cooling of $^{229}\text{Th}^{3+}$ is therefore necessary. The initial $^{229}\text{Th}^{3+}$ spectrum for $^{229}\text{Th}^{3+}$ laser cooling was obtained with the aid of a buffer gas as subsequently described.

First, the frequencies of the 690 nm and the 984 nm light fields were modulated with 300-500 MHz at to generate $\pm 1, \pm 2, \pm 3$ sidebands in order to observe fluorescence of the $^{229}\text{Th}^{3+}$ ions. This modulation combined with the buffer gas Doppler broadening covers all the lines including 2 GHz uncertainty. The isotope shifts are coarsely measured by maximizing the fluorescence by tuning the carrier frequencies.
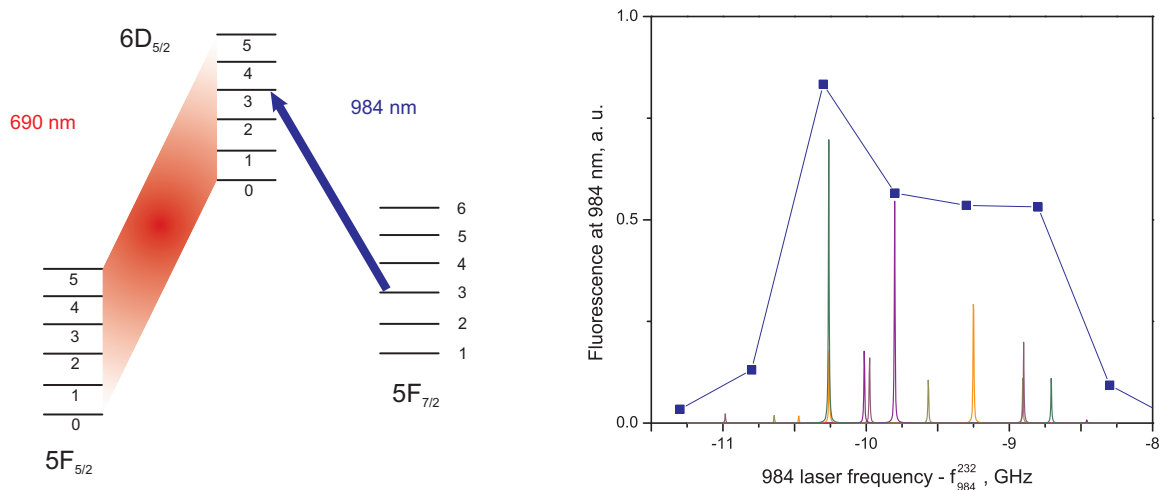
Figure 44: The spectrum of the 984 nm ^{229}Th^{3+} transitions measured by the 984 nm fluorescence in the presence of a buffer gas (squares). The frequency detuning is measured with respect to the 984 nm ^{232}Th^{3+} transition. The energy diagram shows the relevant excitation fields. A broadband 690 nm light field excites all of the ground hyperfine levels, while the monochromatic 984 nm excites various atomic transitions, which are Doppler broadened to ~ 300 MHz. The frequency of the 984 nm light is scanned with the PZT of the laser and measured with a wavemeter with 30 MHz accuracy. The narrow lines represent the resonant cross-sections of the Doppler-free ^{229}Th^{3+} obtained later with laser-cooled samples.

Next, the 690 nm laser with the ~ 3 GHz broadening is set to maximize the fluorescence. The fluorescence dependence on the 984 nm laser frequency as measured is shown in Fig.44.

Secondly, the 690 nm transition scan was performed in the same manner as the previous scan. Fig. 45 shows the 984 nm fluorescence dependence on the frequency of the 690 nm laser without broadening. The 984 nm and the 1088 nm fields with ~ 3 GHz broadening provided repumping from all the metastable and ground hyperfine levels. The 5→4 690 nm transition was unambiguously identified at -12.6 GHz, which aided the spectrscopy of the cooling 1088 nm line.

The 1088 nm transition spectra were obtained in the configuration shown in (Fig. 46). Since the monochromatic 690 nm laser excites only one or a few ground hyperfine levels, the 1088 nm field serves as a repumper and is observed as a modulation of the 984 nm fluorescence. By locking the 690 nm laser at two different frequencies, two
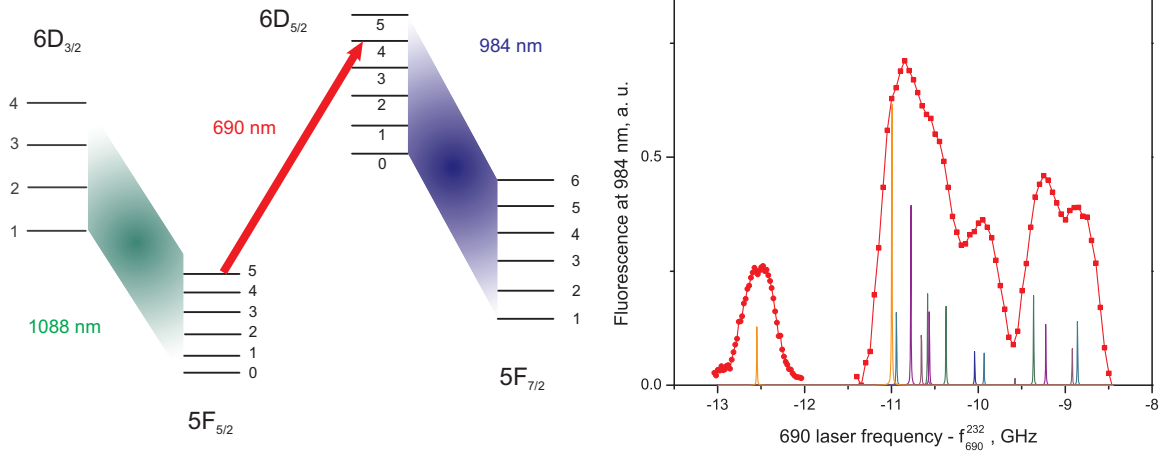
Figure 45: The spectrum of the 690 nm ^{229}Th^{3+} transitions measured by the 984 nm fluorescence in the presence of a buffer gas (squares and circles). The frequency detuning is measured with respect to the 690 nm ^{232}Th^{3+} transition. The energy diagram shows the relevant excitation fields. A broadband 984 nm light field excites all of the metastable hyperfine levels, while the monochromatic 690 nm excites selected atomic transitions, which are Doppler broadened to ~ 300 MHz. The frequency of the 690 nm light is scanned with the rf frequency fed into the phase modulator. Additional scans at different carrier frequencies were performed to distinguish between ± 1 sidebands and to unambiguously label the frequency. The narrow lines represent the resonant cross-sections of the Doppler-free ^{229}Th^{3+} obtained later with laser-cooled samples.

spectra are measured where dips and peaks are dependent on the 690 nm frequency. When the 690 nm laser is tuned to -12.6 GHz, corresponding to the previously identified 690 nm 5→4 transition, the 1088 nm field increases the 984 nm fluorescence when it excites atoms from the ground hyperfine level $F_g \neq 5$ and decreases the fluorescence when $F_g=5$. In contrast, when the 690 nm laser is far detuned from the 5→4 transition at -9.0 GHz, the 1088 nm field increases the 984 nm fluorescence when $F_g=5$. The data shown in Fig. 46 supports this line of reasoning, allowing for identification of the 1088 nm 5→4 frequency -9.75(10) GHz and in agreement with the later measurement (-9.788(6) GHz) with the cold ions. This frequency combined with an initial guess of the hyperfine structure allowed for identifying the 4→4 1088 nm frequency -7.9(1) GHz, in agreement with the 8.016(6) GHz cold sample measurement.

All together these measurements constrained the 1088 nm transitions to an $\sim$100
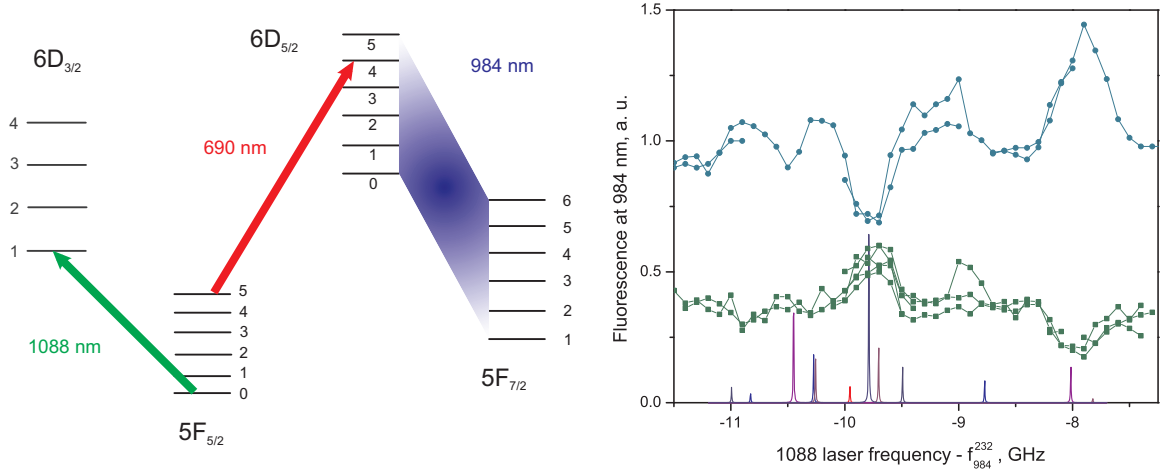
Figure 46: The spectrum of the 1088 nm ^{229}Th^{3+} transitions measured by the 984 nm fluorescence in the presence of a buffer gas, when the 690 nm laser frequency is -12.6 GHz (circles) and -9.0 GHz (squares). The frequency detuning is measured with respect to the 1088 nm ^{232}Th^{3+} transition. The energy diagram shows the relevant excitation fields. A broadband 984 nm light field excites all of the metastable hyperfine levels, while the monochromatic 690 nm and 1088 nm fields excite various atomic transitions, which are Doppler broadened to ~ 300 MHz. The frequency of the 1088 nm light is scanned with the PZT of the laser and measured with a wavemeter with 30 MHz accuracy. The narrow lines represent the resonant cross-sections of the Doppler-free ^{229}Th^{3+} obtained later with laser-cooled samples.

MHz uncertainty. Given that the laser cooling in the high temperature regime occurs at -200..-30 MHz detuning of the transverse 1088 nm cooling beam, this accuracy is sufficient to introduce laser cooling of ^{229}Th^{3+} and to make the phase transition to a crystal state with the aid of the ^{229}Th^{3+} sympathetic cooling, as shown in Fig.47. Once the phase transition occurs, the cooling requirements are relaxed and the crystal can be maintained by the laser cooling of the ^{232}Th^{3+} , which is used to perform the spectroscopy of the ^{229}Th^{3+} hyperfine structure in the cold regime.

When the ions are sympathetically cooled by ^{232}Th^{3+} to tens of mK, the transition Doppler widths are reduced to a few MHz and all optical transitions become clearly resolvable. This allowed for the measurement of the optical frequencies to within a few MHz, using the protocols shown in Fig. 48.

In the first step (Fig. 48a), all 15 transitions at 690 nm were measured by observing

the 984 nm fluorescence and scanning the monochromatic 690 nm laser with the aid of broadband 984 nm and 1088 nm fields. The resonant frequencies were fitted to (23) to obtain the A, B coefficients of the $5F_{5/2}$ and $6D_{5/2}$ levels and the 690 nm line isotope shift.

Next, with the knowledge of the 690 nm lines, the atoms are pumped into a specific ground hyperfine level as shown in Fig. 48b, creating a dark state that reduces the 984 nm fluorescence. Then the monochromatic 1088 nm laser is scanned and the 1088 nm transitions are identified by the maxima of the 984 nm fluorescence. In addition to the resonant frequencies, these measurements provided information for assigning the transitions to particular hyperfine levels since atoms are pumped to a single F-number level. The measured resonant frequencies are fitted to obtain $6D_{3/2}$ A and B coefficients, and the isotope shift of the 1088 nm line.

Finally, only the $5F_{7/2}$ hyperfine structure and 984 nm line isotope shift are left. This is a special case, since all of the unknown hyperfine levels of the metastable $5F_{7/2}$ state have to be addressed with a laser light to generate 984 nm fluorescence for the state detection. While the broadband excitation used in the previous steps can excite atoms from all the levels, it does not provide additional information about the transition frequencies. To circumvent this issue, the selection rule $\Delta F = 0, \pm 1$ is utilized to isolate the levels and measure them one by one. Fig. 49c shows the first step of the protocol. The 1088 nm field is tuned such that the $5F_{5/2}F = 1$
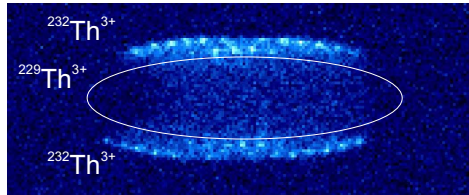
Figure 47: An image of a Wigner crystal, consisting of the ^{229}Th^{3+} ions (dark ellipse region), which are sympathetically cooled by ^{232}Th^{3+} (bright shell). In this cold regime, the ^{229}Th^{3+} 690 nm, 984 nm, 1088 nm transitions between hyperfine levels are well resolved for the measurements.
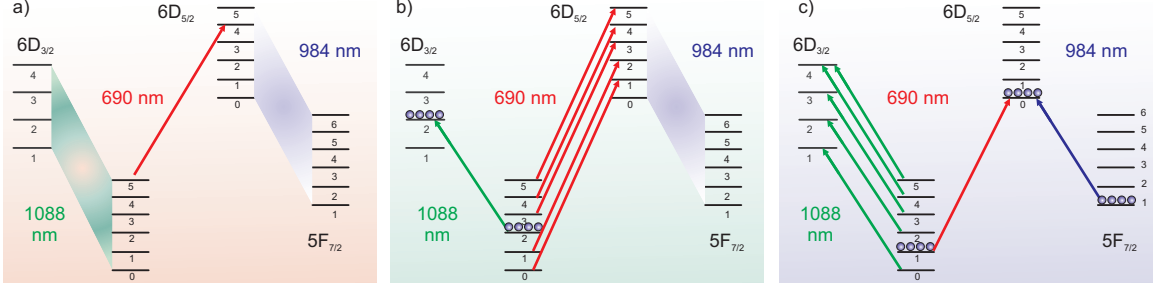
Figure 48: Protocols for the hyperfine spectroscopy in a cold regime. First, all of the 690 nm transition frequencies are measured utilizing broadband 1088 nm and 984 nm repumpers (a). Then these frequencies are used to optically pump atoms to selected hyperfine levels, which allows for measuring the 1088 nm transition frequencies (b). Finally, the 984 nm transition frequencies are measured with the aid of optical pumping and dipole transition selection rules (c).

level is optically pumped and the 690 nm laser excites only the 1→0 transition. In this way, atoms can decay only to the $F = 1$ hyperfine level of the $5F_{7/2}$ manifold. Then the monochromatic 984 nm field is scanned and only one resonance is observed corresponding to the 1→1 984 nm transition.

The 690 nm laser is then tuned to the 1→1 690 nm transition, such that atoms decay to the $F = 1$ and $F = 2$ hyperfine levels of the $5F_{7/2}$ manifold. The $5F_{7/2}F = 1$ level is repumped by the 984 nm laser tuned to the just-identified 1→0 transition, resulting in atoms in the dark $5F_{7/2}F = 2$ state. Then another 984 nm light field is scanned to find the 2→1 transition by repumping atoms from the dark $5F_{7/2}; F = 2$ level, observed by increased fluorescence. This procedure is continued for higher F numbers, by changing the 1088 nm and 690 nm field configurations. Finally, all necessary 984 nm transition frequencies are measured and fitted to obtain the A and B coefficients of the $5F_{7/2}$ level and the 984 nm line isotope shift.

When all three sets of frequencies are measured, a global fit is performed for enhanced accuracy. The final magnetic dipole (A) and electric quadrupole (B) hyperfine coefficients of all four levels and the relative isotope shifts of all three transitions are
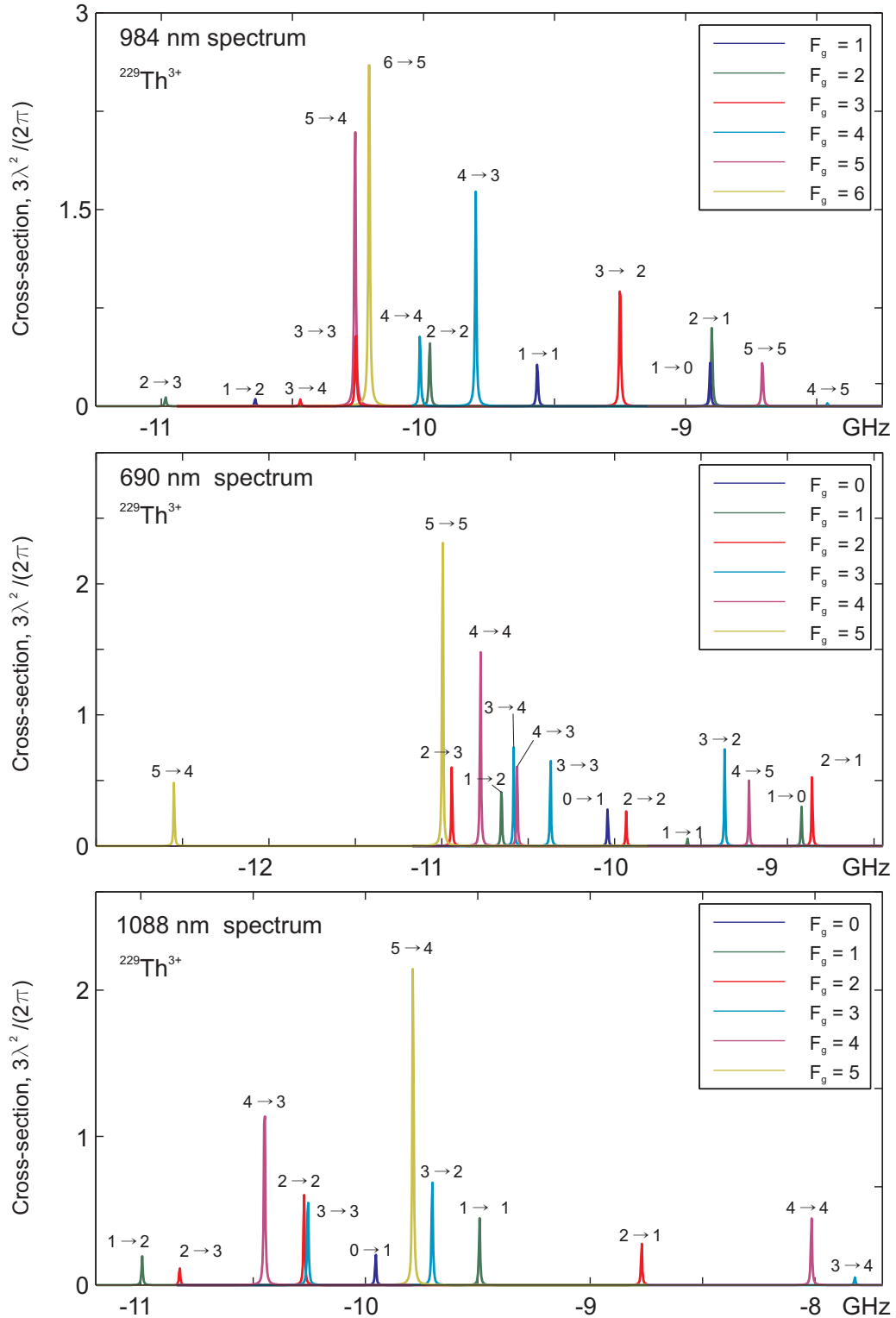
Figure 49: Spectrum of the 690 nm, 984 nm, and 1088 nm ^{229}Th^{3+} lines based on measurements of the magnetic dipole (A) and the electric quadrupole (B) hyperfine coefficients and the isotope shifts. The frequencies are measured with respect to the corresponding transitions in ^{232}Th^{3+} .

extracted directly from the recorded data via a global least-squares fit containing expressions of the form (23). Overall, about 20% of the uncertainty is statistical for each extracted value, while the remaining 80% is due to uncertainties in Zeeman splittings combined with optical pumping effects, laser cooling dynamics, and light shifts. The results of the fit are presented in Table 9 and the derived 1088 nm, 690 nm, 984 nm spectra of ^{229}Th^{3+} in terms of cross-sections is shown in Fig. 49.

Table 9: Measured ^{229}Th^{3+} hyperfine constants A and B and relative isotope shifts from ^{232}Th^{3+}. All units are MHz and all uncertainties are one sigma.

Valence Orbital	A	B	Transition	Isotope Shift
$5F_{5/2}$	82.2(6)	2269(6)	$5F_{5/2} \leftrightarrow 6D_{3/2}$	-9856(10)
$5F_{7/2}$	31.4(7)	2550(12)	$5F_{5/2} \leftrightarrow 6D_{5/2}$	-10509(7)
$6D_{3/2}$	155.3(12)	2265(9)	$5F_{7/2} \leftrightarrow 6D_{5/2}$	-9890(9)
$6D_{5/2}$	-12.6(7)	2694(7)		

The cross-section for a particular transition between hyperfine levels, defined as as the power radiated by the atom divided by the incident energy flux, can be calculated as:

$$\sigma = \frac{4\pi d_q^2}{\epsilon\lambda\hbar\Gamma} = \frac{3\lambda^2}{2\pi} d_q^2 \frac{2J'+1}{2J+1} \frac{1}{|\langle J||er_q||J'\rangle|^2}$$

Using the Wigner-Eckart theorem twice, the dipole moment d_q can be expressed through the reduced dipole moment, $\langle J||er_q||J'\rangle$:

$$d_q = \langle J, F, m|er_q|J', F', m'\rangle =$$

$$= \langle J||er_q||J'\rangle\sqrt{(2F'+1)(2F+1)(2J+1)} \begin{Bmatrix} J & J' & 1 \\ F' & F & I \end{Bmatrix} \begin{pmatrix} F' & 1 & F \\ m & 0 & -m \end{pmatrix}.(24)$$

Assuming uniform distribution among the Zeeman sub-level, the effective dipole moment for π-polarized light is:

$$d^2_{\text{eff}} = \sum_{m=-m_{\text{max}}}^{m_{\text{max}}=\min(F,F')} d^2_m =$$

$$= (2F'+1)(2F+1)(2J+1) \begin{Bmatrix} J & J' & 1 \\ F' & F & I \end{Bmatrix}^2 \sum_{m=-m_{\text{max}}}^{m_{\text{max}}} \begin{pmatrix} F' & 1 & F \\ m & 0 & -m \end{pmatrix}^2 \times$$

$$\times |\langle J||er_q||J'\rangle|^2, \tag{25}$$

Finally, the cross-section of a $F \to F'$ transition is:

$$\sigma_{F \to F'} = \frac{3\lambda^2}{2\pi}(2F'+1)(2F+1)(2J'+1) \begin{Bmatrix} J & J' & 1 \\ F' & F & I \end{Bmatrix}^2 \sum_{m=-m_{\text{max}}}^{m_{\text{max}}} \begin{pmatrix} F' & 1 & F \\ m & 0 & -m \end{pmatrix}^2, \tag{26}$$

where $\sigma_0 = \frac{3\lambda^2}{2\pi}$ in is the cross-section of a two-level system.

The assignments of the frequencies to particular F numbers were based on the initial hyperfine structure information and selection rules utilized in the measurements. Additionally, the global fit for the eight 1088 nm transition frequencies was performed without the assignments, trying all of the 8!=40320 combinations. For that purpose, a least square fitting MATLAB script was run on the School of Physics Condor cluster of ~ 30 computers for a few days. The result confirmed the validity of the initial assignments with the 1.1 MHz root-mean-square of the 8 residuals for the 1→1, 1→2, 3→2, 3→3, 3→4, 4→3, 4→4, 5→4 1088 nm lines.

6.3 ^{229}Th nuclear electric quadrupole moment

The intrinsic nuclear quadrupole moment $Q_0 = \int r^2[3cos^2(\theta)-1]\rho(r)d^3$ is related to the laboratory (spectroscopic) quadrupole moment of the ground rotational mode by ([49]): $Q = ZQ_0\frac{I(2I-1)}{(I+1)(2I+3)}$, where $\rho(r)$ is the electric charge density, normalized to unity, I is nuclear spin, and Z is the atomic number. By taking the unweighted average ratio of the four measured Bs to the corresponding calculated electronic hyperfine matrix elements of Ref. [49], a value of the spectroscopic nuclear electric

quadrupole moment $Q = 3.11(16)$ eb is obtained (Table 10). Since the uncertainty of the experimental values is $< 0.5\%$, the uncertainty of the Q is determined by the stated accuracy of a few percent for the atomic structure calculations, as seen by the deviations of the Q values. Our value for Q may be compared with the previous value of 4.3 eb $\pm$ 20% measured in Th^+ [74].

Table 10: Extraction of the nuclear electric quadrupole moment from the measured hyperfine B coefficients for $^{229}Th^{3+}$ and the theoretical calculations.

Level	B/Q, MHz/eb	B, MHz	Q, eb	deviation
$5F_{5/2}$	740	2269(6)	3.07	1.5%
$5F_{7/2}$	860	2550(12)	2.97	4.7%
$6D_{3/2}$	690	2265(9)	3.28	5.5%
$6D_{5/2}$	860	2694(7)	3.13	0.67 %
		Average	3.11	

After completion of the measurements, we became aware of the uncommonly cited Ref. [73], where the value of $Q = 3.149 \pm 0.032$ eb for ^{229}Th was determined via a Coulomb excitation of the nucleus, and is in a good agreement with our result.

The value of the nuclear ground state electric quadrupole moment and the measured hyperfine B coefficients are important to future determination of the nuclear isomer hyperfine structure and extracting the nuclear isomer state electric quadrupole moment. The latter is expected to constitute a significant fraction of the nuclear Coulomb energy difference ΔV_C, according to the expression (13), which defines sensitivity of the nuclear transition frequency to variation of the fundamental constants [49]. The second major component of the nuclear Coulomb energy difference is the change in the radius of the nucleus between the two states. This change leads to an isomer shift of the electronic transitions in analogue to the isotope shift due to the difference between ^{229}Th-^{232}Th nuclear radii, which is analyzed in the next section.

6.4 The difference between ^{229}Th-^{232}Th nuclear radii

With the measured isotope shifts and the theoretical calculations of Berengut et. al, [49], a new value for $\delta\langle r^2\rangle = \langle r^2\rangle_{229} - \langle r^2\rangle_{232}$ fm^2 can be obtained. Table 11 shows the experimentally measured energy shifts, theoretical energy shifts coefficients, and derived $\delta\langle r^2\rangle$ for the $5F_{7/2}$, $6D_{7/2}$, $6D_{7/2}$ levels with respect to $5F_{5/2}$.

Table 11: Extraction of the difference in ^{229}Th-^{232}Th nuclear radii from the isotope shifts of 1088 nm, 984 nm, 690 nm lines.

Level	$\Delta E/\delta\langle r^2\rangle$, GHz/fm^2	ΔE, GHz	$\langle r^2\rangle_{229} - \langle r^2\rangle_{232}$ fm^2	weight	deviation
$5F_{7/2}$	2(2)	-0.619(11)	-0.310	0.03	3.2%
$6D_{3/2}$	33(8)	-9.856(10)	-0.299	0.46	-0.4%
$6D_{5/2}$	35(8)	-10.509(11)	-0.300	0.52	0.2%
		Weighted average	-0.300		
		and standard deviation	0.002		

The experimental accuracy of 0.1 % for the $6D$ levels and 2% for the $5F_{7/2}$ level shifts is considerably smaller than the accuracy of the theoretical calculations, therefore the uncertainty of the $\delta\langle r^2\rangle$ is determined by the few percent accuracy of the calculations. Conservatively, the uncertainty is 0.015. If the calculations deviations for different levels are not correlated, then the uncertainty is reduced by weighted averaging over the three datapoints to the 0.002 value.

In conclusion, the change in the nuclear radii of Thorium-229 and Thorium-232 isotopes is evaluated $\langle r^2\rangle_{229} - \langle r^2\rangle_{232} = -0.300 \pm 0.002_{\text{stat}} \pm 0.072_{\text{syst}}$ fm^2, which is in agreement with the $-0.334(45)$ fm^2 value [72]. This measurement is useful for the future spectroscopy of the neutral and ionic forms of Thorium-229.

6.5 ^{229}Th nuclear isomer transition via a $^{229}Th^{3+}$ electron bridge

The most recent and precise published measurement of the ^{229}Th isomer energy is 7.6(5) eV [39]. In order to span $\pm\,3\,\sigma$ in the search for this nuclear level, direct optical excitation of the isomer in trapped cold ions may not be a viable method, given available UV sources and the large energy uncertainty. Instead, the electron bridge (EB) process may be utilized [52], as shown in Fig. 50. In this case, hyperfine-induced mixing of the ground and the isomer nuclear manifolds opens electric-dipole transitions between the two. The mixing is expected to be the strongest for the S-electronic states, as the electron probability density at the nucleus is highest. For example, considering only the $7S_{1/2}$ and $8S_{1/2}$ electronic orbitals in first-order perturbation theory,

$$|\widetilde{7S_{1/2},m}\rangle \approx |7S_{1/2},m\rangle + \frac{\langle 8S_{1/2},g|H_{int}|7S_{1/2},m\rangle}{E_{7S,m}-E_{8S,g}}|8S_{1/2},g\rangle \qquad (27)$$

where H_{int} is the electron-nucleus interaction Hamiltonian and $g(m)$ indicates the nuclear ground (isomer) level. The $|8S_{1/2},g\rangle$ admixture, with an expected amplitude of order 10^{-5} [91], couples to the $|7P_{1/2},g\rangle$ level via electric-dipole radiation of frequency $(E_{7S,m}-E_{7P_{1/2},g})/\hbar$ (see Fig. 5). This shifts the spectral interrogation region from the challenging 130-200 nm range to the manageable 250 - 800 nm range.

Considering the $|7P_{1/2},g\rangle \leftrightarrow |7S_{1/2},m\rangle$ electron bridge, an effective electric dipole moment, d_{EB}, is predicted to be $\approx 2 \times 10^{-5}\,e\,a_0$ [91]. It should be noted that this electron-bridge transition is predicted to be substantially stronger than the nuclear M1 transition [91]. For an ion in the $|7P_{1/2},g\rangle$ level, placed at the center of a Gaussian light beam of power P and waist r_0, $\Omega^2 = (4\,P\,d_{EB}{}^2)/(\pi\,\epsilon_0 c\,r_0{}^2\hbar^2)$ so that $T \sim (\pi\,\epsilon_0 c\,r_0{}^2\hbar^2\Delta\omega)/(4\,P\,d_{EB}{}^2)$, according to (22). With realistic $r_0 = 20\,\mu$m and $T < 1$ day, the power requirement is 100 mW. The laser systems for covering the 250-800 nm uncertainty range and providing this amount of power are described in the following sections.
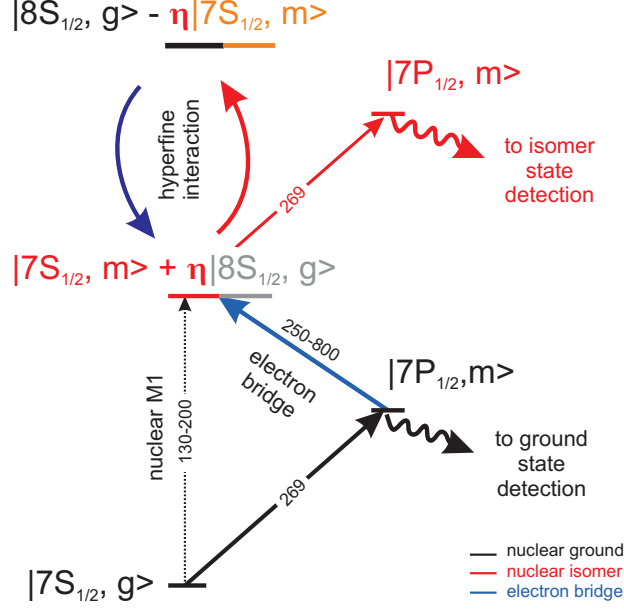
Figure 50: Direct nuclear M1 and electron-bridge $|7P_{1/2}, g\rangle \rightarrow |7S_{1/2}, m\rangle$ nuclear excitation schemes. The hyperfine interaction between the nucleus and the valence electron admixes electronic levels of the nuclear ground and nuclear isomer levels through $|8S_{1/2}, g\rangle$ and $|7S_{1/2}, m\rangle$ levels. This creates a $|7P_{1/2}, g\rangle \leftrightarrow |7S_{1/2}, m\rangle$ electron bridge with effective dipole moment $d_{EB} \approx 2 \times 10^{-5}\, e\, a_0$, which is substantially stronger then the bare nuclear M1 transition, and corresponds to a more convenient wavelength range.

The search using the electron bridge consists of three tasks: obtaining laser-cooled $^{229}\text{Th}^{3+}$, excitation to the $|7P_{1/2}, g\rangle$ level, and illuminating the ions with a sufficiently high intensity light, tunable in the 250-800 nm range. The chains of laser-cooled $^{229}\text{Th}^{3+}$ ions, as shown in Fig. 41d, provide near-unity detection efficiency of the isomer state and strong localization for tight focusing of the search light. In addition, the ionization potential of Th^{3+} is 29 eV, making multi-photon ionization with this protocol unlikely.

The cold $^{229}\text{Th}^{3+}$ ions allow for numerous ways to reach the electron-bridge initial state. The nanosecond lifetime of the $7P_{1/2}$ state defines the choice of the excitation scheme for a particular laser system. For the high repetition rate lasers, both 269 nm and 196 nm lines have to be excited in order to maintain population in the $7P_{1/2}$. With longer time periods between the pulses, however, the electric quadrupole transition at

717 nm can be used instead of the inconvenient 196 nm line. In the next sections, the excitation to the $7P_{1/2}$ via the three step process: 1088 nm $5F_{5/2} \rightarrow 6D_{3/2}$, followed by 717 nm electric quadrupole transition $6D_{3/2} \rightarrow 7S_{1/2}$ and the $7S_{1/2} \rightarrow 7P_{1/2}$ 269 nm D_1 line is described. It should be noted that an alternative, less complex scheme $5F_{5/2} \rightarrow 7P_{1/2}$ two-photon excitation with 329 nm is also possible but requires high energy pulses. It is confirmed that Th^{3+} ions are kept crystallized even when they interact with 100 mJ, 5 ns, 10 Hz, 355 nm pulses focused into a 40 μm diameter beam. Since the 329 nm excitation scheme requires light with much less intensity, it should be realizable.

6.6 *Electronic electric quadrupole transition at 717 nm*

The initial $|7P_{1/2}, g\rangle$ state of the electron bridge can be reached via 269 nm or 196 nm light. The $7S_{1/2} \rightarrow 7P_{1/2}$ 269 nm D_1 line is preferable because of the more available light sources and relaxed requirements on UV transmission. In order to populate the $7S_{1/2}$ level, the 717 nm electric quadrupole transition $6D_{3/2} \rightarrow 7S_{1/2}$ is utilized.

The quadrupole Rabi frequency between states $|i\rangle$ and $|f\rangle$ due to electric field of amplitude $\mathbf{E}_0$ and wavevector $\mathbf{k}$ is:

$$\Omega_Q = \frac{k_\alpha \langle i|Q_{\alpha\beta}|f\rangle (E_0)_\beta}{\hbar} \tag{28}$$

The electric quadrupole matrix element $\langle i|Q_{\alpha\beta}|f\rangle$ can be obtained using the Wigner-Eckart theorem and the reduced electric quadrupole moment $\langle 6D_{3/2}||Q_{\alpha\beta}||7S_{1/2}\rangle = 7.0631\, ea_0^2$ from Ref. [83].

The 717 nm light is created by an ECDL. The laser is based on a 705 nm diode (Opnext HL7002MG). Remarkably, the laser operates 12.5 nm away from the central wavelength at room temperature. The laser is locked to the transfer cavity as described in the previous chapter and the output frequency is controlled by the rf signal, supplied to the 717 nm electro-optical phase modulator. The optical power
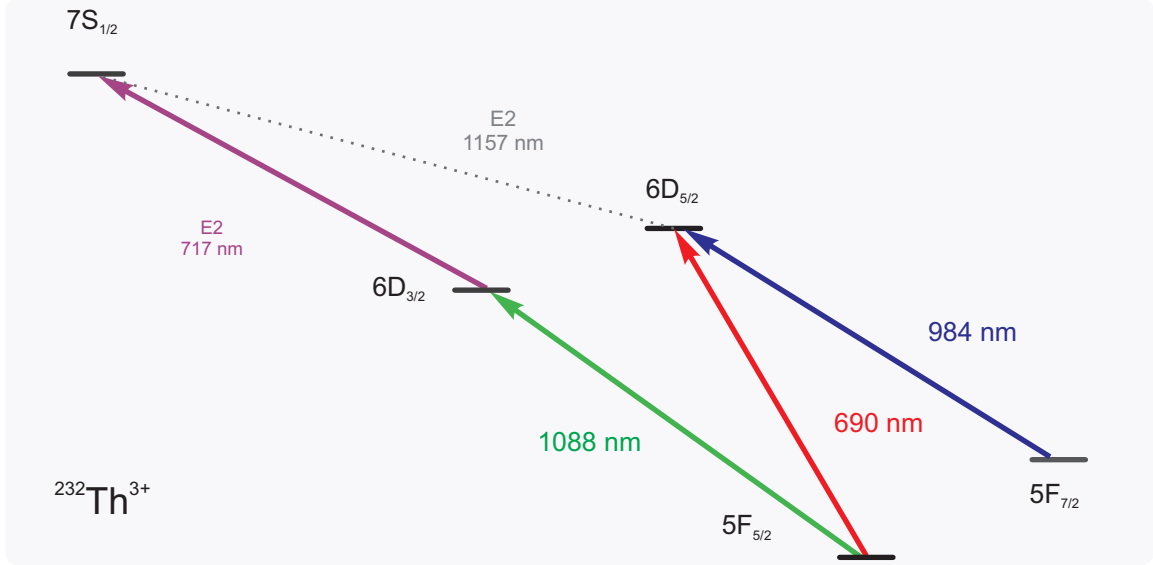
Figure 51: A scheme for excitation of the 717 nm electric quadrupole transition $6D_{3/2} \rightarrow 7S_{1/2}$ transition. The state detection is done by the 984 nm fluorescence measurement.

in the +1 sideband of 1 mW, focused to 110 um diameter corresponds to the electric quadrupole Rabi frequency of ~ 100 kHz. The discharge data [82] suggests a frequency of 417835(2) GHz. According to formula (22) and the 2 GHz uncertainty, the minimum search time is on the order of 1 s.

The search protocol (Fig. 51) consists of two parts: excitation to the metastable $7S_{1/2}$ level and the measurement of its population. For excitation, the atoms are repumped to the ground level with 984 nm light, excited to $6D_{3/2}$ level with an axial 1088 nm light with ~ 10 MHz Rabi frequency, and the cw 717 nm laser frequency is scanned around the initial guess. The detection is accomplished by measuring the population in the other $5F_{7/2}$ metastable state. If an ion makes a transition to the metastable $7S_{1/2}$, the ion becomes dark for the 984 nm fluorescence detection, as shown in the Fig. 52. For the search, the interaction time is chosen to be 0.5 s, which is greater than the detection time of 0.1 s, but less than the theoretically predicted [83] 0.59 s lifetime.

The 717 nm laser frequency broadened to 500 MHz was scanned with 500 MHz
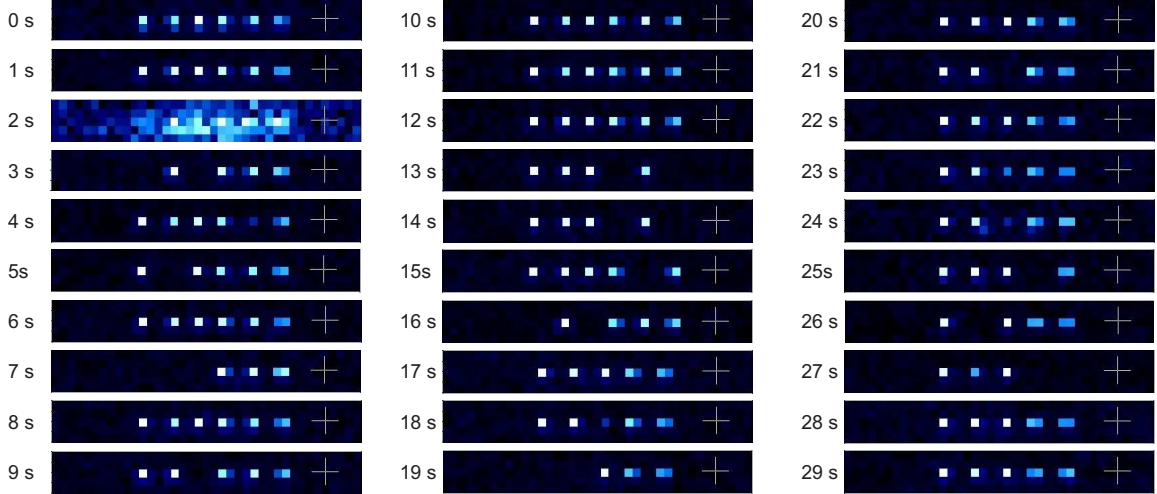
Figure 52: A sequence of images of the ^{232}Th^{3+} demonstrating excitation to the metastable $7S_{1/2}$ level with the 717 nm electric quadrupole transition. A dark spot corresponds to the excitation of the ^{232}Th^{3+} ion to the metastable $7S_{1/2}$ level, rather than a pollutant ion, because the constant chain structure and expected sensitivity to the 717 nm frequency. An ion was lost between 16 s and 17 s frames, as seen by the corresponding shifts of the ions.

steps until the first transition was detected, and the frequency was recorded. Then the sequence was changed to optimize the excitation rate with a shorter excitation time of 50 ms, and the transition was mapped, as shown in Fig. 53a. The frequency of the ^{232}Th^{3+} $6D_{3/2} \rightarrow 7S_{1/2}$ transition, 417 845 964(30) MHz, is derived from the fit and the wavemeter measurement. The uncertainty is dominated by the LM-007 wavemeter accuracy. The measured transition frequency is $\approx$10 GHz higher than predicted by the Ref. [82], suggesting an estimate of the systematic errors of the discharge spectrscopy data.

The ^{229}Th^{3+} -^{232}Th^{3+} isotope shift coefficients for the $7S_{1/2}$ and $6D_{3/2}$ levels are 146(4) GHz/fm^2 and 33(5) GHz^2, respectively [49]. The evaluated radius change $\langle r^2 \rangle_{229} - \langle r^2 \rangle_{232} = -0.300$ fm^2 corresponds to a 33.9(80) GHz ^{229}Th^{3+} -^{232}Th^{3+} isotope shift for the $6D_{3/2} \rightarrow 7S_{1/2}$ transition, which is likely to change the name from "717 nm" ^{232}Th^{3+} to the "718 nm" transition for ^{229}Th^{3+} . The hyperfine splitting of the ^{229}Th^{3+} $7S_{1/2}$ is predicted to be 18(1) GHz.
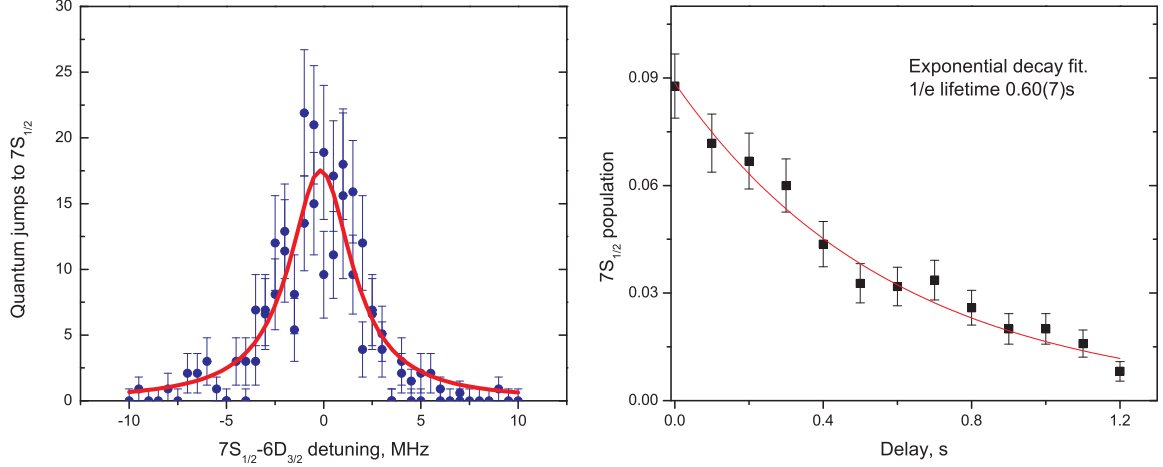
Figure 53: Observation of electronic electric quadrupole transition at 717 nm in ^{232}Th^{3+} . Lifetime of the $7S_{1/2}$ level, measured by counting dark ions. The number transitions to the dark state is recorded and the population is calculated. A dark spot corresponds to the excitation of the ^{232}Th^{3+} ion to the metastable $7S_{1/2}$ level, rather than a pollutant ion, because the constant chain structure and expected sensitivity to the 717 nm frequency. An ion was lost between 16 s and 17 s frames, as seen by the corresponding shifts of the ions.

Finally, this system is used for measuring the lifetime of the $7S_{1/2}$ level. The protocol starts with a 50 ms excitation, followed by a variable delay and a 100 ms long fluoresecence state detection. The period of the sequence is set to 1 s to make sure the ions return to the ground state. The population of the $7S_{1/2}$ level at various delays is shown in Fig. 53b. The exponential fit gives a lifetime of 0.60(7) s, in good agreement with the theoretical value of 0.590 s Ref. [83]. The major systematic error can arise due to the residual $6D_{3/2} \leftrightarrow 7S_{1/2}$ coupling caused by the imperfect attenuation of the 717 nm field after excitation. The magnitude of this error is estimated to be much smaller than the statistical error of 0.07 s.

The successful excitation of the 717 nm transition, whose transition frequency was previously unknown, proved that the developed state detection system is suitable for searching for forbidden transitions in Th^{3+} , particularly the nuclear isomer transition in ^{229}Th^{3+} . In the next section, the 717 nm excitation and the same state detection method is utilized to observe the 269 nm line, the final step to the electron-bridge.

104

6.7   Excitation to the electron bridge with the 269 nm line

The $|7P_{1/2}, g\rangle$ level is the initial state of the strongest electron-bridge transition $|7P_{1/2}, g\rangle \leftrightarrow |7S_{1/2}, m\rangle$. Since the $7S_{1/2}$ level can be populated with the electric quadrupole transition at 717 nm, the 269 nm the $7S_{1/2} \to 7P_{1/2}$ D_1 transition is a natural way to reach the $7P_{1/2}$ level.

The laser light for excitation of this transition was obtained by a single pass doubling of the 539 nm light, generated by an optical parametric oscillator (OPO). The OPO is based on a BBO crystal, pumped with the 10 ns, 10 Hz, 355 nm 3d harmonic of a flash lamp YAG laser. The Littman configuration of the laser cavity allows for frequency tuning with the grating.

The protocol for the 269 nm line spectroscopy is based on the sequence described in the previous section, with the addition of the 269 nm light as shown in Fig. 54. The 717 nm laser excites atoms to the metastable $7S_{1/2}$ state, which is detected by the dark spots in the chain of cold ions as shown in Fig. 52. When the 269 nm field is resonant with the $7S_{1/2} \to 7P_{1/2}$ transition, the atoms are quickly repumped from the $7S_{1/2}$ metastable state due to the short ($\sim$1 ns) lifetime of the $7P_{1/2}$ level and sufficiently strong 269 nm laser field. The scan of the 269 nm frequency and measured population of the metastable state is presented in Fig. 54. The $\approx 100\%$ contrast dip suggests complete depopulation of the $7S_{1/2}$ metastable state, corresponding to the full transfer of the $7S_{1/2}$ population to the $7P_{1/2}$. The intensity of the 269 nm laser was reduced to minimize the linewidth of the dip. Assuming that during the frequency doubling process the light linewidth quadrupled, the OPO linewidth is 40(4) GHz. Interestingly, the wavemeter based on the Fizeau interferometers suggests a 1 THz linewidth, as the interference pattern in the 75 GHz and 3.75 GHz FSR interferometers is not observed. This is attributed to CCD saturation due to the high peak intensity of the pulses.
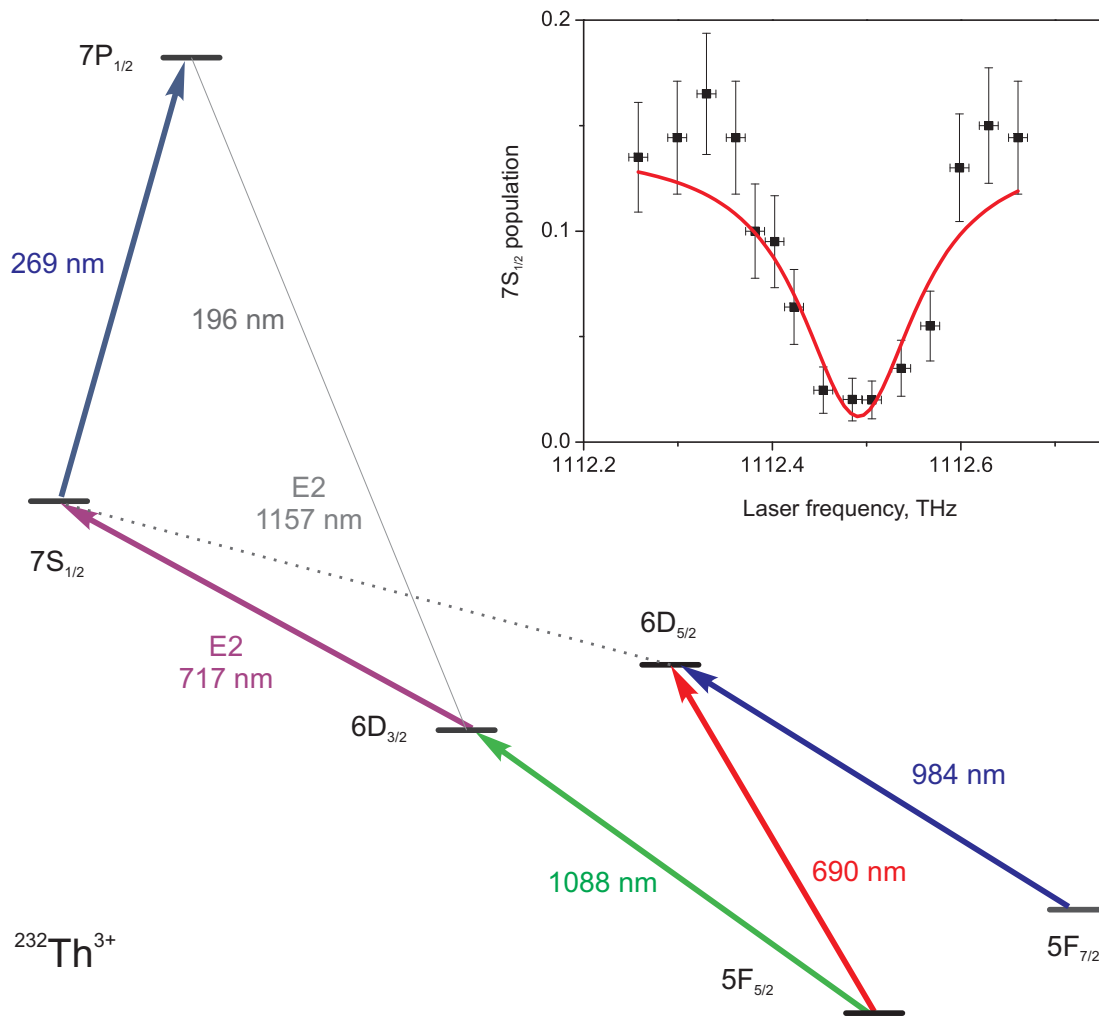
Figure 54: Excitation to the $7P_{1/2}$ level with 269 nm line. The inset shows depopulation of the $7S_{1/2}$ level, when the 269 nm laser light is resonant with the $7P_{1/2} \leftrightarrow 7P_{1/2}$ transition.

6.8   High-power, widely-tunable laser systems

In order to scan the $\sim 10^{15}$ Hz frequency range of the nuclear transition of $\sim$ $100\,\mu$Hz linewidth, the laser system has to provide a sufficient amount of optical power to broaden the transition and reduce the search time to a realistic value. The frequency range of the electron-bridge transition covers parts of UV and the entire visible spectra. There are three types of laser systems that are able to simultaneously provide both tunability and a sufficient amount of power: Ti:sapphire laser with

harmonics generation, dye lasers, and optical parametric oscillators. These laser systems and their pumps are overviewed in this section.

6.8.1 Ti:sapphire laser system

A Ti:sapphire crystal pumped with a 532 nm light provides a broadband gain in red and near infrared ranges. The commercial 80 MHz 2 ps Ti:sapphire laser can be tuned from 690 nm to 1000 nm and generate >500 mW of light. The 250 nm - 690 nm range can be accessed by harmonics generation. Fig. 55 shows a doubler and tripler of picosecond pulses generated by a Ti:sapphire laser. At the 8.6 W cw 532 nm pump power, the Ti:sapph generates 1.05 W at 939 nm. A single pass in the KDP crystal generates 40 mW at 470 nm. This second harmonic is separated from the fundamental field and then recombined. In this way a variable delay of the 939 nm light can be used to compensate for the temporal walk-off. Finally, the sum frequency generation occurs at the second KDP crystal, which produces 0.35 mW at 313 nm. The efficiencies of the second and third harmonic generation can be further optimized with the Boyd-Kleinman analysis [92], generalized to elliptical beams [93].
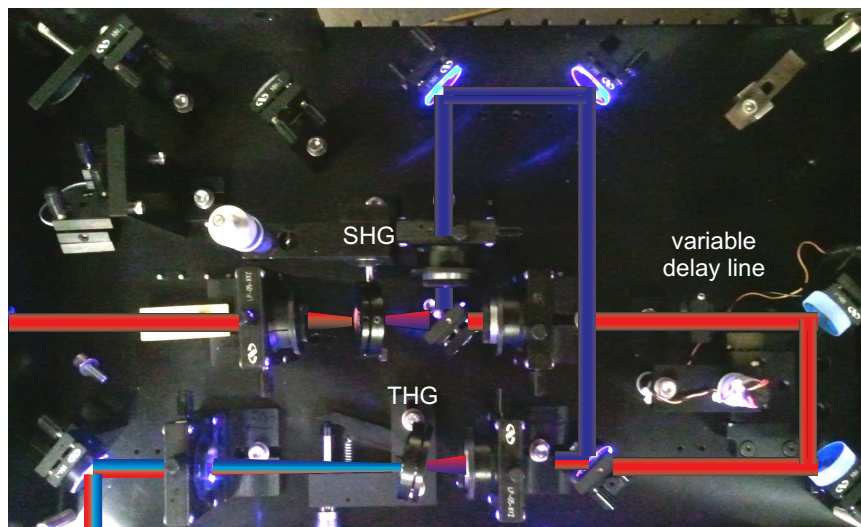
Figure 55: A system for generating second and third harmonics of picosecond pulses, generated by a Ti:sapphire laser.

While the system is able to cover most of the 250 nm - 800 nm range, there is
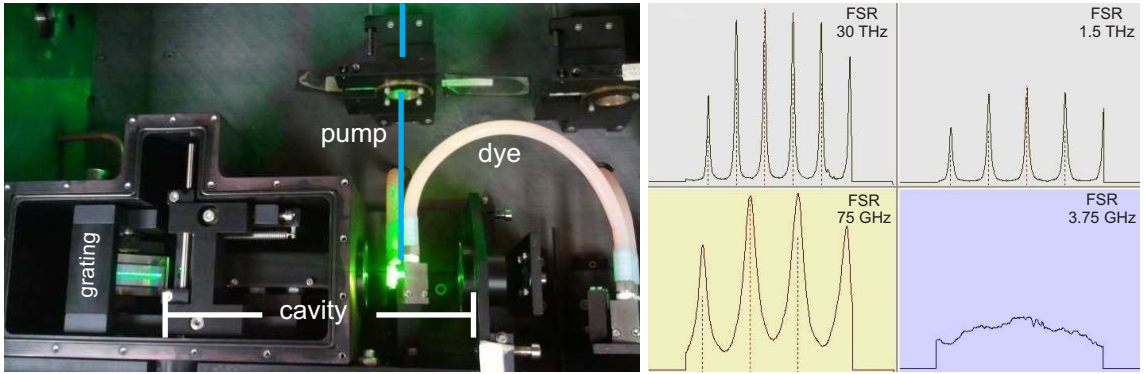
Figure 56: Dye laser pumped with a 355 nm 10 Hz 10 ns YAG laser generates 539 nm light for excitation of the 269 nm Th^{3+} line. The frequency is measured with a wavemeter, which suggests a 25 GHz linewidth; however, the actual linewidth is likely to be ~ 3 GHz. This discrepancy is associated with the saturation of the wavemeter CCD camera with the high peak intensity of the laser pulses.

a 500 nm - 690 nm gap, and the power is significantly reduced due to losses in the harmonic generation processes. Additionally, in order to maintain large population in the $7P_{1/2}$ state with the lifetime of 1 ns, both 269 nm and 196 nm transitions have to be excited and synchronized with the search field on a sub-nanosecond level. This complexity significantly impedes the search of the nuclear transition frequency. Better alternatives are dye lasers and optical parametric oscillators that cover most of the 250 nm - 800 nm range without harmonic generation.

6.8.2 Dye laser

Organic compounds pumped with UV light provide an optical gain in the 311 nm - 1530 nm wavelength range; thus a dye laser with an appropriate pump laser and a corresponding set of dyes can cover most of the frequency uncertainty region for the nuclear transition. A typical dye laser is shown in Fig. 56.

The laser efficiency varies between 5%-20%, such that optical powers of >50 mW can be obtained with >1 W 266 nm, 355 nm YAG pump lasers. A disadvantage associated with the use of a dye laser, however, is the time overhead as a result of changing the dyes, since the typical wavelength tunability range of a dye is $\sim$40 nm.

6.8.3 Optical Parametric Oscillator

An optical parametric oscillator utilizes frequency difference generation in a non-linear crystal. A pump photon spontaneously breaks down into signal and idler photons during the parametric down-conversion process. Finally, an optical cavity for signal and/or idler fields creates optical feedback, which results in lasing. An OPO based on a BBO Type I crystal, pumped with 266 nm 4th harmonic of YAG laser, can lase in the 300 nm - 2340 nm wavelength range [94]. Without narrowing elements, the typical linewidth of an OPO is ~ 1 THz. Wavelength tuning can be accomplished by changing the phase-matching condition with the crystal orientation.

A design of an OPO depends on its pump intensity. In order to make a laser, the round-trip transmission in the optical cavity should be higher than the inverse of the optical gain. With a 10 ns, 10 Hz, 100 mW$_{cw}$, 266 nm pump, a gain of 6 was observed for 795 nm light. With such a high gain, it is relatively easy to construct an OPO with a low finesse cavity. A Littman or Littrow configuration can be used for linewidth narrowing and tuning by using a diffraction grating as a resonator mirror. The 266 nm pump light is obtained by two stages of doubling Nd:YAG laser. The maximum power of 0.5 W$_{cw}$ is observed at 1.5 W$_{cw}$ of 532 nm light. With the typical 10-15% efficiency of an OPO, a >50 mW$_{cw}$ output can be obtained in the 300 nm - 2340 nm range. The uncovered 250 nm - 300 nm range can be reached with a single-pass second harmonic generation, a high-efficiency process with such pulse duty cycle.

At a higher repetition rate of 4 kHz and 80 ns pulses, a 4 W$_{cw}$ 266 nm pump provided a gain of 1.005 for 795 nm light. To satisfy the lasing threshold of the laser, the round trip transmission should be more than 1/1.005=99.5%. For this purpose, the crystal has to be Brewster cut for the resonant field (anti-reflection coatings degrade due to the short wavelength 266 nm pump). The 266 nm pump light is obtained by doubling of 532 nm light, which is generated by intracavity frequency doubling of Nd:YAG laser light. The maximum 266 nm power of 8 W$_{cw}$ is observed

at 80 W_{cw} of 532 nm light by focusing the 532 nm beam with a 10 cm cylindrical lens into a 250 μm diameter beam inside a BBO crystal of 5 mm length. The second harmonic generation efficiency is likely to be limited by the multimodeness of the 532 nm field (M^2=13). At such high power, thermal lensing should be minimized by using optical materials with lower absorption properties. For this reason, all BK7 lenses were replaced with fused silica lenses, resulting in significantly higher 266 nm light generation. With a typical 10-15% efficiency of an OPO, a >0.8 W_{cw} mW_{cw} output can be attained in the 300 nm - 2340 nm range [94].

The most time-efficient alignment of an OPO is done with a tracing light. First, the pump light is aligned with a crystal until parametric down-conversion is observed. Then a tracer light is aligned with the pump by maximizing the amplification of the tracer light intensity. Afterwards, the tracer is retroreflected with the first resonator mirror with the aid of an iris. Finally, the second mirror is positioned, forming an optical cavity to trigger lasing. The alignment of the second mirror can be first accomplished by a retroreflection with an iris or by maximizing the OPO output power.

In conclusion, the described laser systems are sufficiently powerful and tunable for the location and excitation of the nuclear isomer transition. With the given powers, the search time is dominated by the duty cycle of the experiment rather than the available laser power.

CHAPTER VII

CONCLUSION AND OUTLOOK

Several important developments towards quantum telecommunication and a thorium optical nuclear clock are presented in this work. One of them is the first demonstration of long-lived quantum memory compatible with existing optical fiber networks. The near-infrared 795 nm wavelength quantum memory signal is converted to a telecom 1367 nm wavelength with an efficiency of up to 65% while maintaining quantum entanglement with a remotely stored matter excitation. The wavelength conversion is realized with a four-wave mixing process in an optically thick sample of cold rubidium gas. The high optical thickness of more than 150, corresponding to 1.2×10^{11} atoms/cm^2, is captured in a novel Extended Dark Magneto-Optical Trap. The trap in particular can be utilized for future quantum optics experiments where strong interaction is required.

Another key development is the first realization of a multiplexed quantum memory. This quantum memory array is shown to be applicable for the multiplexing quantum telecommunication protocols through the observation of the entanglement between the memory elements. Combined with a long-lived memory compatible with telecom fibers, the quantum memory array forms a basic building block of a quantum repeater. This technology leads us closer to distributing the entanglement on a continental scale with the potential to revolutionize computation and secure communication. Furthermore, these advancements are a step towards deeper understanding of the Einstein-Podolsky-Rosen paradox and fundamental tests of quantum physics.

The first-time laser cooling of triply charged Thorium-229 is presented in this work. The laser-cooled ^{229}Th^{3+} is a system teeming with prospects. Most importantly, this

system opens the path towards the laser excitation of the nuclear isomer transition with an electron-bridge. To that endeavor, the electric quadrupole transition at 717 nm and electric dipole transition at 269 nm are excited for the first time. With available laser systems, the search for the isomer transition with laser beams highly focused on the chain of laser-cooled ^{229}Th^{3+} is expected to take less than a day of the ions' illumination.

Once the isomer state is populated, the methods demonstrated with the hyperfine spectroscopy of the ^{229}Th^{3+} electronic transitions can be used to measure the isomer shifts and the hyperfine structure of the isomer manifold electronic states. The value of the Thorium-229 nuclear ground electric quadrupole moment presented in this work contributes the determination of the sensitivity of the nuclear transition to the variation of fundamental constants. This sensitivity is likely to be a few orders of magnitude higher than most current sensitive measurements of Hg$^+$ and Al$^+$ clocks [3].

Lastly, the laser-cooled triply charged Thorium-229 crystals produced in this work are an ideal system for utilizing the nuclear transition as a primary frequency reference, with potential inaccuracy approaching 1×10^{-19} [7]. The laser excitation of this nuclear transition holds the promise for an exciting era with new levels of precision in time-keeping and in searches for the temporal variation of fundamental constants.

APPENDIX A

MASTER OSCILLATOR POWER AMPLIFIER

External Cavity Diode Lasers are the most common variety of lasers in AMO labs. However, their optical power is typically limited to <200 mW. For high-power applications like laser cooling, fast manipulation semiconductor tapered amplifiers (TA), also known as master oscillator power amplifiers (MOPA), are used. Typically, these chips can produce 1-2 W of optical power with about 10-20 mW of seed laser power. While turnkey MOPA systems are available commercially, a home-built system can reduce costs by a factor of 2 to 4. In this section, a reliable design (Fig.58) is presented, which is proven to operate at the level of commercial systems. An example of the importance of thermal effects at high powers is shown.

A.1 A robust opto-mechanical design for MOPA

A simple design is shown in Fig. 57. A MOPA chip is mounted in a copper mount on top of a thermoelectric cooler (TEC), which is situated on a metal block attached to an optical table. Two aspheric lenses on XYZ translation stages are mounted to the optical table to allow for the seed laser to be injected into the MOPA and for the output beam to be collimated. Operating several such configurations over a few years required a couple of hours of warming up and/or realignment each day when the MOPA was turned back on. The root of such alignment drift is the thermal expansion of the metal block that also serves as a heat sink. Given a typical metal thermal expansion coefficient of $2 \cdot 10^{-5}$ K^{-1}, a metal block height of 0.1 m, and a change in temperature of 5 K would produce a 10 μm shift, comparable with the gain chip dimension. Thus, once the MOPA is turned on and the heat is dissipated in the
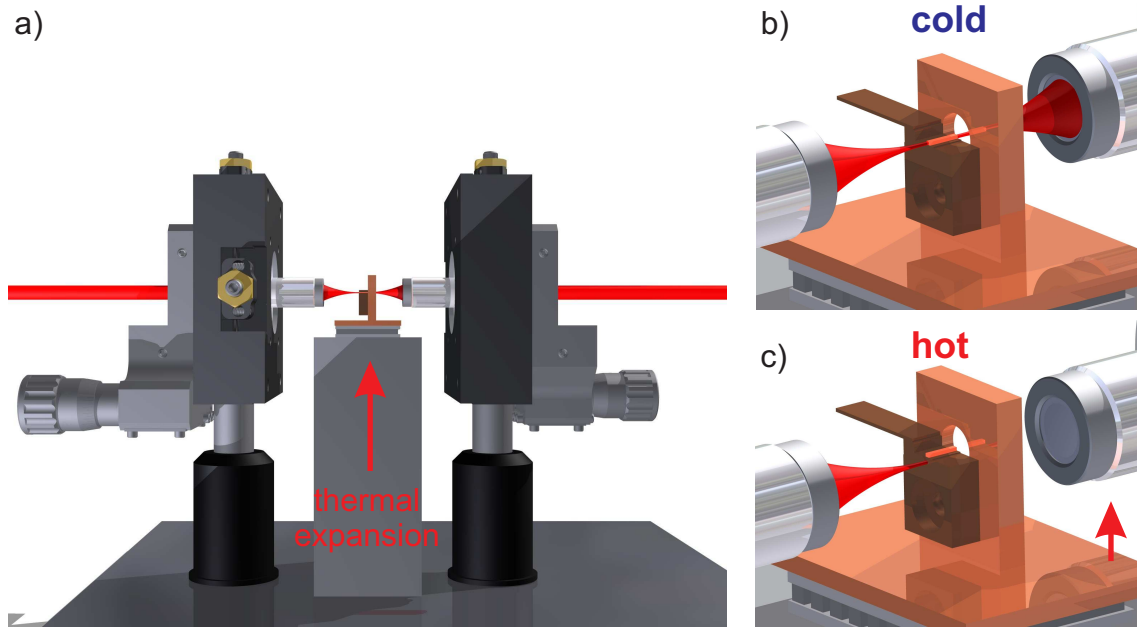
Figure 57: An opto-mechanical design for a Tapered Amplifier affected by thermal effects.

heat sink, injection to the MOPA is misaligned, as is the output mode.

The solution is obvious when the problem is identified: decouple the heat sink from the optical mount and mount the lenses as close to the MOPA reference as possible. These two modifications (Fig. 58) significantly improve the stability and robustness of the alignment. When the MOPA is turned on, the output mode is coupled to a single mode fiber instantaneously and does not drift with time. This design modification saved approximately a thousand man-hours, and made it possible to run complex experiments for several weeks of data acquisition.

A.2   Mode matching of Gaussian beams

Mode matching of Gaussian beams is routine work in an AMO lab, because the eigen modes of lasers, fibers, and optical cavities are typically Gaussian beams. In this section, useful formulas, algorithms, and tricks for mode matching are summarized.

A Gaussian beam of light with wavelength λ is described solely by three parameters: waist size, ω_0, its coordinate(s) z_0, and its wave vector. Mode matching of two
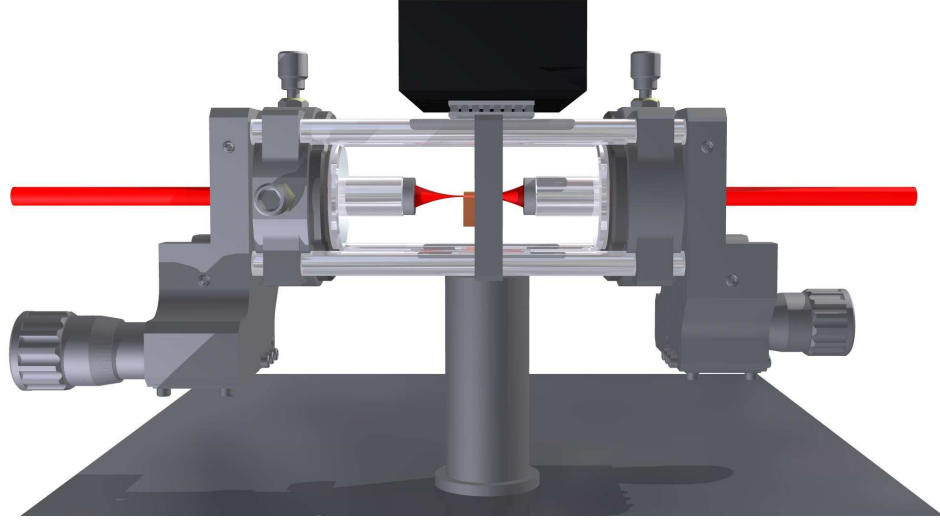
Figure 58: An opto-mechanical design for a Tapered Amplifier unaffected by thermal effects.

Gaussian beams is done by matching these parameters. It is useful to keep in mind a formula for mode matching efficiency, η, in the limit of similar Gaussian beams:

$$
\begin{aligned}
\eta &= \frac{|\int E_1^* E_2|dA}{\sqrt{\int |E_1|^2 dA \int |E_2|^2 dA}} = [(\frac{\omega_1^2(z) + \omega_2^2}{2\omega_1(z)\omega_2})^2 + (\frac{\pi\omega_1(z)\omega_2}{\lambda R_1(z)})^2]^{-1} \approx \\
&\approx 1 - (\frac{\Delta\omega}{\omega_0})^2 - (\frac{\Delta z_0}{z_R})^2,
\end{aligned}
$$

where $E_{1,2}$ are the electric fields of the Gaussian modes, dA is an area element, $\omega_1(z)$, $R_1(z)$ are the spot size and the radius of curvature of the mode E_1 at the waist of the mode E_2, $\Delta\omega$ - difference in waists, ω_0 - average waist, Δz_0 - difference in waists' positions, z_R - average Raleigh range. With accounting Fresnel losses, this formula describes coupling efficiency into a single mode fiber. This formula states that with knowledge of the Gaussian beam parameters and proper mode matching optics, it is possible to achieve unity mode matching efficiency. This makes beam profiling a powerful tool in mode matching, especially with weak and unknown light produced by atoms, e. g. with four-wave mixing, whether it is a frequency conversion or a quantum memory. 80% coupling efficiency to a single mode fiber, or 86% mode matching

efficiency has been demonstrated for a telecom light produced with four-wave mixing. With well-defined modes produced by single mode fibers it is straightforward to couple light from a fiber to a fiber without antireflection coatings with 90% efficiency, which corresponds to $90/92 = 98$ % mode matching.

Typically a laser beam is aligned to a fiber coupler with two mirrors in adjustable mirror mounts. However in many cases it is better to use only one mirror and mount the fiber coupler on a mirror mount. It gives three advantages: savings on one mirror, less space taken on the optical table, and a much faster convergence of the fiber coupling alignment procedure. The latter one is due to the fact that when aspheric lens of the fiber coupler is moved for mode matching, it changes not position the beam, but its direction, which is easily picked up with the mirror mount angular degrees of freedom. Therefore, an angular basis provided by the mount can realign the beam faster.

APPENDIX B

FPGA DRIVER FOR MULTIPLEXED QUANTUM MEMORY

The FPGA board generates the time sequence for for the write AOM, read AOM, and clean field switching, as well as the gating for the signal and idler fields. The FPGA is also used to configure bits for the digital to analog converters (DAC). The DAC is a homemade circuit involving a fast setting time 8-bit DAC chip (DAC0808) combined with a high speed operational amplifier (LM7372). The DAC generates different voltage levels to drive the voltage controlled oscillator (VCO). The VCO is a commercially customized device featuring a high 3 dB bandwidth.

The program (Fig.59) utilizes 4,536 / 4,608 (98 %) of logic elements, 1,828 / 4,608 (40 %) of dedicated logic registers, 77 / 89 (87 %) of pins, 1 / 2 (50 %) PLLs of the field-programmable gate array (FPGA) Cyclone II EP2C5T144C8, realizing several delay generators, pulse generators, time analyzers, USB interface, and control logic, operating with 5 ns precision. At this level of complexity, internal delays inside the chip become important. The program must work not just on a mathematical level of algorithms, but also at a physical level of electrical signals inside the chip.

Altera USB Blaster device uses a FT232 chip, which is a common USB-serial converter, used in the FPGA board for the USB interface. This degeneracy results in a driver conflict. A solution is to rename the driver files, such that the operating system treats the chips separately.

Since it is a generally useful to update FPGA experimental parameters with a computer, I present the core of the source code for a communication protocol through a USB based serial port.
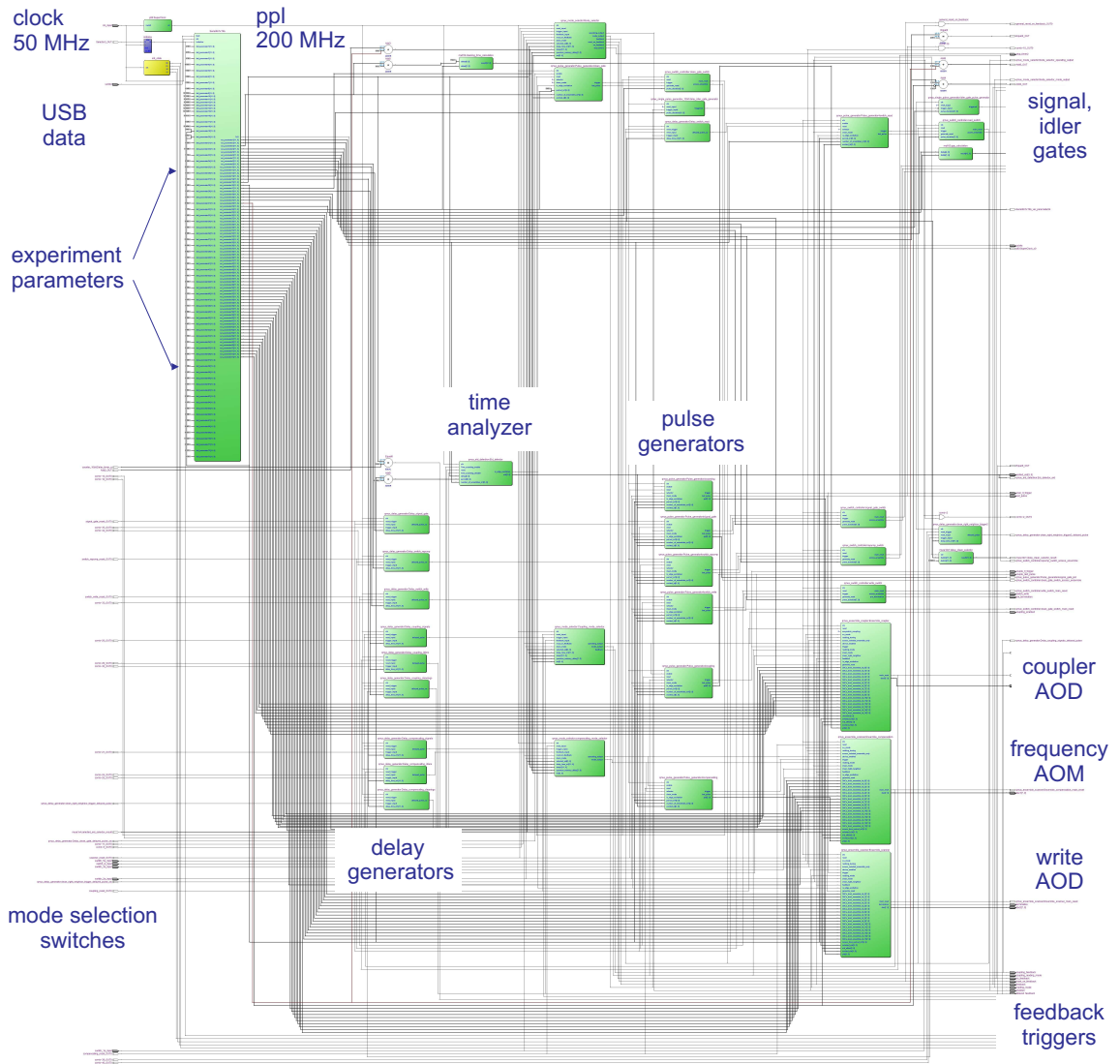
Figure 59: The block diagram of the FPGA program used to control and scan the quantum memory array with the write laser, detect the excited element, and read out the excitation after a variable delay.
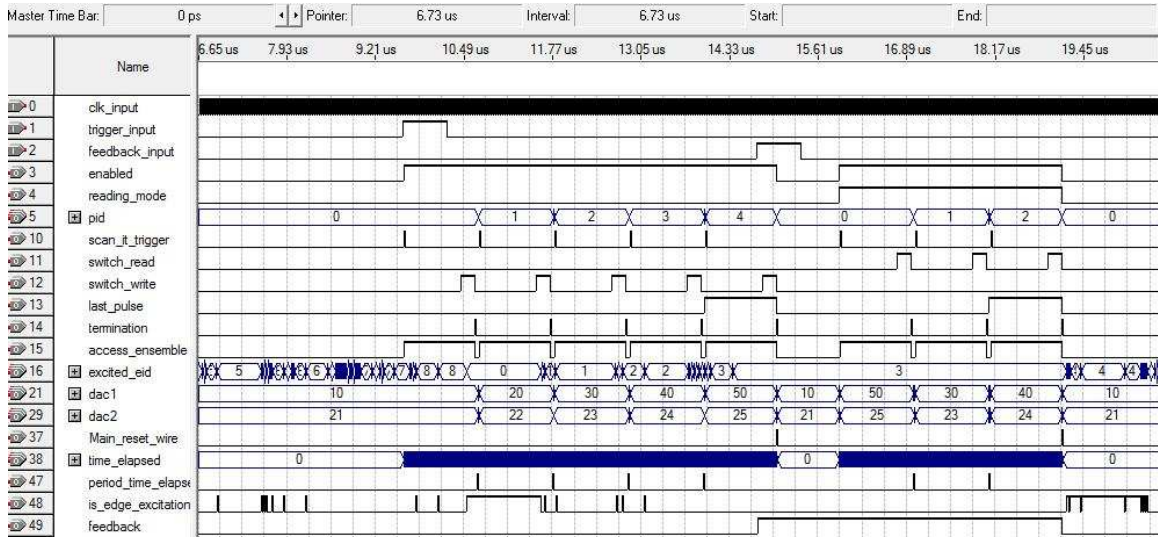
Figure 60: Simulation of the FPGA program used to control the multiplexed quantum memory.

```
1   Commands (sent to Serial COMx port):
    set value:        s[parameter#][space][value]enter
3   set default value:  s[parameter#][space]d
    get value:        g[parameter#]enter
5   load all defaults       !

7   always @(posedge clk)
    case (interface_state)
9       default: interface_state <= 4'd0;
        4'd0: begin //waiting for command key pressed
11              if (RxD_data_ready)
                    case (RxD_data)
13                      8'd115: begin mode <= 1'b0; interface_state <= 4'd1; end //set
                        8'd103: begin mode <= 1'b1; interface_state <= 4'd1; end //get
15                      8'd33: begin mode <= 1'b0; interface_state <= 4'd12; end //set defaults
                endcase
17          if (initialize) begin mode <= 1'b0; interface_state <= 4'd12; end //set defaults
            end
19      4'd1: begin    //initialize
                number_length <= 3'd0; parameter_id <=8'd0;
21              address_or_value <= 1'b0;  interface_state <= 4'd2;
                end
23      4'd2: begin //waiting for digit key pressed
                if (RxD_data_ready)
25                  case (RxD_data)
                    8'd32:  if (mode == 1'b0) interface_state <= 4'd3;
27                  8'd13:  interface_state <= 4'd3;
                    8'd48: begin digit[number_length] <= 4'd0; number_length <= number_length + 3'd1; end
29                  ..
                    8'd57: begin digit[number_length] <= 4'd9; number_length <= number_length + 3'd1; end
31                  8'd100: begin if (address_or_value) interface_state <= 4'd11;   end
                endcase
33          end
        4'd3:  begin
35              case (number_length)
                    3'd1: entered_number <= digit[0];
37                  3'd2: entered_number <= digit[1]+ digit[0]*(4'd10);
                    3'd3: entered_number <= digit[2]+ digit[1]*(4'd10) + digit[0]*(7'd100);
39                  ..
                endcase
41              interface_state <= 4'd4;
            end
43      4'd4: begin
                case (address_or_value)
45                  1'b0:   parameter_id <= entered_number;
                    1'b1:   value <= entered_number;
47                  endcase
            number_length <= 3'd0;        interface_state <= 4'd5;
49          end
        4'd5: begin   // what to do after getting some number
51              case (mode)
                1'b0: begin //prepare to get value
53                      if (~address_or_value)
                            begin address_or_value <= 1'b1;   interface_state <= 4'd2; end
55                          else interface_state <= 4'd6;
                    end
57              1'b1: begin //show value and terminate
                    telecom_data <=  var_parameter[parameter_id];
59              interface_state <= 4'd7;
                    end
```

119

```verilog
                      endcase
                  end
      4'd6: begin  //update parameter
                  var_parameter[parameter_id] <= value;
               telecom_data <= value;
                  interface_state <= 4'd7;

          end
      4'd7: begin  //show result
              decode2decimal <= 1'b1;            interface_state <= 4'd8;     end
      4'd8: interface_state <= 4'd9;
      4'd9: begin  //wait until transmit is done and finalize
              decode2decimal <= 1'b0;           if(done) interface_state <= 4'd0; end
      4'd11: begin  //load default
              entered_number <= var_parameter_default[parameter_id];   interface_state <= 4'd4; end
      4'd12: begin  //load defaults
              parameter_inc <= 8'd0;   interface_state <= 4'd13;     end
      4'd13: begin      var_parameter[parameter_inc] <= var_parameter_default[parameter_inc];
                        interface_state <= 4'd14; end
      4'd14: begin      parameter_inc <= parameter_inc + 8'd1;     interface_state <= 4'd15; end
      4'd15: begin
                   if(parameter_inc == number_of_parameters)
                       begin
                  telecom_data <= parameter_inc;
                  interface_state <= 4'd7;
                end
          else interface_state <= 4'd13;
                  end
endcase

///// STRING SENDER STATE MACHINE ////////////////////////////////////////
reg send_char;
reg [7:0] char_out;
reg [3:0] i_counter;
reg done;
reg [2:0] state_string_sender;
wire [3:0] stringLength = 4'd6;

always @(posedge clk)
    begin
       case(state_string_sender)
       3'd0: if (send_string_trigger) state_string_sender <= 3'd1;
       3'd1: state_string_sender <= 3'd2;
     3'd2: state_string_sender <= 3'd3;
     3'd3: state_string_sender <= 3'd4;
       3'd4: state_string_sender <= 3'd5;
       3'd5: state_string_sender <= 3'd6;
       3'd6: begin
                   if( done == 1'b0) state_string_sender <= 3'd2;
                   if (done & ~send_string_trigger) state_string_sender <= 3'd0;
               end
       endcase
    end

always @(posedge clk)
    case(state_string_sender)
       3'd1: begin i_counter <= 4'd0; done <= 1'b0; end
       3'd2:
               begin
                   if(~transmitter_busy)
                       begin
                  char_out = decimal_string[i_counter];
                       send_char = 1'b1;
                       end
               end
       3'd5: begin
                   if(send_char == 1'b1)
                       begin   i_counter <= i_counter+4'd1; send_char <= 1'b0;   end
                   if(i_counter == stringLength) done = 1'b1;
               end
    endcase
```

120

REFERENCES

[1] L.-M. Duan, M. D. Lukin, J. I. Cirac, and P. Zoller, "Long-Distance Quantum Communication with Atomic Ensembles and Linear Optics," *Nature* **414**, 413 (2001).

[2] D. N. Matsukevich, T. Chanelière, S. D. Jenkins, S.-Y. Lan, T. A. B. Kennedy, and A. Kuzmich, "Entanglement of Remote Atomic Qubits," *Phys. Rev. Lett.* **96**, 030405 (2006).

[3] T. Rosenband, D. B. Hume, P. O. Schmidt, C. W. Chou, A. Brusch, L. Lorini, W. H. Oskay, R. E. Drullinger, T. M. Fortier, J. E. Stalnaker, S. A. Diddams, W. C. Swann, N. R. Newbury, W. M. Itano, D. J. Wineland, and J. C. Bergquist, "Frequency Ratio of Al$^+$ and Hg$^+$ Single-Ion Optical Clocks; Metrology at the 17th Decimal Place," *Science* **319**, 1808 (2008).

[4] H.-J. Briegel, W. Dür, J. I. Cirac, and P. Zoller, "Quantum Repeaters: The Role of Imperfect Local Operations in Quantum Communication," *Phys. Rev. Lett.* **81**, 5932 (1998).

[5] C. H. Bennett and G. Brassard, in *Proceedings of the International Conference on Computers, Systems and Signal Processing* (Indian Institute of Science, Bangalore, India, 1984).

[6] P. W. Shor, "Polynomial-Time Algorithms for Prime Factorization and Discrete Logarithms on a Quantum Computer," *SIAM J. Comput.* **26**, 1484 (1997).

[7] C. J. Campbell, A. G. Radnaev, A. Kuzmich, V. A. Dzuba, V. V. Flambaum, and A. Derevianko, "Single-Ion Nuclear Clock for Metrology at the 19th Decimal Place," *Phys. Rev. Lett.* **108**, 120802 (2012).

[8] V. V. Flambaum, "Enhanced Effect of Temporal Variation of the Fine Structure Constant and the Strong Interaction in ^{229}Th," *Phys. Rev. Lett.* **97**, 092502 (2006).

[9] W. K. Wootters and W. H. Zurek, "A single quantum cannot be cloned," *Nature* **299**, 802 (1982).

[10] C. Bonato, A. Tomaello, V. D. Deppo, G. Naletto, and P. Villoresi, "Feasibility of satellite quantum key distribution," *New Journal of Physics* **11**, 045017 (2009).

[11] T. Chanelière, D. N. Matsukevich, S. D. Jenkins, S.-Y. Lan, T. A. B. Kennedy, and A. Kuzmich, "Storage and Retrieval of Single Photons Transmitted Between Remote Quantum Memories," *Nature* **438**, 833 (2005).

[12] S.-Y. Lan, S. D. Jenkins, T. Chanelière, D. N. Matsukevich, C. J. Campbell, R. Zhao, T. A. B. Kennedy, and A. Kuzmich, "Dual-Species Matter Qubit Entangled with Light," *Phys. Rev. Lett.* **98**, 123602 (2007).

[13] T. Chanelière, D. N. Matsukevich, S. D. Jenkins, T. A. B. Kennedy, M. S. Chapman, and A. Kuzmich, "Quantum Telecommunication Based on Atomic Cascade Transitions," *Phys. Rev. Lett.* **96**, 093604 (2006).

[14] R. Zhao, Y. O. Dudin, S. D. Jenkins, C. J. Campbell, D. N. Matsukevich, T. A. B. Kennedy, and A. Kuzmich, "Long-Lived Quantum Memory," *Nature Physics* **5**, 100 (2009).

[15] D. N. Matsukevich, T. Chanelière, S. D. Jenkins, S.-Y. Lan, T. A. B. Kennedy, and A. Kuzmich, "Deterministic Single Photons via Conditional Quantum Evolution," *Phys. Rev. Lett.* **97**, 013601 (2006).

[16] D. N. Matsukevich and A. Kuzmich, "Quantum State Transfer Between Matter and Light," *Science* **306**, 663 (2004).

[17] D. N. Matsukevich, T. Chanelière, S. D. Jenkins, S.-Y. Lan, T. A. B. Kennedy, and A. Kuzmich, "Observation of Dark State Polariton Collapses and Revivals," *Phys. Rev. Lett.* **96**, 033601 (2006).

[18] J. Simon, H. Tanji, S. Ghosh, and V. Vuletić, "Single-Photon Bus Connecting Spin-Wave Quantum Memories," *Nature Physics* **3**, 765 (2007).

[19] Y.-A. Chen *et al.*, "Memory-Built-In Quantum Teleportation with Photonic and Atomic Qubits," *Nature Physics* **4**, 103 (2008).

[20] A. Einstein, B. Podolsky, and N. Rosen, "Can Quantum-Mechanical Description of Physical Reality Be Considered Complete?," *Phys. Rev.* **47**, 777 (1935).

[21] A. Garg and N. D. Mermin, "Detector inefficiencies in the Einstein-Podolsky-Rosen experiment," *Phys. Rev. D* **35**, 3831 (1987).

[22] O. A. Collins, S. D. Jenkins, A. Kuzmich, and T. A. B. Kennedy, "Multiplexed Memory-Insensitive Quantum Repeaters," *Phys. Rev. Lett.* **98**, 060502 (2007).

[23] D. N. Matsukevich, P. Maunz, D. L. Moehring, S. Olmschenk, and C. Monroe, "Bell Inequality Violation with Two Remote Atomic Qubits," *Phys. Rev. Lett.* **100**, 150404 (2008).

[24] C. H. van der Wall, M. D. Eisaman, A. André, R. L. Walsworth, D. F. Phillips, A. S. Zibrov, and M. D. Lukin, "Atomic Memory for Correlated Photon States," *Science* **301**, 196 (2003).

[25] J. Simon, H. Tanji, S. Ghosh, and V. Vuletić, "Single-Photon Bus Connecting Spin-Wave Quantum Memories," *Nature Physics* **3**, 765 (2007).

[26] N. Ashby, T. P. Heavner, S. R. Jefferts, T. E. Parker, A. G. Radnaev, and Y. O. Dudin, "Testing Local Position Invariance with Four Cesium-Fountain Primary Frequency Standards and Four NIST Hydrogen Masers," *Phys. Rev. Lett.* **98**, 070802 (2007).

[27] P. Jessen and I. Deutsch, "Optical Lattices,", volume 37 of *Advances In Atomic, Molecular, and Optical Physics* pp. 95 – 138 Academic Press 1996.

[28] D. D. Yavuz, P. B. Kulatunga, E. Urban, T. A. Johnson, N. Proite, T. Henage, T. G. Walker, and M. Saffman, "Fast Ground State Manipulation of Neutral Atoms in Microscopic Optical Traps," *Phys. Rev. Lett.* **96**, 063001 (2006).

[29] J. Kruse, C. Gierl, M. Schlosser, and G. Birkl, "Reconfigurable site-selective manipulation of atomic quantum systems in two-dimensional arrays of dipole traps," *Phys. Rev. A* **81**, 060308 (2010).

[30] S. Kuhr, W. Alt, D. Schrader, I. Dotsenko, Y. Miroshnychenko, A. Rauschenbeutel, and D. Meschede, "Analysis of dephasing mechanisms in a standing-wave dipole trap," *Phys. Rev. A* **72**, 023406 (2005).

[31] Y. O. Dudin, S. D. Jenkins, R. Zhao, D. N. Matsukevich, A. Kuzmich, and T. A. B. Kennedy, "Entanglement of a Photon and an Optical Lattice Spin Wave," *Phys. Rev. Lett.* **103**, 020505 (2009).

[32] A. G. Radnaev, Y. O. Dudin, R. Zhao, H. H. Jen, S. D. Jenkins, A. Kuzmich, and T. A. B. Kennedy, "A quantum memory with telecom-wavelength conversion," *Nature Physics* **6**, 894 (2010).

[33] Y. O. Dudin, R. Zhao, T. A. B. Kennedy, and A. Kuzmich, "Light storage in a magnetically dressed optical lattice," *Phys. Rev. A* **81**, 041805 (2010).

[34] P. C. Maurer, G. Kucsko, C. Latta, L. Jiang, N. Y. Yao, S. D. Bennett, F. Pastawski, D. Hunger, N. Chisholm, M. Markham, D. J. Twitchen, J. I. Cirac, and M. D. Lukin, "Room-Temperature Quantum Bit Memory Exceeding One Second," *Science* **336**, 1283 (2012).

[35] M. Steger, K. Saeedi, M. L. W. Thewalt, J. J. L. Morton, H. Riemann, N. V. Abrosimov, P. Becker, and H.-J. Pohl, "Quantum Information Storage for over 180 s Using Donor Spins in a ^{28}Si Semiconductor Vacuum," *Science* **336**, 1280 (2012).

[36] L. Kroger and C. Reich, "Features of the low-energy level scheme of ^{229}Th as observed in the α-decay of ^{233}U," *Nuclear Physics A* **259**, 29 (1976).

[37] C. W. Reich and R. G. Helmer, "Energy separation of the doublet of intrinsic states at the ground state of ^{229}Th," *Phys. Rev. Lett.* **64**, 271 (1990).

[38] R. G. Helmer and C. W. Reich, "An excited state of ^{229}Th at 3.5 eV," *Phys. Rev. C* **49**, 1845 (1994).

[39] B. R. Beck, J. A. Becker, P. Beiersdorfer, G. V. Brown, K. J. Moody, J. B. Wilhelmy, F. S. Porter, C. A. Kilbourne, and R. L. Kelley, "Energy Splitting of the Ground-State Doublet in the Nucleus ^{229}Th," *Phys. Rev. Lett.* **98**, 142501 (2007).

[40] E. Peik and C. Tamm, "Nuclear laser spectroscopy of the 3.5 eV transition in Th-229," *EPL (Europhysics Letters)* **61**, 181 (2003).

[41] W. G. Rellergert, D. DeMille, R. R. Greco, M. P. Hehlen, J. R. Torgerson, and E. R. Hudson, "Constraining the Evolution of the Fundamental Constants with a Solid-State Optical Frequency Reference Based on the ^{229}Th Nucleus," *Phys. Rev. Lett.* **104**, 200802 (2010).

[42] E. Peik, K. Zimmermann, M. Okhapkin, and C. Tamm, "Prospects for a Nuclear Optical Frequency Standard Based on THORIUM-229," in *Frequency Standards and Metrology*, edited by L. Maleki pp. 532–538 2009 0812.3548.

[43] G. A. Kazakov, A. N. Litvinov, V. I. Romanenko, L. P. Yatsenko, A. V. Romanenko, M. Schreitl, G. Winkler, and T. Schumm, "Performance of a ^{229}Thorium solid-state nuclear clock," *ArXiv e-prints* (2012) 1204.3268.

[44] A. D. Ludlow, T. Zelevinsky, G. K. Campbell, S. Blatt, M. M. Boyd, M. H. G. de Miranda, M. J. Martin, J. W. Thomsen, S. M. Foreman, J. Ye, T. M. Fortier, J. E. Stalnaker, S. A. Diddams, Y. Le Coq, Z. W. Barber, N. Poli, N. D. Lemke, K. M. Beck, and C. W. Oates, "Sr Lattice Clock at 1×10^{16} Fractional Uncertainty by Remote Optical Evaluation with a Ca Clock," *Science* **319**, 1805 (2008).

[45] X. tao He and Z. zhou Ren, "Temporal variation of the fine structure constant and the strong interaction parameter in the ^{229}Th transition," *Nuclear Physics A* **806**, 117 (2008).

[46] V. V. Flambaum, N. Auerbach, and V. F. Dmitriev, "Coulomb energy contribution to the excitation energy in ^{229}Th and enhanced effect of α variation," *EPL (Europhysics Letters)* **85**, 50005 (2009).

[47] A. C. Hayes, J. L. Friar, and P. Möller, "Splitting sensitivity of the ground and 7.6 eV isomeric states of ^{229}Th," *Phys. Rev. C* **78**, 024311 (2008).

[48] E. Litvinova, H. Feldmeier, J. Dobaczewski, and V. Flambaum, "Nuclear structure of lowest ^{229}Th states and time-dependent fundamental constants," *Phys. Rev. C* **79**, 064303 (2009).

[49] J. C. Berengut, V. A. Dzuba, V. V. Flambaum, and S. G. Porsev, "Proposed Experimental Method to Determine α Sensitivity of Splitting between Ground and 7.6 eV Isomeric States in ^{229}Th," *Phys. Rev. Lett.* **102**, 210801 (2009).

[50] S. G. Porsev, V. V. Flambaum, E. Peik, and C. Tamm, "Excitation of the Isomeric ^{229m}Th Nuclear State via an Electronic Bridge Process in ^{229}Th^{+}," *Phys. Rev. Lett.* **105**, 182501 (2010).

[51] D. J. Wineland, R. E. Drullinger, and F. L. Walls, "Radiation-Pressure Cooling of Bound Resonant Absorbers," *Phys. Rev. Lett.* **40**, 1639 (1978).

[52] C. J. Campbell, A. V. Steele, L. R. Churchill, M. V. DePalatis, D. E. Naylor, D. N. Matsukevich, A. Kuzmich, and M. S. Chapman, "Multiply Charged Thorium Crystals for Nuclear Laser Spectroscopy," *Phys. Rev. Lett.* **102**, 233004 (2009).

[53] S. Y. Lan, A. G. Radnaev, O. A. Collins, D. N. Matsukevich, T. A. B. Kennedy, and A. Kuzmich, "A Multiplexed Quantum Memory," *Opt. Express* **17**, 13639 (2009).

[54] J. S. Bell, "On the Einstein-Podolsky-Rosen paradox," *Physics (Long Island City, N.Y.)* **1**, 195 (1964).

[55] J. S. Bell, "On the Problem of Hidden Variables in Quantum Mechanics," *Rev. Mod. Phys.* **38**, 447 (1966).

[56] J. F. Clauser, M. A. Horne, A. Shimony, and R. A. Holt, "Proposed Experiment to Test Local Hidden-Variable Theories," *Phys. Rev. Lett.* **23**, 880 (1969).

[57] B. Zhao, Z.-B. Chen, Y.-A. Chen, J. Schmiedmayer, and J.-W. Pan, "Robust Creation of Entanglement between Remote Memory Qubits," *Phys. Rev. Lett.* **98**, 240502 (2007).

[58] L. Jiang, J. M. Taylor, and M. D. Lukin, "Fast and robust approach to long-distance quantum communication with atomic ensembles," *Phys. Rev. A* **76**, 012301 (2007).

[59] H. H. Jen and T. A. B. Kennedy, "Efficiency of light-frequency conversion in an atomic ensemble," *Phys. Rev. A* **82**, 023815 (2010).

[60] R. T. Willis, F. E. Becerra, L. A. Orozco, and S. L. Rolston, "Four-wave mixing in the diamond configuration in an atomic vapor," *Phys. Rev. A* **79**, 033814 (2009).

[61] W. Ketterle, K. B. Davis, M. A. Joffe, A. Martin, and D. E. Pritchard, "High densities of cold atoms in a *dark* spontaneous-force optical trap," *Phys. Rev. Lett.* **70**, 2253 (1993).

[62] Y.-W. Lin, H.-C. Chou, P. P. Dwivedi, Y.-C. Chen, and I. A. Yu, "Using a pair of rectangular coils in the MOT for the production of cold atom clouds with large optical density," *Opt. Express* **16**, 3753 (2008).

[63] T. Y. Abi-Salloum, "Electromagnetically induced transparency and Autler-Townes splitting: Two similar but distinct phenomena in two categories of three-level atomic systems," *Phys. Rev. A* **81**, 053836 (2010).

[64] Y. O. Dudin, A. G. Radnaev, R. Zhao, J. Z. Blumoff, T. A. B. Kennedy, and A. Kuzmich, "Entanglement of Light-Shift Compensated Atomic Spin Waves with Telecom Light," *Phys. Rev. Lett.* **105**, 260502 (2010).

[65] S. D. Jenkins, *Theory of Light–Atomic Ensemble Interactions: Entanglement, Storage and Retrieval*, PhD thesis Georgia Institute of Technology 2006.

[66] P. Grangier, G. Roger, and A. Aspect, "Experimental Evidence for a Photon Anticorrelation Effect on a Beam Splitter: A New Light on Single-Photon Interferences," *Europhys. Lett.* **1**, 173 (1986).

[67] D. F. Walls and G. J. Milburn, *Quantum Optics* (Springer-Verlag, Berlin, 1994).

[68] N. Lundblad, M. Schlosser, and J. V. Porto, "Publisher's Note: Experimental observation of magic-wavelength behavior of ^{87}Rb atoms in an optical lattice [Phys. Rev. A 81, 031611 (2010)]," *Phys. Rev. A* **81**, 049904 (2010).

[69] S. Chen, Y.-A. Chen, B. Zhao, Z.-S. Yuan, J. Schmiedmayer, and J.-W. Pan, "Demonstration of a Stable Atom-Photon Entanglement Source for Quantum Repeaters," *Phys. Rev. Lett.* **99**, 180505 (2007).

[70] Y. O. Dudin, L. Li, and A. Kuzmich, "Light storage on the scale of a minute," *submitted* (2012).

[71] C. J. Campbell, A. G. Radnaev, and A. Kuzmich, "Wigner Crystals of ^{229}Th for Optical Excitation of the Nuclear Isomer," *Phys. Rev. Lett.* **106**, 223001 (2011).

[72] I. Angeli, "A consistent set of nuclear rms charge radii: properties of the radius surface R(N,Z)," *Atomic Data and Nuclear Data Tables* **87**, 185 (2004).

[73] C. E. Bemis, F. K. McGowan, J. L. C. F. Jr, W. T. Milner, R. L. Robinson, P. H. Stelson, G. A. Leander, and C. W. Reich, "Coulomb excitation of states in ^{229}Th," *Physica Scripta* **38**, 657 (1988).

[74] Gerstenkorn, S., Luc, P., Verges, J., Englekemeir, D.W., Gindler, J.E., and Tomkins, F.S., "Structures hyperfines du spectre d'étincelle, moment magnétique et quadrupolaire de l'isotope 229 du thorium," *J. Phys. France* **35**, 483 (1974).

[75] B. R. Beck, J. A. Becker, P. Beiersdorfer, G. V. Brown, J. K. Moody, C. Y. Wu, J. B. Wilhelmy, F. S. Porter, C. A. Kilbourne, and R. L. Kelley, "Improved Value for the Energy Splitting of the Ground-State Doublet in the Nucleus ^{229}Th," (2010).

[76] S. Raeder, V. Sonnenschein, T. Gottwald, I. D. Moore, M. Reponen, S. Rothe, N. Trautmann, and K. Wendt, "Resonance ionization spectroscopy of thorium isotopes-towards a laser spectroscopic identification of the low-lying 7.6 eV isomer of ^{229}Th," *Journal of Physics B Atomic Molecular Physics* **44**, 165005 (2011) 1105.4646.

[77] O. A. Herrera-Sancho, M. V. Okhapkin, K. Zimmermann, C. Tamm, E. Peik, A. V. Taichenachev, V. I. Yudin, and P. Głowacki, "Two-photon laser excitation of trapped ^{232}Th$^+$ ions via the 402-nm resonance line," *Phys. Rev. A* **85**, 033402 (2012).

[78] R. J. Lang, "The spectrum of trebly ionized thorium," *Canadian Journal of Research* **14a**, 43 (1936).

[79] P. Klinkenberg and R. Lang, "The spectrum of trebly ionized thorium, Th IV," *Physica* **15**, 774 (1949).

[80] G. Charles, "A compilation of data on some spectra of Thorium," *Oak Ridge National Lab Technical Report* , 161 (1958).

[81] B. A. Palmer and J. R. Engleman, "Atlas of the Thorium Spectrum," *Los Alamos National Lab.* , 333 (1983).

[82] P. Klinkenberg, "Spectral structure of trebly ionized thorium, Th IV," *Physica B+C* **151**, 552 (1988).

[83] U. I. Safronova, W. R. Johnson, and M. S. Safronova, "Excitation energies, polarizabilities, multipole transition rates, and lifetimes in Th IV," *Phys. Rev. A* **74**, 042511 (2006).

[84] J. C. Berengut, V. A. Dzuba, V. V. Flambaum, and A. Ong, "Electron-Hole Transitions in Multiply Charged Ions for Precision Laser Spectroscopy and Searching for Variations in α," *Phys. Rev. Lett.* **106**, 210802 (2011).

[85] G. A. Kazakov, A. N. Litvinov, V. I. Romanenko, L. P. Yatsenko, A. V. Romanenko, M. Schreitl, G. Winkler, and T. Schumm, "Performance of a 229 Thorium solid-state nuclear clock," *ArXiv e-prints* (2012) 1204.3268.

[86] V. V. Flambaum and S. G. Porsev, "Enhanced sensitivity to the fine-structure-constant variation in the Th IV atomic clock transition," *Phys. Rev. A* **80**, 064502 (2009).

[87] K. Zimmermann, M. V. Okhapkin, O. A. Herrera-Sancho, and E. Peik, "Laser ablation loading of a radiofrequency ion trap," *Applied Physics B: Lasers and Optics* **107**, 883 (2012) 1112.1664.

[88] L. R. Churchill, M. V. DePalatis, and M. S. Chapman, "Charge exchange and chemical reactions with trapped Th^{3+}," *Phys. Rev. A* **83**, 012710 (2011).

[89] M. S. Safronova, (private communication).

[90] C. Schwartz, "Theory of Hyperfine Structure," *Phys. Rev.* **97**, 380 (1955).

[91] S. G. Porsev and V. V. Flambaum, "Effect of atomic electrons on the 7.6-eV nuclear transition in $^{229}Th^{3+}$," *Phys. Rev. A* **81**, 032504 (2010).

[92] G. D. Boyd and D. A. Kleinman, "Parametric Interaction of Focused Gaussian Light Beams," *Journal of Applied Physics* **39**, 3597 (1968).

[93] T. Freegarde, J. Coutts, J. Walz, D. Leibfried, and T. W. Hänsch, "General analysis of type I second-harmonic generation with elliptical Gaussian beams," *J. Opt. Soc. Am. B* **14**, 2010 (1997).

[94] N. V. Kondratyuk, A. A. Shagov, K. L. Demidchik, A. M. Yurkin, and A. E. Kokh, "BBO-crystal optical parametric oscillator tunable over the 300 2340 nm range and pumped by the 4th harmonic of a Nd:YAG laser," *Quantum Electronics* **30**, 253 (2000).

LIST OF PUBLICATIONS

1. S.-Y. Lan, A. G. Radnaev, O. A. Collins, D. N. Matsukevich, T. A. B. Kennedy and A. Kuzmich, "A Multiplexed Quantum Memory," *Optics Express* **17**, 13639-13645 (2009)

2. A. G. Radnaev, Y. O. Dudin, R. Zhao, H. H. Jen, S. D. Jenkins, A. Kuzmich and T. A. B. Kennedy, "A Quantum Memory with Telecom-Wavelength Conversion," *Nature Physics* **6**, 894 (2010)

3. Y. O. Dudin, A. G. Radnaev, R. Zhao, J. Z. Blumoff, T. A. B. Kennedy, and A. Kuzmich, "Entanglement of Light-Shift Compensated Atomic Spin Waves with Telecom Light," *Phys. Rev. Lett.* **105**, 260502 (2010).

4. C. J. Campbell, A. G. Radnaev, and A. Kuzmich, "Wigner Crystals of ^{229}Th for Optical Excitation of the Nuclear Isomer," *Phys. Rev. Lett.* **106**, 223001 (2011)

5. C. J. Campbell, A. G. Radnaev, A. Kuzmich, V. A. Dzuba, V. V. Flambaum, and A. Derevianko, "A Single-Ion Nuclear Clock for Metrology at the 19th Decimal Place," *Phys. Rev. Lett.* **108**, 120802 (2012)

VITA

Alexander G. Radnaev was born in Irkutsk, USSR.